Università degli Studi di Udine
PhD programme in
Environmental and Energy Engineering Sciences

PhD programme Chair Prof. Alfredo SOLDATI

Dynamics of passive and active particles at the surface of a stratified/unstratified turbulent open channel flow

Dott. Salvatore Lovecchio

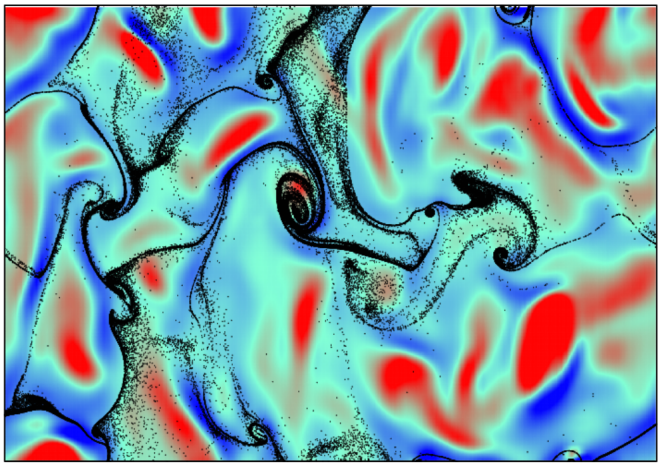

EVALUATION PANEL

Prof. Eric CLIMENT	Reviewer
Prof. Bernhard MEHLIG	Reviewer
Dr. Cristian MARCHIOLI	Committee member
Prof. Luca BRANDT	Committee member
Dr. Francesco PICANO	Committee member
Prof. Alfredo SOLDATI	Supervisor

Author's Web Page: http://158.110.32.35/PEOPLE/Lovecchio.html

Author's e-mail: salvatore.lovecchio@uniud.it - lovecchio.salvo@gmail.com

Author's address:

Dipartimento di Ingegneria Elettrica
Gestionale e Meccanica
Università degli Studi di Udine
Via delle Scienze, 206
33100 Udine – Italia
mobile. +39 347 3021010
web: `http://www.diegm.uniud.it`

Abstract

In this thesis the behaviour of passive and active particles in a turbulent open channel flow has been investigated. The surface of the turbulent open channel has been treated as a flat free-slip surface that bounds a three-dimensional volume in which the flow is turbulent. This configuration mimics the motion of active/passive ocean surfactants (e.g. phytoplankton, floaters or drifters) when surface waves and ripples are absent. The investigation include the study for stable stratified open channel flow.

The nature of the surface turbulence is crucial for the dynamics of particles which float in the upper layers. Surface turbulence has been analysed in terms of energy transfer among the scales and the role of surface compressibility has been included in this analysis. An extensive campaign of Direct Numerical Simulations (DNS) coupled with Lagrangian Particle Tracking (LPT) is used to study these phenomena. The governing equations are solved using a pseudo-spectral method for the specific case of turbulent water flow in a channel.

Results show that free-surface is characterised by an inverse energy cascade which becomes persistent at higher Reynolds number. Surface is forced by means of upwellings which appear as two-dimensional sources for the surface-parallel fluid velocity and alternate to sinks associated with downdrafts of fluid from the surface to the bulk. Consequently, surface compressibility is increased.

Passive buoyant particles reach the surface by means of upwellings and form highly concentrated filaments in downwelling regions. They cluster at large scales and persist for long time. In case of stratification, the surfacing is influenced by the presence of internal gravity waves and the clustering at the surface is destroyed. Finally, the case of self propelled active particles which mimics the behaviour of gyrotactic phytoplankton, has been examined. The main preliminary result is that the presence of stratification is able to make the vertical migration more unstable and to delay the surfacing of the swimming cells.

Contents

List of Figures

1

Introduction

Turbulent fluid flow is a complex, nonlinear multiscale phenomenon which leaves open some of the most fundamental problems in classical physics.
Most of the natural and industrial flows are turbulent and contain dispersed inclusion ("particles"). Understanding the mechanisms of transport and mixing processes is central to the study, for example, of the weather, the circulation of the atmosphere and the oceans. This is a challenging problem both from the theoretical point of view (the study of diffusion and chaos in geophysical systems) and for pratical issues (plankton dynamics or the fate of pollutant spills) [36, 18].
In this thesis, the turbulence of free-surface flows and its effect on the dispersion of floaters like nutrients or pollutants in sea water will be examined. Their dynamics have effects on marine life and on the environment.
Among all, plankton species are known to inhabit the upper sunlit layer of almost all oceans and bodies of fresh water. They obtain energy through the process of photosynthesis and must therefore live in the well-lit surface layer of an ocean, sea, lake or any other body of water, contributing to half of all photosynthetic activity on Earth.
One way to classify different plankton species is by the presence or absence of motility. While some types of phytoplankton are incapable of swimming (referred to as passive particles hereinafter) and remain at the whim of ambient flows, other types of plankton can actively propel themselves through the water flow (referred to as active particles hereinafter).
Assigning realistic and robust values to the many associated parameters in global circulation models is an active area of research. Moreover, since global warming has effects on the changes of vertical stratification of water column, it is fundamental to investigate how thermal stratification affects

the dynamics of passive and active self propelled particles, which is still an open question.

In the next sections some of the well known characteristics of turbulent flows will be reviewed from a phenomenological point of view . In particular, the differences between three and two dimensional turbulence, with emphasis given to surface turbulence, will be discussed. At last, some general consideration about the clustering of particles in turbulence will be given.

1.1 The skeleton of the free-surface turbulence

In the last few years new methodologies have been developed on the Lagrangian description of transport and mixing, coming from the tools of nonlinear dynamics.
The main useful tool to investigate and map the flow into regions of mixing and unmixing is the technique based on Local Lyapunov Exponents which measures the relative dispersion of transported particles [17, 64, 30]. The Local Lyapunov Exponent is a scalar value which characterises the amount of stretching about the trajectory of a point over time and it can be used to study the dispersion in turbulent flow fields.
These exponents are a generalization of Lyapunov Exponents defined for dynamical systems. The Lyapunov Exponent is defined as the exponential rate of separation, averaged over infinite time, of particles trajectories initially separated infinitesimally. Consider $\mathbf{x}(t_0)$ and $\mathbf{x}(t) = \mathbf{x}(t_0) + \delta(t)$ as two particle trajectories separated initially by a distance $\delta(t_0)$ the Lyapunov Exponent is defined by:

$$\lambda = \lim_{t\to\infty} \lim_{\delta(t_0)\to 0} \frac{1}{t} \ln \frac{||\delta(t)||}{||\delta(t_0)||}.$$

This exponent can be either positive or negative indicating exponentially diverging or converging pairs of trajectories. Negative values of λ are characteristic of stable solutions of dissipative systems: Such systems exhibit asymptotic stability. If λ is positive, the orbit is unstable and chaotic and nearby points will diverge to any arbitrary separation.
The Lyapunov Exponent is quite useful in the study of time-independent dynamical systems. However, in the reality, fluids are time-dependent and experimental data are only known over a finite interval of time and space.

To deal with experimental data and to evaluate the previous coefficient by means of numerical simulations, the concept of Finite-Size Lyapunov Exponents (FSLE) has been recently introduced ([3, 2]).
For their simplicity in computing and growing number of applications from the oceanographic to atmospheric flows, these tools have attracted the attention of the oceanic community. The main interest is due to the fact that these coefficients are able to identify the dynamical structures in the fluid transport from the submesoscale to the mesoscale. They detect and display the presence of Lagrangian Coherent Structures (LCSs) which act as a barrier to the mixing properties of flows. These structures are the "skeleton" of the fluid.
In figure 1.1 the Finite Size Lyapunov Exponents (FSLE) at the surface of a turbulent free-surface channel flow are shown (the details of geometry will be provided in Chap. 2). To measure the FSLE at a point r, a reference particle is started from r at time t, simultaneously with another particle at a distance d_0 from r.

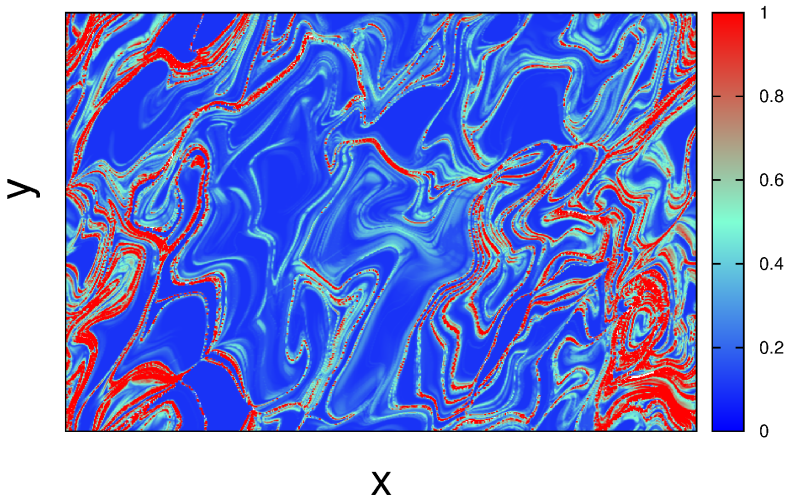

FIGURE 1.1 – Finite Size Lyapunov Exponents computed at turbulent free-surface

The time τ required to reach the separation d_f is measured and the

FSLE is defined as

$$\lambda(r, t, d_0, d_f) = \frac{1}{\tau} \ln \frac{d_f}{d_0}.$$

From the definition it is clear that large values of FSLE indicate regions in which two particles tend to be stretched by the flow and reach rapidly the distance d_f. These regions are very sensitive to the initial conditions and consequently, the flow is chaotic (the so-called Lagrangian chaos ([36]). Regions of high FSLE values are organized in filamentary structures and indicate the unstable manifold that is the largest stretching direction in the fluid. Between the filaments of high FSLE values, there are "valleys" of lower values in which the mixing is poor. The shape of filaments and the extent of the regions with low FSLE values change with time and both depend on the Eulerian characteristics of the flow in a non-trivial way.
The aim of the thesis is to understand the causes of such behaviour and the role of turbulence structures which force the surface.

1.1.1 Phenomenology of free-surface turbulence

As mentioned in the introduction, turbulence is a multiscale non linear phenomenon. The way in which the different scales interact plays a key role in determining how the energy flows.
Few studies of turbulence have been more important than the phenomenology of Kolmogorov-Richardson direct cascade.
To briefly explain this phenomenological picture, it is necessary to start from the Navier Stokes equation

$$\partial_t \mathbf{v} + \mathbf{v} \cdot \nabla \mathbf{v} = -\frac{1}{\rho} \nabla p + \nu \Delta \mathbf{v} + \mathbf{f}$$

where $\mathbf{f}$ is an external driving force, ν and ρ are the viscosity and density of the fluid respectively, p is the pressure. The forcing term is acting on a characteristic scale L and injects energy at an average rate $< \mathbf{f} \cdot \mathbf{v} >= \epsilon$, where the brackets indicate the average over space and time. The nonlinear terms ($\mathbf{v} \cdot \nabla \mathbf{v}$ and ∇p) preserve the total energy and thus simply redistribute it among the modes, i.e. the different scales. Finally, the viscous term dissipates energy at an average rate $\nu \sum_{i,j} \left\langle \left(\partial_j v_i\right)^2 \right\rangle$. The dissipation term is proportional to $\left(\partial_j v_i\right)^2$ which, in Fourier space, means a term proportional to the square of wave number (k^2). This term becomes

important at large wave numbers and thus at very small scales. At statistically stationary states, the rate of energy dissipation balances the input rate $\nu \sum_{i,j} \left\langle \left(\partial_j v_i\right)^2 \right\rangle \sim \epsilon$.

According to the Kolmogorov-Richardson cascade, the system is forced at scale L (the injection scale) and due to nonlinear terms, large scale structures break into smaller and smaller eddies. This cascade ends at scales l_D which are dominated by dissipation. The scales $l_D \ll l \ll L$ are known as inertial range since the main contributions comes from the non-linear (inertial) terms. A first way to look at the distribution of energy among the scales is by looking at the kinetic energy of the Fourier modes in an infinitesimal shell of wave-numbers ($E(k)dk$). It is known from experimental and numerical simulations that the energy spectrum exhibits a universal behaviour which closely follows a power law $E(k) \propto k^{-5/3}$ over the inertial range (figure 1.2(a)).

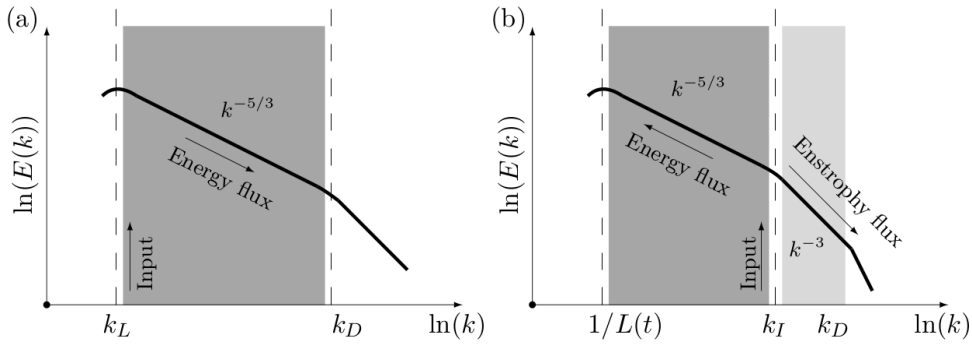

FIGURE 1.2 – Energy spectra for the case of 3D turbulence (a) and 2D turbulence (b)

This power law seems to be independent of the fluid and the detailed geometry of forcing (with a correction due to intermittency introduced in the multifractal model by Parisi and Frisch in 1985). The two crossovers in figure 1.2(a) are respectively the scale at which the energy is forced ($L \sim k_L^{-1}$) and the scale at which the energy is dissipated ($l_D \sim k_D^{-1}$). For $k < k_L$ the spectrum depends on the forcing or boundary condition, for $k > k_L$ it shows a power law decay.

In two-dimensional flows the situation is rather different due to the simultaneous conservation of kinetic energy and enstrophy. As consequence there is an inverse energy cascade from small to larger scales.

The interest in 2D turbulence is supported by the fact that the reversal of the energy flux has been observed in geophysical flows subjected to the Earth's rotation [66, 43] as well as in shallow fluid layer [9, 72] and thermal stratified flows.

In 1967 Kraichnan [34] posed the basis for a theory in 2D flows. The basic idea is that the energy and the enstrophy are injected at a scale L_I (figure 1.2(b)) at a rate $< \mathbf{f} \cdot \mathbf{v} >= \bar{\epsilon}$ and $< (\nabla \wedge \mathbf{f})\omega >= \bar{\eta}$ respectively. Then a double cascade establishes due to nonlinear transfer of energy and enstrophy among the scales: energy flows toward the larger scales ($l > L_I$) (inverse cascade) while enstrophy towards the smaller scales ($l < L_I$) (direct cascade). In figure 1.2(b) the energy of spectra for the 2D case is shown . From dimensional analysis and theoretical derivations, it is known that for $1/L(t) \ll k \ll k_I$, the power spectrum behaves as in 3D turbulence: $E(k) \approx k^{-5/3}\bar{\epsilon}^{-2/3}$ while for $k_I < k < k_D$ it is obtained: $E(k) \approx k^{-3}\bar{\eta}^{-2/3}$.

It is clear from previous discussion that three- and two-dimensional flows are driven by different phenomenologies. Moreover, three-dimensional turbulence is characterized by anomalous scaling and small-scale intermittency [27], whereas the inverse cascade is apparently self-similiar [7]. The transition between the two behaviours has been mainly investigated in models of turbulence where the dimension was introduced as formal parameter [10].

In Chap. 3 how the confinement induced by the presence of the free-surface, causes a direct or inverse cascade, will be discussed. From experiments of free-surface Rashidi and Banerjee [54] as well as from numerical simulation of Pan and Banerjee [48], it was observed that the turbulence near the surface is dominated by upwellings: blobs of fluid impinging on the surface originated from the hairpin vortex in the bottom boundary layer. These regions are separated by downwellings and spiral vortices attached at the surface in a process known as vortex connection. In figure 1.3(a) the vectorial field of velocity at the surface is shown and in figure 1.3(b) a zoom visualise a strong upwelling with the nearby convergent regions.

As discussed in a review article by Sarpakaya [61], the phenomenology of vortex connection is linked to the hairpin vortex ejected from the turbulent bottom boundary layer and approaching the surface. These structures break into sections which remain attached to the surface. The dynamics of upwellings and downwellings guides the energy transfer close to the free surface as observed by Perot and Moin [51, 52] and Nagaosa [45]. Up-

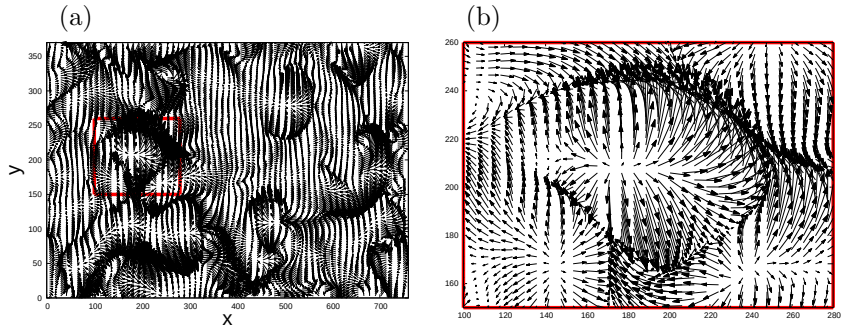

FIGURE 1.3 – Velocity vector field at the surface underlying the upwelling and downwelling (a), (b) shows a zoom of the inset in (a)

wellings are associated to stagnation points at surface with high pressure and a negative gradient of the normal velocity. In a stagnation point, the pressure has a maximum. This leads to a negative vertical component of the pressure-strain correlation. Momentum is transfered to surface-parallel fluctuations. In downwelling, the situation is reversed and energy is transfered from horizontal to vertical fluctuations. Magnaudet [40] showed that these phenomena depends on anisotropy of the turbulence below the free-surface underlying that this behaviour could not be reproduced completely by isotropic decaying turbulence. It remains to understand if the turbulence at the surface is mainly three-dimensional or two-dimensional. Pan and Banerjee [48] noted that the one-dimensional velocity spectra shows a scaling region $\sim k^{-3}$ which is consistent with the prediction of two-dimensional turbulence by Kraichnan. However, Walker [71] showed that the contribution to the production of normal surface vorticity by vortex-stretching has its maximum near the free-surface. This process could not develop, by definition, in two-dimensional flows and it shows a three-dimensional nature of surface.

1.1.2 Phenomenology of particle clustering in turbulence

In this section some general considerations linked to the advection and clustering of particles in flows will be discussed. In particular the analysis will

be focused on a simple model: particles are considered pointwise and their dynamics are driven by viscous and buoyancy forces (as it will be done in Chap. 4). Their motion is driven by the following equations:

$$\frac{d\mathbf{x}_p}{dt} = \mathbf{v}_p \ , \quad \frac{d\mathbf{v}_p}{dt} = \frac{(\rho_p - \rho_f)}{\rho_p}\mathbf{g} + \frac{(\mathbf{u}_{@p} - \mathbf{v}_p)}{\tau_p} \ , \tag{1.1.1}$$

where ρ_p is the density of particles, ρ_f is the density of fluid, $\tau_p = \frac{\rho_p d_p^2}{18\rho_f \nu}$ is the Stokes response time based on particle diameter d_p (ν is the fluid viscosity). Note that if $\rho_p = \rho_f$ the first term is zero and corresponds to neutrally buoyant particles, if $\rho_p < \rho_f$ the first term is negative and it is the case of particles lighter than surrounding fluid, while if $\rho_p > \rho_f$ is the case of particles heavier than fluid.

When the particles are small and their densities are comparable with the carrying fluid they usually follow the local fluid motion. If any of these conditions are not fulfilled, the dynamics of the particles deviate from those of the fluid. Such particles are generically called "inertial particles". The situation becomes more complicated if the particles are "active", e.g. if they can self-propel, such as microorganisms in the ocean (which will be discussed in Chap. 5), or if the particles exchange mass, momentum or energy with the carrying fluid, such as water droplets in clouds. Here the case of inertial particles will be considered.

In real situations, the fluid evolves with Navier-Stokes equation and the most interesting feature which arises for inertial particles, is the particle clustering namely strongly inhomogeneous distributions. By following Cencini et al. [11] and Bec [5], an explanation of such phenomenology could be done using the dynamic system theory. The previous equations 1.1.1 could be written in a more compact form $\frac{d\mathbf{z}}{dt} = \mathbf{F}(\mathbf{z}, t)$ where $\mathbf{z} = (\mathbf{x}, \mathbf{v})$ and $\mathbf{F} = \left[\mathbf{v}, \frac{\rho_p - \rho_f}{\rho_p}\mathbf{g} + \frac{\mathbf{u}-\mathbf{v}}{\tau_p}\right]$. In a 3-dimensional flow (or in general d-dimensional flow), particles live in a 6-phase space ($2d$ in general) and if an attractor exists, it will have a fractal dimension $\bar{\nu} < 6$ where in the simple model that we have considered $\bar{\nu}$ is only function of τ_p and the ratio between the density of the particles and the density of the flow. If we do the divergence of $\mathbf{F}$ we have that $\nabla \cdot \mathbf{F} = -\frac{3}{\tau_p}$ which means that phase-space volumes contract with rate $-3/\tau_p$ [11].
In the limit case in which $\tau_p \to 0$ the contraction $\nabla \cdot \mathbf{F} = -\infty$. In this case the dynamics of particles correspond to that of tracers and $\bar{\nu} = 3$: the at-

tractor space coincides with the coordinate space. No clustering occurs and particles will sample uniformly the space (note that this is in the hypothesis in which particles are advected by an incompressible flow). In the other limit case $St \to \infty$ it results $\nabla \cdot \mathbf{F} = 0$ which correspond to a conservative dynamics in the full $6-$ dimensional space. Also in this case no clustering occurs. Between these two limits, it could happen that clustering is observed ([11], [5]) and the effective velocity field of particles is compressible even if the underlying fluid field is incompressible. Inertial particles form clusters so that their ensemble behaves like a compressible fluid.
Based on this observation, an original way to compute the local concentration of particles by means of the Jacobian ($\mathbf{J}(t)$) of particle path, evaluated along the trajectory of each single particle, was proposed in [53, 31]. Given the initial conditions of particles $\mathbf{X}_0$, the Jacobian $\mathbf{J}(t)$ is equal to the $\det\left[\frac{\partial \mathbf{X}_{p,i}(\mathbf{X_0},t)}{\partial \mathbf{X}_{0,j}}\right]$ and quantifies the dilatation/compression of the initial volume associated to the particles.

Starting from an uniform distribution ($\mathbf{J}(t=0)=1$), $\mathbf{J}(t)$ gives a map of particle field. Moreover $\mathbf{J}(t)$ can be related to the divergence of the particle velocity field:

$$\frac{\mathrm{d}\ \ln|\mathbf{J}(t)|}{\mathrm{d}\ \mathrm{t}} = \nabla \cdot \mathbf{u_p}.$$

The divergence of the particle velocity field represents the relative rate of change of the dilatation/compression following a particle path [1]. The authors in [53, 31] find that inertial particles sample preferentially flow regions in which their local concentration is higher with respect to the initial conditions.
On the other hand, clustering could occur also in the case in which particles (even tracers) are advected by a compressible flow and follow the streamline (Boffetta et al [8]). The picture which arises is that the clustering is a general consequence of compressibility.

Surface Eulerian compressibility will be introduced in Chap. 3 and its effect on the dynamic of the buoyant passive particles, which float on the surface, will be shown in Chap. 4.

Thesis outline

The present work is structured as follows:

- Chap. 2: the governing equations and the numerical method are reported and discussed in detail; in the first section, the geometry of problem and the equation for the neutrally buoyant and stable stratified turbulence, are reported. In the second and third sections the numerical approach and the solution procedure are provided; in the third and fourth sections the spectral approximation of the solution is shown and the discretized set of equations is reported. In the last section information about lagrangian particle tracking is provided.

- Chap. 3: turbulence of free-surface is investigated. In the first section once the flow field statistics for the neutrally buoyant turbulent open channel flow are provided, the spectral energy fluxes and the effect of compressibility at the free surface, will be exposed. In the last section, the case of stable stratification and the main statistics to characterize the surface will be discussed in detail.

- Chap. 4: the transport of passive buoyant particles in turbulent open channel flow will be discussed. In the first section the problem is posed and the details of the simulations are provided; in the second section the clustering of particles at surface and their temporal persistence are discussed in detail for the case of neutrally buoyant flow. In the last section, the phenomena of surfacing and clustering in stable stratified open channel flow, will be discussed in detail.

- Chap. 5: the behaviour of self-propelled particles in turbulent open channel flow will be introduced. In the first section the problem is described, providing the details of the simulations. In the remaining part of chapter preliminary results, linked to the dynamics of active particles and their interaction with the stratification, will be exposed.

The results presented in this thesis are partially reproduced from the following pubblications:

- S. Lovecchio, C. Marchioli, and A. Soldati, "Time persistence of floating-particle clusters in free-surface turbulence", Physical Review E **88**,(2013): 033003;

- S. Lovecchio, F. Zonta, and A. Soldati, "Influence of thermal stratification on the surfacing and clustering of floaters in free surface turbulence", Advances in Water Resources **72**, (2014);
- S. Lovecchio, F. Zonta, and A. Soldati, "Inverse energy cascade and flow topology in free surface turbulence", accepted in Physical Review E (2015);
- S. Lovecchio, and A. Soldati, "Effects of thermal stratification on phytoplankton surfacing", in preparation.

I

Methodology

2

Governing equations & Numerical methods

In the first part of this chapter the equations used to describe the dynamics of an incompressible viscous fluid flow with heat transfer are derived. In the second part of the chapter the numerical method employed to solve the balance equations is presented and discussed in detail. In the third section the Lagrangian Particle Tracking algorithm is introduced.

2.1 Governing equations

In the continuum approach the dynamics of fluids are governed by the balance equations of mass, momentum and energy. These equations, together with the constitutive laws for the stress tensor and for the conductive heat flux, can describe the motion of any kind of fluid flow. With reference to the schematic of Fig.2.1, we consider an incompressible and Newtonian turbulent flow of water in a plane channel with differentially-heated walls.

The reference geometry consists of two infinite flat parallel walls; the origin of the coordinate system is located at the center of the channel and the x, y and $z-$axis point in the streamwise, spanwise and wall-normal directions. Indicating with h the channel height, the size of the channel is $2\pi h \times \pi h \times h$, in $x-$, $y-$ and $z-$ axis respectively.

For the fluid velocity, no-slip (resp. no-stress) boundary conditions are enforced at the bottom (resp. top) boundary.

For the fluid temperature, a constant heat flux (resp. adiabatic condition) is enforced at the top (resp. bottom) boundary (Taylor et al., 2005). Note that periodicity is applied in x and y for both velocity and temperature.

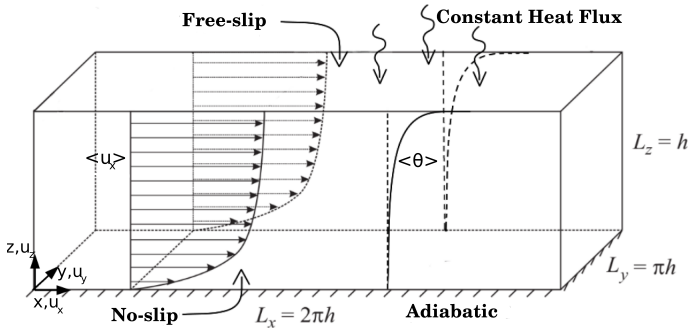

FIGURE 2.1 – Sketch of the computational domain

Due to the free surface heating there is a negative temperature difference between the bottom and the top layers of the channel which causes a stable buoyancy effect (the gravitational acceleration g acting downward along the wall-normal direction).

The governing equations are non-dimensionalised with the channel height h, the friction velocity $u_\tau = \sqrt{\frac{\tau_w}{\rho_{\text{ref}}}}$, and the value of the imposed free-surface temperature gradient $\frac{\partial \theta}{\partial z}\Big|_s$ where subscript s indicates the position of surface.

The shear stress τ_w used to define the friction velocity is the horizontally averaged value of τ at the wall which must balance the vertically integrated pressure gradient for the steady state.

With the previous choices the governing balance equations in dimensionless form read as:

$$\frac{\partial u_i}{\partial x_i} = 0 \ , \tag{2.1.1}$$

$$\frac{\partial u_i}{\partial t} = S_i + \frac{1}{Re_\tau}\left(\frac{\partial^2 u_i}{\partial {x_j}^2}\right) - \frac{\partial p}{\partial x_i} \ , \tag{2.1.2}$$

$$\frac{\partial \theta}{\partial t} = S_\theta + \frac{1}{Re_\tau Pr}\left(\frac{\partial^2 \theta}{\partial {x_j}^2}\right) - \beta_T \tag{2.1.3}$$

where u_i is the i^{th} component of the velocity vector.

The S-terms contain the non-linear convective terms, the dimensionless

mean pressure gradient and the buoyancy term:

$$S_i = -u_j \frac{\partial u_i}{\partial x_j} + \delta_{i,1} + \delta_{i,3} \frac{Gr}{Re_\tau^2} \theta, \tag{2.1.4}$$

$$S_\theta = -u_j \frac{\partial \theta}{\partial x_j} \ . \tag{2.1.5}$$

In the above equations, $\delta_{i,1}$ is the mean pressure gradient that drives the flow in the streamwise direction while $\delta_{i,3}$ is the Kronecker delta (used to account for the buoyancy term in the wall-normal direction).

Eqs. 2.1.1-2.1.3 are subject to the following boundary conditions:

$$@ \text{ Wall: } u_x = u_y = u_z = 0, \frac{\partial \theta}{\partial z} = 0 \tag{2.1.6}$$

$$@ \text{ Free-surface: } \frac{\partial u_x}{\partial z} = \frac{\partial u_y}{\partial z} = u_z = 0, \frac{\partial \theta}{\partial z} = 1 \tag{2.1.7}$$

The dimensionless Reynolds, Grashof and Prandtl numbers are defined as

$$Re_\tau = \frac{u_\tau h}{\nu}, \qquad Gr = \frac{g\beta h^3}{\nu^2} \frac{\partial \theta}{\partial z} \Big|_s \ , \qquad Pr = \frac{\mu c_p}{\lambda} \ . \tag{2.1.8}$$

where μ and ν are the dynamic and the kinematic viscosity, β is the thermal expansion coefficient, c_p is the specific heat and λ is the thermal conductivity.

The key parameter for stratified flows is the shear Richardson number $Ri_\tau = Gr/Re_\tau^2$, which is the ratio between buoyancy and inertia. Note that $\beta_T = 1/(Re_\tau Pr)$ in Eq. 2.1.3, and depends on the specific flow configuration considered here (an open channel flow with a constant surface heating). Specifically, the temperature field inside the channel may be written as:

$$\theta = \theta_1(t) + \theta(\mathbf{x}, t), \tag{2.1.9}$$

where θ_1 is the deterministic temperature field (which increases in time owing to the imposed surface heating), while $\theta(\mathbf{x}, t)$ is the turbulent temperature field (statistically steady). The substitution of Eq. 2.1.9 into the energy equation

$$\frac{\partial \theta}{\partial t} = -u_j \frac{\partial \theta}{\partial x_j} + \frac{1}{Re_\tau Pr} \frac{\partial^2 \theta}{\partial x_j^2}. \tag{2.1.10}$$

gives

$$\frac{d\theta_1}{dt} + \frac{\partial\theta}{\partial t} = -u_j \frac{\partial\theta}{\partial x_j} + \frac{1}{Re_\tau Pr}\frac{\partial^2\theta}{\partial x_j^2}. \tag{2.1.11}$$

Using the Reynolds average, Eq. 2.1.11 becomes

$$\frac{d\theta_1}{dt} = -\frac{\partial\langle\theta' w'\rangle}{\partial z} + \frac{1}{Re_\tau Pr}\frac{\partial^2\langle\theta\rangle}{\partial z^2}. \tag{2.1.12}$$

The right-hand side (rhs) of Eq. 2.1.12 is only a function of space (since $\theta(\mathbf{x}, t)$ is a statistically steady field) while the left-hand side (lhs) is only a function of time. Consequently Eq. 2.1.12 is satisfied only when rhs and lhs are constant. To compute the value of the constant, we integrate Eq. 2.1.12 from $z = 0$ (wall, subscript w) to $z = 1$ (free-surface, subscript s):

$$\int_0^1 \frac{d\theta_1}{dt} dz = \frac{1}{Re_\tau Pr}\left[\frac{\partial\theta}{\partial z}\Big|_s - \frac{\partial\theta}{\partial z}\Big|_w\right]. \tag{2.1.13}$$

Using the boundary conditions (see Eq. 2.1.6-2.1.7), we obtain

$$\frac{d\theta_1}{dt} = \frac{1}{Re_\tau Pr} \tag{2.1.14}$$

and

$$\theta_1(t) = \frac{t}{Re_\tau Pr} + C. \tag{2.1.15}$$

From Eq. 2.1.15 we note that the deterministic temperature field θ_1 increases lineraly in time. Since we are interested in the behavior of the turbulent temperature field θ only, we subtract the temperature changes due to θ_1 from the energy balance equation. Therefore, the governing balance equation for the temperature field (Eq. 2.1.3) becomes:

$$\frac{\partial\theta}{\partial t} + u_j \frac{\partial\theta}{\partial x_j} = \frac{1}{Re_\tau Pr}\left(\frac{\partial^2\theta}{\partial {x_j}^2}\right) - \beta_T, \tag{2.1.16}$$

where $\beta_T = d\theta_1/dt = 1/Re_\tau Pr$.

It is evident that Eqs. 2.1.1-2.1.5 include buoyancy effects. However, the same equations can be used to analyse neutrally-buoyant flows, simply assuming a vanishing Grashof number ($Gr = 0$).

Eqs. 2.1.1-2.1.3 are discretized using a pseudo-spectral method based on transforming the field variables into the wavenumber space, through a Fourier representation for the periodic (homogeneous) directions x and y,

and a Chebychev representation for the wall-normal (non- homogeneous) direction z. A two-level explicit Adams-Bashfort scheme for the non-linear terms and an implicit Crank-Nicolson method for the viscous terms are employed for the time advancement. As commonly done in pseudospectral method, the convective non-linear terms are first computed in physical space and then transformed in the wavenumber space using a de-aliasing procedure based on the 2/3-rule; derivatives are evaluated directly in the wavenumber space to maintain spectral accuracy. Further details will be provided in next section.

2.2 Numerical approach

Throughout this thesis we will analyse different physical problems (stratified/unstratified flows). However, the structure of the governing equations does not change from one situation to another, as we have observed in Sec. 2.1. As a consequence, a unique numerical scheme can be adopted to analyse all the problems. Without loss of generality, we will take the simulations with thermal stratification as reference. Indeed, the numerical approach developed for the solution of Eqs.(2.1.1)-(2.1.3) is discussed. In this section it is preferred to refer to x,y,z (streamwise, spanwise and wall normal direction respectively) to as x_1, x_2, x_3 and the same is true for u_x, u_y, u_z which will be referred to as u_1, u_2, u_3.

2.3 Solution procedure

The present scheme solves for the balance equations of motion (Eqs. 2.1.1-2.1.3) through the elimination of pressure. The pressure field can be removed upon taking the curl of Eq. (2.1.2), to give:

$$\frac{\partial \omega_k}{\partial t} = \epsilon_{ijk} \frac{\partial S_j}{\partial x_i} + \frac{1}{Re} \nabla^2 \omega_k, \tag{2.3.1}$$

where $\omega_k = \epsilon_{ijk} \frac{\partial u_j}{\partial x_i}$ is the $k-th$ component of the vorticity vector. Taking twice the curl of Eq. (2.1.2) and using Eq. (2.1.1) together with the vectorial identity $\nabla \times (\nabla \times \mathbf{v}) = \nabla(\nabla \cdot \mathbf{v}) - \nabla^2 \mathbf{v}$, a 4^{th}-order equation in u_i can be obtained:

$$\frac{\partial (\nabla^2 u_i)}{\partial t} = \nabla^2 S_i - \frac{\partial}{\partial x_i} \left(\frac{\partial S_j}{\partial x_j} \right) + \frac{1}{Re} \nabla^4 u_i. \tag{2.3.2}$$

Eqs. (2.3.1)-(2.3.2) can be written with respect to the normal components, *i.e.* for ω_3 and u_3:

$$\frac{\partial \omega_3}{\partial t} = \frac{\partial S_2}{\partial x_1} - \frac{\partial S_1}{\partial x_2} + \frac{1}{Re}\nabla^2 \omega_3. \tag{2.3.3}$$

$$\frac{\partial (\nabla^2 u_3)}{\partial t} = \nabla^2 S_3 - \frac{\partial}{\partial x_3}\left(\frac{\partial S_j}{\partial x_j}\right) + \frac{1}{Re}\nabla^4 u_3. \tag{2.3.4}$$

These two equations are numerically solved for ω_3 and u_3. With ω_3 and u_3 known, u_1 and u_2 can be obtained by solving the following equations simultaneously

$$\frac{\partial u_1}{\partial x_1} + \frac{\partial u_2}{\partial x_2} = -\frac{\partial u_3}{\partial x_3}, \tag{2.3.5}$$

$$\frac{\partial u_2}{\partial x_1} - \frac{\partial u_1}{\partial x_2} = \omega_3. \tag{2.3.6}$$

Here, Eqs. (2.3.5) and (2.3.6) derive, respectively, from continuity and from the definition of vorticity. Although not needed for the time advancement of the solutions, pressure can be obtained by solving a Poisson-type equation after all velocity components have been found:

$$\nabla^2 p = \frac{\partial S_j}{\partial x_j}. \tag{2.3.7}$$

Once the velocity field is known, the temperature field can be obtained from the solution of the energy balance equation:

$$\frac{\partial \theta}{\partial t} = S_\theta + \frac{1}{Re_\tau Pr}\left(\frac{\partial^2 \theta}{\partial {x_j}^2}\right) - \beta_T. \tag{2.3.8}$$

2.4 Spectral representation of solutions

To represent the solution in space, finite Fourier expansion in the homogeneous (x_1 and x_2) directions is used:

$$f(x_1, x_2, x_3) = \sum_{|n_1|}^{\frac{N_1}{2}} \sum_{|n_2|}^{\frac{N_2}{2}} \hat{f}(k_1, k_2, x_3) e^{i(k_1 x_1 + k_2 x_2)}, \tag{2.4.1}$$

where $\hat{f}$ represents the Fourier coefficients of a general dependent function, $i = \sqrt{-1}$, N_1 and N_2 are the number of Fourier modes retained in the series,

and the summation indices n_1 and n_2 are chosen so that $-\frac{N_1}{2}+1 \leq n_1 \leq \frac{N_1}{2}$ and $-\frac{N_2}{2}+1 \leq n_2 \leq \frac{N_2}{2}$. The wavenumbers k_1 and k_2 are given by:

$$k_1 = \frac{2\pi n_1}{L_1} \tag{2.4.2}$$

$$k_2 = \frac{2\pi n_2}{L_2}, \tag{2.4.3}$$

with L_1 and L_2 being the periodicity lengths in the streamwise and spanwise directions. Because of the orthogonality of the Fourier functions, the Fourier transform $\hat{f}$ can be obtained as:

$$\hat{f}(k_1, k_2, x_3) = \frac{1}{N_1 N_2} \sum_{|n_1|}^{\frac{N_1}{2}} \sum_{|n_2|}^{\frac{N_2}{2}} f(x_1, x_2, x_3) e^{-i(k_1 x_1 + k_2 x_2)}, \tag{2.4.4}$$

where x_1 and x_2 are chosen to be the transform locations

$$x_1 = \frac{n_1}{N_1} L_1 \tag{2.4.5}$$

$$x_2 = \frac{n_2}{N_2} L_2. \tag{2.4.6}$$

In the cross-stream (wall-normal) direction x_3, Chebyshev polynomials are used to represent the solution,

$$\hat{f}(k_1, k_2, x_3) = \sum_{n_3=0}^{N_3'} a(k_1, k_2, n_3) T_n(x_3), \tag{2.4.7}$$

where the prime denotes that the first term is halved. The Chebyshev polynomial of order n_3 in x_3 is defined as

$$T_{n_3}(x_3) = \cos(n_3 \arccos(x_3)), \tag{2.4.8}$$

with $-1 \leq x_3 \leq 1$. Orthogonality also exist for Chebyshev polynomials, which leads to the following inverse transformation:

$$\hat{a}(k_1, k_2, n_3) = \frac{2}{N_3} \sum_{n_3=0}^{N_3'} \hat{a}(k_1, k_2, x_3) T_{n_3}(x_3). \tag{2.4.9}$$

In physical space the collocation points along the cross-stream direction are related to Chebyshev indexes in the following way:

$$x_3 = \cos\left(\frac{n_3\pi}{N_3}\right). \tag{2.4.10}$$

The advantage of using Chebyshev polynomials to represent the solution in the cross-stream direction is that such a representation gives very good resolution in the regions close to the boundaries, because the collocation points bunch up there [1]. For in-depth discussion on Chebyshev polynomials and their applications in numerical analysis, see Fox and Parker [26]. Therefore the spectral representation (in all three directions) of a generic dependent variable takes the final form

$$f(x_1,x_2,x_3) = \sum_{|n_1|}^{\frac{N_1}{2}} \sum_{|n_2|}^{\frac{N_2}{2}} \sum_{n_3=0}^{N_3'} \hat{a}(k_1,k_2,n_3) e^{i(k_1x_1+k_2x_2)} T_{n_3}(x_3). \tag{2.4.11}$$

2.5 Discretization of the equations

Momentum equations

With the spectral representation given by Eq.(2.4.1), Eq.(2.3.4) can be written as:

$$\begin{aligned}\frac{\partial}{\partial t}\left(\frac{\partial^2}{\partial x_3^2}-k^2\right)\hat{u}_3 = &\left(\frac{\partial^2}{\partial x_3^2}-k^2\right)\hat{S}_3 \\ &-\frac{\partial}{\partial x_3}\left(ik_1\hat{S}_1+ik_2\hat{S}_2+\frac{\partial}{\partial x_3}\hat{S}_3\right) \\ &+\frac{1}{Re}\left(\frac{\partial^2}{\partial x_3^2}-k^2\right)\left(\frac{\partial^2}{\partial x_3^2}-k^2\right)\hat{u}_3,\end{aligned} \tag{2.5.1}$$

where $k^2 = k_1^2 + k_2^2$. Time advancement of Eq. (2.5.1) is done using a two-level explicit Adams-Bashfort scheme for the convective terms and an implicit Crank-Nicholson method for the diffusion terms. The time-differenced

[1] In wall bounded flows, resolution close to the wall is very important, since large gradients of the solutions occur there

form of Eq. (2.5.1), based on the above schemes, is

$$\begin{aligned}\left(\frac{\partial^2}{\partial x_3^2}-k^2\right)\frac{(\hat{u}_3^{n+1}-\hat{u}_3^n)}{\Delta t} =& \frac{3}{2}\left(\frac{\partial^2}{\partial x_3^2}-k^2\right)\hat{S}_3^n-\frac{1}{2}\left(\frac{\partial^2}{\partial x_3^2}-k^2\right)\hat{S}_3^{n-1}\\ &-\frac{\partial}{\partial x_3}\,ik_1(\frac{3}{2}\hat{S}_1^n-\frac{1}{2}\hat{S}_1^{n-1})\\ &-\frac{\partial}{\partial x_3}\,ik_2(\frac{3}{2}\hat{S}_2^n-\frac{1}{2}\hat{S}_2^{n-1})\\ &-\frac{\partial^2}{\partial x_3^2}(\frac{3}{2}\hat{S}_3^n-\frac{1}{2}\hat{S}_3^{n-1})\\ &+\frac{1}{Re}\left(\frac{\partial^2}{\partial x_3^2}-k^2\right)\left(\frac{\partial^2}{\partial x_3^2}-k^2\right)\frac{(\hat{u}_3^{n+1}+\hat{u}_3^n)}{2},\end{aligned} \tag{2.5.2}$$

where superscripts $n-1$, n and $n+1$ indicate three successive time levels. By defining $\gamma=\frac{\Delta t}{2\ Re}$ we can rearrange Eq. (2.5.2):

$$\begin{aligned}&\left[1-\gamma\left(\frac{\partial^2}{\partial x_3^2}-k^2\right)\right]\left(\frac{\partial^2}{\partial x_3^2}-k^2\right)\hat{u}_3^{n+1}=\\ &-k^2(\frac{3}{2}\hat{S}_3^n-\frac{1}{2}\hat{S}_3^{n-1})\Delta t\\ &-\frac{\partial}{\partial x_3}\,ik_1(\frac{3}{2}\hat{S}_1^n-\frac{1}{2}\hat{S}_1^{n-1})\Delta t\\ &-\frac{\partial}{\partial x_3}\,ik_2(\frac{3}{2}\hat{S}_2^n-\frac{1}{2}\hat{S}_2^{n-1})\Delta t\\ &+(\gamma\frac{\partial^2}{\partial x_3^2}+(1-\gamma k^2))\left(\frac{\partial^2}{\partial x_3^2}-k^2\right)\hat{u}_3^n.\end{aligned} \tag{2.5.3}$$

Introducing $\beta^2=\frac{1+\gamma k^2}{\gamma}$ and recalling that $\frac{\partial\hat{u}_3}{\partial x_3}=-ik_1\hat{u}_1-ik_2\hat{u}_2$ from continuity, we can manipulate the last term on the rhs of Eq. (2.5.3):

$$\begin{aligned}&-\gamma\left(\frac{\partial^2}{\partial x_3^2}-\beta^2\right)\left(\frac{\partial^2}{\partial x_3^2}-k^2\right)\hat{u}_3^{n+1}=\\ &-k^2(\frac{3}{2}\hat{S}_3^n-\frac{1}{2}\hat{S}_3^{n-1})\Delta t-k^2(\gamma\frac{\partial^2}{\partial x_3^2}+(1-\gamma k^2))\hat{u}_3^n\\ &-\frac{\partial}{\partial x_3}\,ik_1(\frac{3}{2}\hat{S}_1^n-\frac{1}{2}\hat{S}_1^{n-1})\Delta t-\frac{\partial}{\partial x_3}\,ik_1(\gamma\frac{\partial^2}{\partial x_3^2}+(1-\gamma k^2))\hat{u}_1^n\\ &-\frac{\partial}{\partial x_3}\,ik_2(\frac{3}{2}\hat{S}_2^n-\frac{1}{2}\hat{S}_2^{n-1})\Delta t-\frac{\partial}{\partial x_3}\,ik_2(\gamma\frac{\partial^2}{\partial x_3^2}+(1-\gamma k^2))\hat{u}_2^n\end{aligned} \tag{2.5.4}$$

.

By introducing the historical terms:

$$\begin{aligned}
\hat{H}_1^n &= (\frac{3}{2}\hat{S}_1^n - \frac{1}{2}\hat{S}_1^{n-1})\Delta t + (\gamma\frac{\partial^2}{\partial x_3^2} + (1-\gamma k^2))\hat{u}_1^n, \\
\hat{H}_2^n &= (\frac{3}{2}\hat{S}_2^n - \frac{1}{2}\hat{S}_2^{n-1})\Delta t + (\gamma\frac{\partial^2}{\partial x_3^2} + (1-\gamma k^2))\hat{u}_2^n, \\
\hat{H}_3^n &= (\frac{3}{2}\hat{S}_3^n - \frac{1}{2}\hat{S}_3^{n-1})\Delta t + (\gamma\frac{\partial^2}{\partial x_3^2} + (1-\gamma k^2))\hat{u}_3^n,
\end{aligned} \tag{2.5.5}$$

Eq. (2.5.4) becomes:

$$\left(\frac{\partial^2}{\partial x_3^2} - \beta^2\right)\left(\frac{\partial^2}{\partial x_3^2} - k^2\right)\hat{u}_3^{n+1} = \frac{1}{\gamma}(k^2\hat{H}_3^n + \frac{\partial}{\partial x_3}(ik_1\hat{H}_1^n + ik_2\hat{H}_2^n)). \tag{2.5.6}$$

If we put $\hat{H}^n = k^2\hat{H}_3^n + \frac{\partial}{\partial x_3}(ik_1\hat{H}_1^n + ik_2\hat{H}_2^n)$ we come to the final form of the equation:

$$\left(\frac{\partial^2}{\partial x_3^2} - \beta^2\right)\left(\frac{\partial^2}{\partial x_3^2} - k^2\right)\hat{u}_3^{n+1} = \frac{\hat{H}^n}{\gamma}. \tag{2.5.7}$$

Defining $\hat{\phi} = \left(\frac{\partial^2}{\partial x_3^2} - k^2\right)\hat{u}_3^{n+1}$ the above fourth-order equation becomes a system of two second-order equations:

$$\left(\frac{\partial^2}{\partial x_3^2} - \beta^2\right)\hat{\phi} = \frac{\hat{H}^n}{\gamma}, \tag{2.5.8}$$

$$\left(\frac{\partial^2}{\partial x_3^2} - k^2\right)\hat{u}_3^{n+1} = \hat{\phi}. \tag{2.5.9}$$

These equations are solved with the following four boundary conditions:

$$\begin{aligned}
&\hat{u}_3^{n+1}(\pm 1) = 0 && (a) \\
&\frac{\partial\hat{u}_3^{n+1}}{\partial x_3}(+1) = 0 && (b) \\
&\frac{\partial^2\hat{u}_3^{n+1}}{\partial x_3^2}(-1) = 0 && (c)
\end{aligned} \tag{2.5.10}$$

where $x_3 = z = +1$ indicates the wall and $x_3 = z = -1$ indicates the surface. The conditions (b) and (c) are obtained from applying the

continuity equation at the wall (condition (b)) and its derivative in x_3 at the free-slip surface (condition c).

The lack of real boundary conditions for $\hat{\phi}$ can be circumvented by decomposing it into three parts:

$$\hat{\phi} = \hat{\phi}_1 + \hat{A}\phi_2 + \hat{B}\phi_3, \tag{2.5.11}$$

where constants $\hat{A}$ and $\hat{B}$ are to be determined. These three individual components of $\hat{\phi}$ satisfy:

$$\begin{aligned}
&\left(\frac{\partial^2}{\partial x_3^2} - \beta^2\right)\hat{\phi}_1 = \frac{\hat{H}^n}{\gamma}, \qquad \hat{\phi}_1(1) = 0, \qquad \hat{\phi}_1(-1) = 0;\\
&\left(\frac{\partial^2}{\partial x_3^2} - \beta^2\right)\phi_2 = 0, \qquad \phi_2(1) = 0, \qquad \phi_2(-1) = 1;\\
&\left(\frac{\partial^2}{\partial x_3^2} - \beta^2\right)\phi_3 = 0, \qquad \phi_3(1) = 1, \qquad \phi_3(-1) = 0.
\end{aligned} \tag{2.5.12}$$

Likewise $\hat{u}_3^{n+1}$ can be splitted into:

$$\hat{u}_3 = \hat{u}_{3,1} + \hat{A}u_{3,2} + \hat{B}u_{3,3}. \tag{2.5.13}$$

Once the solution of Eqs. (2.5.12) has been carried out, we can solve:

$$\begin{aligned}
&\left(\frac{\partial^2}{\partial x_3^2} - \beta^2\right)\hat{u}_{3,1} = \hat{\phi}_1, \qquad \hat{u}_{3,1}(1) = 0, \qquad \hat{u}_{3,1}(-1) = 0,\\
&\left(\frac{\partial^2}{\partial x_3^2} - \beta^2\right)u_{3,2} = \phi_2, \qquad u_{3,2}(1) = 0, \qquad u_{3,2}(-1) = 0,\\
&\left(\frac{\partial^2}{\partial x_3^2} - \beta^2\right)u_{3,3} = \phi_3, \qquad u_{3,3}(1) = 0, \qquad u_{3,3}(-1) = 0.
\end{aligned} \tag{2.5.14}$$

Finally the unknown constants $\hat{A}$ and $\hat{B}$ are determined by applying the boundary conditions of Eq. (2.5.10b) to $\hat{u}_3^{n+1}$ written in terms of its components:

$$\begin{aligned}
&\frac{\partial \hat{u}_{3,1}}{\partial x_3}(1) + \hat{A}\frac{\partial u_{3,2}}{\partial x_3}(1) + \hat{B}\frac{\partial u_{3,3}}{\partial x_3}(1) = 0,\\
&\frac{\partial \hat{u}_{3,1}}{\partial x_3}(-1) + \hat{A}\frac{\partial u_{3,2}}{\partial x_3}(-1) + \hat{B}\frac{\partial u_{3,3}}{\partial x_3}(-1) = 0.
\end{aligned} \tag{2.5.15}$$

With $\hat{A}$ and $\hat{B}$ determined, $\hat{u}_3^{n+1}$ is fully known. The above system of equations are solved using a Chebyshev method so the solutions $\hat{u}_3^{n+1}$ will

be represented by Chebyshev coefficients in the wall normal direction x_3. Therefore, the solution $\hat{u}_3^{n+1}$ will be function of k_1, k_2 and n_3:

$$\hat{u}_3^{n+1} = \hat{u}_3^{n+1}(k_1, k_2, n_3), \tag{2.5.16}$$

where $0 < n_3 < N_3$, N_3 being the number of coefficients and collocation points in the wall-normal direction. Recalling Eq.(2.4.1), the solution in space will read as:

$$u_3^{n+1}(x_1, x_2, x_3) = \sum_{|n_1|}^{\frac{N_1}{2}} \sum_{|n_2|}^{\frac{N_2}{2}} \sum_{n_3=0}^{N_3'} \hat{u}_3^{n+1}(k_1, k_2, n_3) e^{i(k_1 x_1 + k_2 x_2)} T_{n_3}(x_3), \tag{2.5.17}$$

The other two velocity components will be determined through the normal vorticity component $\hat{\omega}_3$. Following a discretization procedure similar to that of Eq. (2.3.4) we can write:

$$\left(\frac{\partial^2}{\partial x_3^2} - \beta^2\right) \hat{\omega}_3^{n+1} = -\frac{(ik_1 \hat{H}_2^n - ik_2 \hat{H}_1^n)}{\gamma}, \tag{2.5.18}$$

with boundary conditions:

$$\hat{\omega}_3^{n+1} = ik_1 \hat{u}_2 - ik_2 \hat{u}_1 = 0 \qquad x_3 = +1, \tag{2.5.19}$$

$$\frac{\partial \hat{\omega}_3^{n+1}}{\partial x_3} = ik_1 \frac{\partial \hat{u}_2}{\partial x_3} - ik_2 \frac{\partial \hat{u}_1}{\partial x_3} = 0 \qquad x_3 = -1. \tag{2.5.20}$$

Once vorticity is known, $\hat{u}_1^{n+1}$ and $\hat{u}_2^{n+1}$ can be determined from solving:

$$-ik_2 \hat{u}_1^{n+1} + ik_1 \hat{u}_2^{n+1} = \hat{\omega}_3^{n+1}, \tag{2.5.21}$$

$$ik_1 \hat{u}_1^{n+1} + ik_2 \hat{u}_2^{n+1} = -\frac{\partial \hat{u}_3^{n+1}}{\partial x_3}, \tag{2.5.22}$$

that come from the definition of $\hat{\omega}_3$ and from continuity equation, respectively. Pressure can be calculated by the transformed Poisson equation Eq. (2.3.7):

$$\left(\frac{\partial^2}{\partial x_3^2} - \beta^2\right) \hat{p}^{n+1} = ik_1 \hat{S}_1^{n+1} + ik_2 \hat{S}_2^{n+1} + \frac{\partial \hat{S}_3^{n+1}}{\partial x_3}. \tag{2.5.23}$$

Boundary conditions for $\hat{p}^{n+1}$ can be obtained by the transformed form of Eq. (3.3.2) in the x_3 direction applied at $x_3 = \pm 1$.

The above scheme is used to evaluate the solutions in Fourier-Chebyshev space for $k^2 \neq 0$. The case $k^2 = 0$ corresponds to the solution averaged over an $x_1 - x_2$ plane. In this case the solution procedure is simpler: upon time discretization the x_1 and x_2 components of Eq. (2.1.2) in Fourier-Chebyshev space after time discretization give:

$$\left(\frac{\partial^2}{\partial x_3^2} - \frac{1}{\gamma}\right)\hat{u}_1^{n+1} = -\frac{\hat{H}_1}{\gamma}, \tag{2.5.24}$$

$$\left(\frac{\partial^2}{\partial x_3^2} - \frac{1}{\gamma}\right)\hat{u}_2^{n+1} = -\frac{\hat{H}_2}{\gamma}, \tag{2.5.25}$$

that can be solved by applying the following boundary conditions:

$$\hat{u}_1^{n+1} = \hat{u}_2^{n+1} = 0 \qquad x_3 = +1 \tag{2.5.26}$$

$$\frac{\partial \hat{u}_1^{n+1}}{\partial x_3} = \frac{\partial \hat{u}_2^{n+1}}{\partial x_3} = 0 \qquad x_3 = -1. \tag{2.5.27}$$

Using the continuity equation, Eq.(2.5.22), with $k_1 = k_2 = 0$ and the condition $\hat{u}_3^{n+1}(\pm 1) = 0$ one can show that $\hat{u}_3^{n+1} = 0$. To calculate $\hat{p}^{n+1}$ it is necessary to recall the transformed momentum equation, Eq.(2.1.2), in the x_3 direction for $k^2 = 0$ and $\hat{u}_3^{n+1} = 0$: we have $\hat{p}^{n+1} = -(\widehat{u_3^{n+1}u_3^{n+1}})$.

Energy equation

Once the velocity field is given the thermal field can be computed solving Eq. (2.1.3). The convective term S_T is advanced in the time integration by the second order explicit Adams-Bashfort scheme, while the implicit Crank-Nicolson method is used to advance the diffusion term. The time differenced energy equation (Eq.3.3.3) is therefore given by:

$$\frac{\hat{\theta}_i^{n+1} - \hat{\theta}_i^n}{\Delta\theta} = \frac{3}{2}\hat{S}_\theta^n - \frac{1}{2}\hat{S}_\theta^{n-1} + \frac{1}{PrRe_\tau}\frac{\partial^2}{\partial x_j \partial x_j}\left(\frac{\theta_i^{n+1} + \theta_i^n}{2}\right) \tag{2.5.28}$$

All n and $n-1$ terms are grouped into the historical term

$$\hat{H}_\theta = \left[\gamma_\theta \frac{\partial^2}{\partial z^2} + \left(1 - \gamma_\theta k^2\right)\right]\hat{\theta}^n + \Delta\theta\left(\frac{3}{2}\hat{S}_\theta^n - \frac{1}{2}\hat{S}_\theta^{n-1}\right), \tag{2.5.29}$$

where $k^2 = k_1^2 + k_2^2$, $\gamma_\theta = \frac{\Delta t}{2Pr \cdot Re_\tau}$. Upon rearrangement the following differential equation for the temperature field can be obtained:

$$\left(\frac{\partial^2}{\partial z^2} - \frac{1 + \gamma_\theta^2}{\gamma_\theta} \right) \hat{\theta} = -\frac{\hat{H}_\theta}{\gamma_\theta}, \tag{2.5.30}$$

as an unknown for each Fourier wave number pair (k_1, k_2). Eq.(2.5.30) can be solved with a Chebishev-Tau method to obtain the new temperature field.

2.6 Lagrangian Particle Tracking

The dynamics of the floaters is described by a set of ordinary differential equations for the position, x_p, and the velocity, v_p, of the floaters. In vector form:

$$\frac{d\mathbf{x}_p}{dt} = \mathbf{v}_p \ , \tag{2.6.1}$$

$$\frac{d\mathbf{v}_p}{dt} = \frac{(\rho_p - \rho)}{\rho_p}\mathbf{g} + \frac{(\mathbf{u}_{@p} - \mathbf{v}_p)}{\tau_p}(1 + 0.15\, Re_p^{0.687}) \ , \tag{2.6.2}$$

where $\mathbf{u}_{@p}$ is the fluid velocity at the position of the floater, interpolated with 6th-order Lagrange polynomials, whereas $\tau_p = \rho_p d_p^2/18\rho\nu$ is the relaxation time of the floater based on the density ρ_p and the diameter d_p of the floater. The Stokes drag coefficient is computed using a standard non-linear correction when the Reynolds number of the floater $Re_p = |\mathbf{u}_{@p} - \mathbf{v}_p|\, d_p/\nu > 0.2$. For thermally-stratified flows, the fluid density ρ in the equation of particle motion Eq.2.6.2 depends on the temperature. However, the variation of ρ with temperature is smaller compared with the difference between the particle density and the fluid reference density. This suggests that the variation of the fluid density in Eq.(2.6.2) is negligible, and ρ can be considered constant. Note also that, for the present choice of the physical parameters, the dynamics of the particles is not influenced by the lift force (Giusti et al., 2005; Molin et al., 2012). Floaters are treated as pointwise non-rotating rigid spheres (point-particle approach) and are injected into the flow at a concentration low enough to consider dilute system conditions: the effect of the floaters on turbulence is neglected (one-way coupling approach) as well as the inter-floaters collisions. Periodic boundary conditions are imposed on the floaters moving outside the computational domain in the homogeneous directions. In the wall-normal

direction, the floaters reaching the free surface still obey the buoyancy force balance, whereas elastic rebound is enforced at the bottom wall. A 4th-order Runge-Kutta scheme is used to advance Eqs.(2.6.1)-(2.6.2) in time.

II

Results

3

Free-surface turbulent flow

In this chapter the turbulence of free-surface is investigated.
This chapter is divided in two main sections: the first part the case of flow without thermal stratification will be studied. In this section, once the velocity profiles and statistics are shown and discussed, how energy flows across the scales at the surface will be examined . The phenomenon of energy transfer will be introduced and analysed by means of spectral energy flux. The effect of surface compressibility will be also introduced and discussed and it will be compared with the theoretical predictions. In the second part will be discussed the case of turbulence affected by thermal stratification.

3.1 Introduction: problem definition

Accurate prediction of transfer fluxes of heat, momentum and chemical species at the ocean-atmosphere interface is of paramount importance for sizing environmental issues and for depicting future climate change scenarios. For non breaking interfaces, transfer fluxes are strictly controlled by the dynamics of free-surface turbulence. Albeit constrained onto a two-dimensional space, free surface turbulence exhibits features which are barely described by simplified two-dimensional modelling. Via Direct Numerical Simulation of the fully three dimensional free surface channel flow it will be demonstrated that energy transfer near the surface is characterized by an inverse cascade from the smaller to the larger flow scales. The two-dimensional surface divergence (∇_{2D}) and compressibility (C) are used to show that regions of direct and inverse energy cascade are associated to the local flow structures. It will be demonstrated and quantified that surface compress-

ibility is a direct measure of the transition from a fully three-dimensional turbulence to a surface turbulence indicating the predominance of the inverse energy cascade and suggesting guidelines for large scale modelling of free-surface turbulent flows.

3.2 Turbulence at the free-surface

A sketch of the simulated flow configuration is shown in 3.1, together with the boundary conditions for the fluid (water). The flow field is calculated by integrating incompressible continuity and Navier-Stokes equations. The equation for the flow in dimensionless form are here recalled:

$$\frac{\partial u_i}{\partial x_i} = 0 \ , \quad \frac{\partial u_i}{\partial t} = -u_j \frac{\partial u_i}{\partial x_j} + \frac{1}{Re_\tau} \frac{\partial^2 u_i}{\partial x_j \partial x_j} - \frac{\partial p}{\partial x_i} + \delta_{1,i} \tag{3.2.1}$$

with u_i the i^{th} component of the fluid velocity, p the fluctuating kinematic pressure, $\delta_{1,i}$ the mean pressure gradient driving the flow, and $Re_\tau = hu_\tau/\nu$ the shear Reynolds number based on the channel depth h and the shear velocity $u_\tau = \sqrt{h|\ \delta_{1,i}|\ /\rho}$.
Results presented in this section are relative to two values of the shear Reynolds number: $Re_\tau^L = 171$ and $Re_\tau^H = 509$ corresponding, respectively, to shear velocity $u_\tau^L = 0.00605\ ms^{-1}$ and $u_\tau^H = 0.018\ ms^{-1}$. The size of the computational domain in wall units is $L_x^+ \times L_y^+ \times L_z^+ = 2\pi Re_\tau \times \pi Re_\tau \times Re_\tau$, discretized with $128 \times 128 \times 129$ grid points ($k_x = i2\pi/L_x$, $k_y = j2\pi/L_y$ with $i, j = 1, ..., 128$, and $T_n(z) = \cos[n \cdot \cos^{-1}(z/h)]$ with $n = 1, ..., 129$ before de-aliasing) at Re_τ^L and with $256 \times 256 \times 257$ grid points ($i, j = 256$ and $n = 257$ before de-aliasing) at Re_τ^H.

3.2.1 Flow field statistics

For validation purposes, Fig. 3.2 shows the mean and RMS (Root Mean Square) fluid velocity profiles for both Reynolds numbers: results compare well with those reported in previous studies (see e.g. [46], not shown). Figs. 3.2(a) and 3.2(c) indicate that the free surface does not alter significantly the mean velocity profile, but also does not influence near-wall turbulence. The strong effect of the free surface on turbulence is revealed by the increase of the streamwise and spanwise components of the RMS near the surface

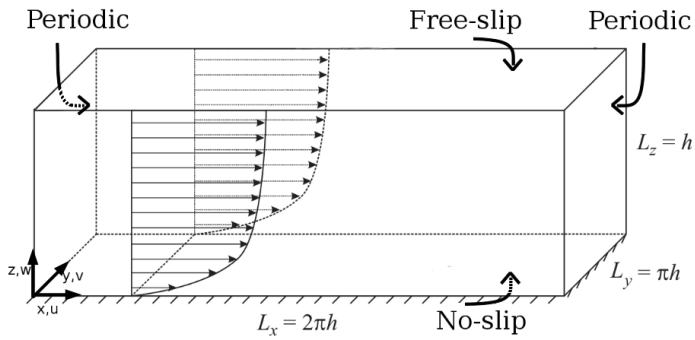

FIGURE 3.1 – Sketch of the computational domain with boundary conditions for the fluid.

itself (see Figs. 3.2(b) and 3.2(d)), indicating the presence of an anisotropic velocity layer [46].

3.2.2 Characterization of free-surface turbulence through energy spectra

Turbulent flow structures near the free surface of an open channel have been investigated in several previous studies [32, 48, 33, 54, 62, 46, 47], as discussed in Chap. 1. All these studies show that surface structures are generated and sustained by bursting phenomena that are continuously produced by wall shear turbulence inside the buffer layer. Bursts emanate from the bottom of the channel and produce upwelling motions of fluid as they are convected toward the free surface. Near the surface, turbulence is restructured and nearly two-dimensionalized due to damping of vertical fluctuations [61]: upwellings appear as two-dimensional sources for the surface-parallel fluid velocity and alternate to sinks associated with downdrafts of fluid from the surface to the bulk. Through sources fluid elements at the surface are replaced with fluid from the bulk, giving rise to the well-known surface-renewal events [33]. Whirlpool-like vortices may also form in the high-shear region between closely-adjacent upwellings. This phenomenology has been long recognized to produce flow with properties that differ from those typical of two-dimensional incompressible Navier-Stokes turbulence [35, 23]. These properties can be quantified examining the energy spectra of the fluid velocity fluctuations on the surface [46], shown in Fig. 3.3 for the case of statistically-steady turbulence. To emphasize direction-related as-

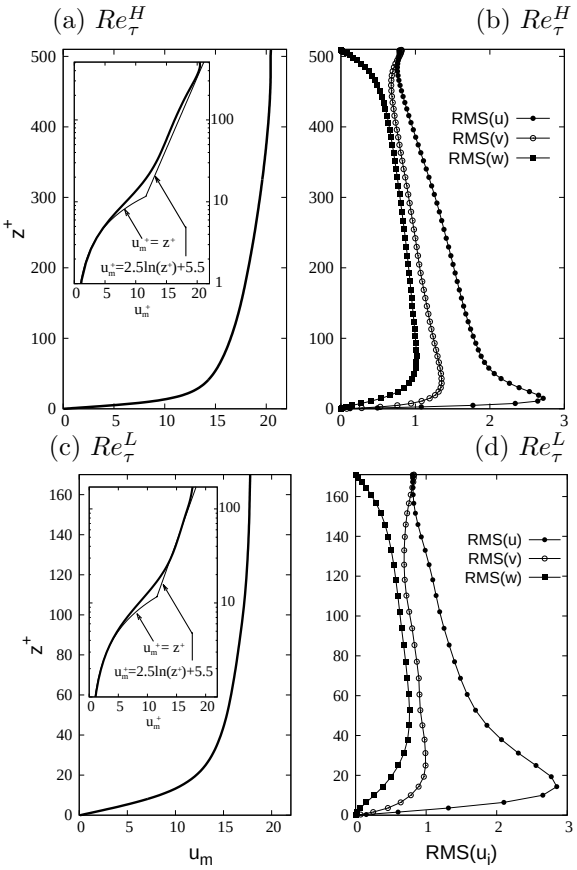

FIGURE 3.2 – Fluid velocity statistics: mean streamwise velocity, u_m^+ (panels (a) and (c)); and Root Mean Square components, $RMS(u_i)$ (panels (b) and (d)). Panels (a-b) refer to the Re_τ^H simulation, panels (c-d) refer to the Re_τ^L simulation. The insets in panels (a) and (b) compare the mean velocity profile to the wall law $u_m^+ = z^+$ and to the logarithmic law $u_m^+ = 2.5\ln(z^+) + 5.5$ in lin-log scale.

pects of the energy spectra, results for the surface-parallel velocities are examined in isolation: Panels (a) and (c) in Fig. 3.3 show the one-dimensional streamwise spectra of the streamwise velocity $E_x(k_x)$ computed at the free surface ($z^+ = 0$, circles) and at the channel center ($z^+ = 254.6$ at Re_τ^H, $z^+ = 85.5$ at Re_τ^L, squares) in the Re_τ^H and Re_τ^L simulations, respectively; panels (b) and (d) show the spectra of the spanwise velocity $E_y(k_x)$ in the same two regions. Solid lines represent the slope of the spectrum within the inertial regimes predicted by the Kraichnan-Leith-Batchelor (KLB) phenomenology of two-dimensional turbulence [34, 4]: $k_x^{-5/3}$, representing inverse cascade of energy to large flow scales and k_x^{-3}, representing direct

cascade of enstrophy to small flow scales. A collective analysis of spectra shown in Fig. 3.3 reveals clear deviations from two-dimensionality. First, no evident $-5/3$ range is observed except for few of the lowest wavenumbers: this can be attributed to the intermittent nature of turbulence associated with spatial fluctuations in the rate of energy dissipation. A relatively larger range of high wavenumbers can be identified over which spectra exhibit a -3 scaling: In the present flow configuration, however, this corresponds to up-cascading of energy from large to small wavenumbers, namely to merging of smaller flow structures into larger structures. Such findings cannot be reconciled with the KLB theory for 2D turbulence.

Examining $E_x(k_x)$, we notice that the spectrum at the free surface is always below that in the center of the channel. Also, energy in the high-wavenumber portion of the spectrum decays more rapidly [46], roughly as k^{-6}: This tendency is particularly evident at Re_τ^H and indicates that only large-scale surface structures survive to the detriment of small-scale ones. Examining $E_y(k_x)$, we observe that redistribution of energy from small to large scales in proximity of the free surface determines a cross-over between spectra at low wavenumbers (for both Reynolds numbers): this finding confirms further that small scale structures play little role in determining turbulence properties in this region of the flow.

3.2.3 How energy flows across the scales and compressibility effects at free surface

To investigate further on the direct/inverse cascade of the energy flux across turbulent scales a filtering approach similar to that presented in [48, 73] is used. A filtered flowfield $\overline{u}^{(\Delta)}$ is obtained applying a low-pass Gaussian filter $G_l(\mathbf{k}) = exp(-|\mathbf{k}|^2\Delta^2/24)$, in which Δ is the filter size, to the field variables written in the wavenumber space ($\mathbf{k}$). The scales of the velocity field are thus divided into scales larger than Δ (unfiltered) and scales smaller than Δ (filtered). Turbulence kinetic energy transport equation for the scales larger than a given Δ ($\overline{q} = \overline{u_i}^{(\Delta)}\overline{u_i}^{(\Delta)}$) is thus [48, 73] :

$$\begin{aligned}\frac{\partial \overline{q}}{\partial t} + \frac{\partial \overline{q u_i}^{(\Delta)}}{\partial x_j} = \frac{\partial}{\partial u_j}\left(-2\overline{p}^{(\Delta)}\overline{u_j}^{(\Delta)} - 2\overline{u_i}^{(\Delta)}\tau_{ij} + \frac{1}{Re}\frac{\partial \overline{q}}{\partial x_j}\right) \\ - \frac{2}{Re}\frac{\partial \overline{u_i}^{(\Delta)}}{\partial x_j}\frac{\partial \overline{u_i}^{(\Delta)}}{\partial x_j} + 2\tau_{ij}\overline{S_{ij}}^{(\Delta)},\end{aligned} \tag{3.2.2}$$

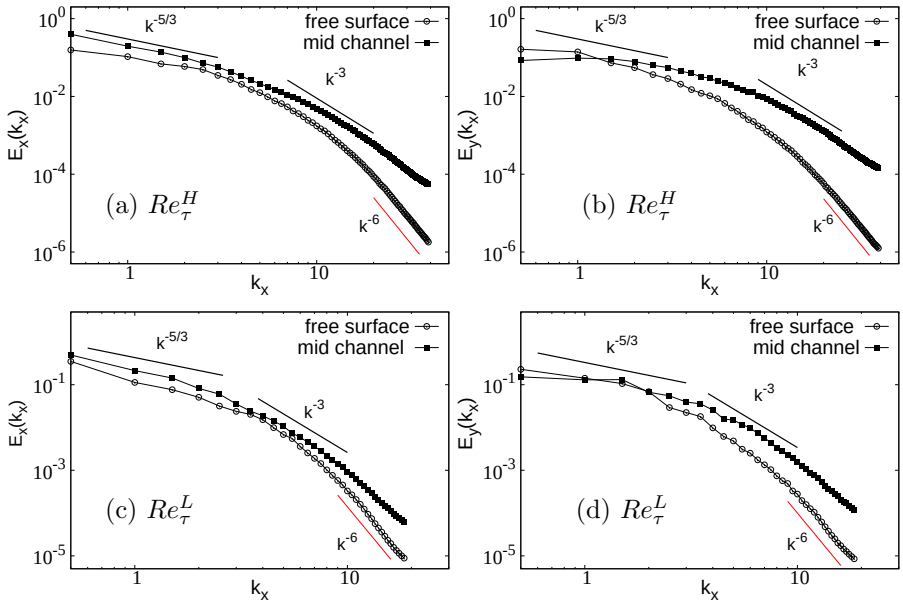

FIGURE 3.3 – One-dimensional (streamwise) energy spectra of the streamwise ($E_x(k_x)$, panels (a) and (c)) and spanwise ($E_y(k_x)$, panels (b) and (d)) surface-parallel velocity fluctuations. Spectra are computed at the free surface ($z^+ = 0$, circles) and at the channel center ($z^+ = 254.6$ at Re_τ^H, $z^+ = 85.5$ at Re_τ^L, squares). Panels (a) and (b) refer to the Re_τ^H simulation, panels (c) and (d) refer to the Re_τ^L simulation.

where $\tau_{ij} = \overline{u_i u_j}^{(\Delta)} - \overline{u_i}^{(\Delta)}\overline{u_j}^{(\Delta)}$ is the stress and $\overline{S_{ij}}^{(\Delta)} = 1/2(\partial\overline{u_i}^{(\Delta)}/\partial x_j)$ is the rate-of-strain tensor. The dissipation for the scales smaller than Δ is

$$\Pi^{(\Delta)} = -\tau_{ij}\overline{S_{ij}}^{(\Delta)} = -\left[\overline{u_i u_j}^{(\Delta)} - \overline{u_i}^{(\Delta)}\overline{u_j}^{(\Delta)}\right]\frac{\partial\overline{u_i}^{(\Delta)}}{\partial x_j}.$$

This quantity is the energy flux between small and large scales across the filter size. In particular, $\Pi^{(\Delta)} > 0$ indicates the direct energy cascade from larger to smaller scales, whereas $\Pi^{(\Delta)} < 0$ is the inverse energy cascade from smaller to larger scales. We can explicitely compute the contribution of the direct and inverse energy flux to the total energy flux as $\Pi_+^{(\Delta)} = \frac{1}{2}(\Pi^{(\Delta)} + |\Pi^{(\Delta)}|)$ and $\Pi_-^{(\Delta)} = \frac{1}{2}(\Pi^{(\Delta)} - |\Pi^{(\Delta)}|)$, respectively. Note that $\Pi^{(\Delta)}$, $\Pi_+^{(\Delta)}$ and $\Pi_-^{(\Delta)}$ are function of the cut-off filter size Δ: by varying the filter size Δ, we obtain the characteristic energy flux at different scales.

The behavior of time and plane averaged energy fluxes for both Reynolds numbers is demonstrated in Fig. 3.4.

Results, which are relative to the channel surface, are shown as a func-

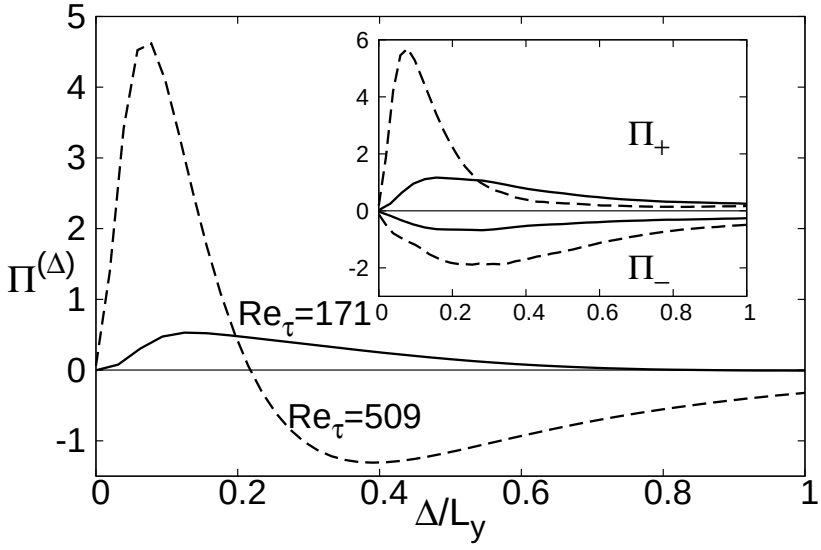

FIGURE 3.4 – Time-average of the energy flux $\Pi^{(\Delta)}$ as a function of the Gaussian filter size (Δ) at the channel surface ($z = 0$) for Re_τ^L (solid line, $-$) and Re_τ^H (dashed line, $--$). The contribution of the positive energy flux (direct cascade, $\Pi_+^{(\Delta)}$) and of the negative energy flux (inverse cascade, $\Pi_-^{(\Delta)}$) are also shown in the inset.

tion of the dimensionless filter size, Δ/L_y, and are normalized by the plane averaged absolute value of the viscous dissipation $\epsilon_0 = (2/Re)S_{ij}S_{ij}$ [48].
For the low Reynolds number Re_τ^L (solid line in Fig. 3.4), we observe that the energy flux peaks at $\Delta/L_y \simeq 0.1$, and then monotonically decreases to zero when the filter size Δ increases. The energy flux is indicating the predominance of the direct energy cascade mechanism across the entire scale range. Note that in physical space the peak corresponds to the size of the most energetic surface structures like plumes, upwellings and time-persistent recirculation regions.
The behaviour of the energy flux for the high Reynolds number Re_τ^H (dashed line in Fig. 3.4) appears richer: the maximum is reached approximately at the same location $\Delta/L_y \simeq 0.1$ observed for Re_τ^L but the energy flux becomes negative for $\Delta/L_y > 0.2$. This indicates a strong and persistent inverse energy cascade occurring at larger scales.
To deepen the analysis, it is observed the behavior of the single positive ($\Pi_+^{(\Delta)}$) and negative ($\Pi_-^{(\Delta)}$) contributions to the overall energy flux in order to establish the relative importance of direct and inverse energy cascade mechanisms for all scales. As shown in the inset of Fig. 3.4, for low and high Reynolds numbers both cascades exist in the entire range of scales. However, for Re_τ^L the contribution of the inverse energy cascade is not sufficient to dominate the dynamics of turbulence: it is always $\Pi_+^{(\Delta)} > \Pi_-^{(\Delta)}$. By contrast, for Re_τ^H the inverse cascade is proportianally more important, with a peak value occurring for scales which are larger ($\Delta/L_y \simeq 0.25$) than those corresponding to the peak of the direct cascade ($\Delta/L_y \simeq 0.1$). Overall, it is observed a competion between the direct and the inverse cascade mechanism which produces a non-monotonic behavior. For $\Delta/L_y < 0.2$, $\Pi_+^{(\Delta)}$ prevails yelding to the direct energy cascade. For $\Delta/L_y > 0.2$, $\Pi_-^{(\Delta)}$ dominates, producing a remarkable inverse energy cascade. This inverse energy cascade controls the dynamics of the large and persistent (in time and space, see [61]) scales, with important implications for all transport phenomena for which these scales are significant.

3.2.4 Flow topology & Energy Cascade

The physical mechanism leading to direct or inverse energy cascades is still an open question, with new promising theories (for two dimensional turbulence) supporting the importance of large scale strain and vortex thinning in the dynamics of the inverse energy cascade [73]. At the surface of our three

dimensional numerical experiment, turbulence is continuously regenerated by upwellings advecting energy at the surface, where turbulence dynamics appears somehow two-dimensionalized and characterized by strongly different features [61]. To explore surface turbulence it is studied the behavior of the two dimensional surface divergence $\nabla_{2D} = \frac{\partial u}{\partial x} + \frac{\partial v}{\partial y}$. This topological flow feature provides information about the exchange of mass and momentum between the surface and the bulk of the flow. Regions characterized by $\nabla_{2D} > 0$ are regions of local flow expansion, generated by bulk flow upwellings. Regions characterized by $\nabla_{2D} < 0$ are regions of local flow compression leading to downwellings. Contour maps of the instantaneous energy flux $\Pi^{(\Delta)}$ (computed for $\Delta/L_y = 0.2$, a scale at which inverse and direct cascades are both significant for the two Re_τ examined) and of the instantaneous two dimensional surface divergence ∇_{2D} are shown vis-a-vis for low and high Reynolds numbers in Fig. 3.5 and Fig. 3.6 respectively. Local energy fluxes and flow sources/sinks have a distinctly inhomogeneous pattern distribution exhibiting a remarkably strong correspondence, which can give a possible explanation of surface turbulence mechanisms.

Regions of direct cascade ($\Pi^{(\Delta)} > 0$) seem to correspond to regions of flow expansion (upwellings, $\nabla_{2D} > 0$), whereas regions of inverse cascade ($\Pi^{(\Delta)} < 0$) seem to correspond to regions of flow compression (downwellings, $\nabla_{2D} < 0$). We can try to measure this correspondence via the following spatial correlations computed for the same filter size $\Delta/L_y = 0.2$:

$$\langle \nabla^+_{2D} \Pi^{(\Delta)}_+ \rangle = \frac{\langle \nabla^+_{2D}(x - x', y, z_{surf}) \Pi^{(\Delta)}_+(x, y, z_{surf}) \rangle}{\nabla^+_{2D,rms}(z_{surf}) \Pi^{(\Delta)}_{+,rms}(z_{surf})}$$

and

$$\langle \nabla^-_{2D} \Pi^{(\Delta)}_- \rangle = \frac{\langle \nabla^-_{2D}(x - x', y, z_{surf}) \Pi^{(\Delta)}_-(x, y, z_{surf}) \rangle}{\nabla^-_{2D,rms}(z_{surf}) \Pi^{(\Delta)}_{-,rms}(z_{surf})},$$

where z_{surf} represents the position of the free surface. Results are shown in Fig. 3.7 for $Re_\tau = 171$ and in Fig. 3.8 for $Re_\tau = 509$.

The correlation between $\Pi^{(\Delta)}_+$ and ∇^+_{2D} and between $\Pi^{(\Delta)}_-$ and ∇^-_{2D}, is strong for both Re^L_τ and Re^H_τ for a length roughly corresponding to the filter width and then drops to almost zero for scales larger than the filter size. This strong spatial correlation suggests a causal relation between the direct/inverse energy cascade and the surface renewal mechanism based

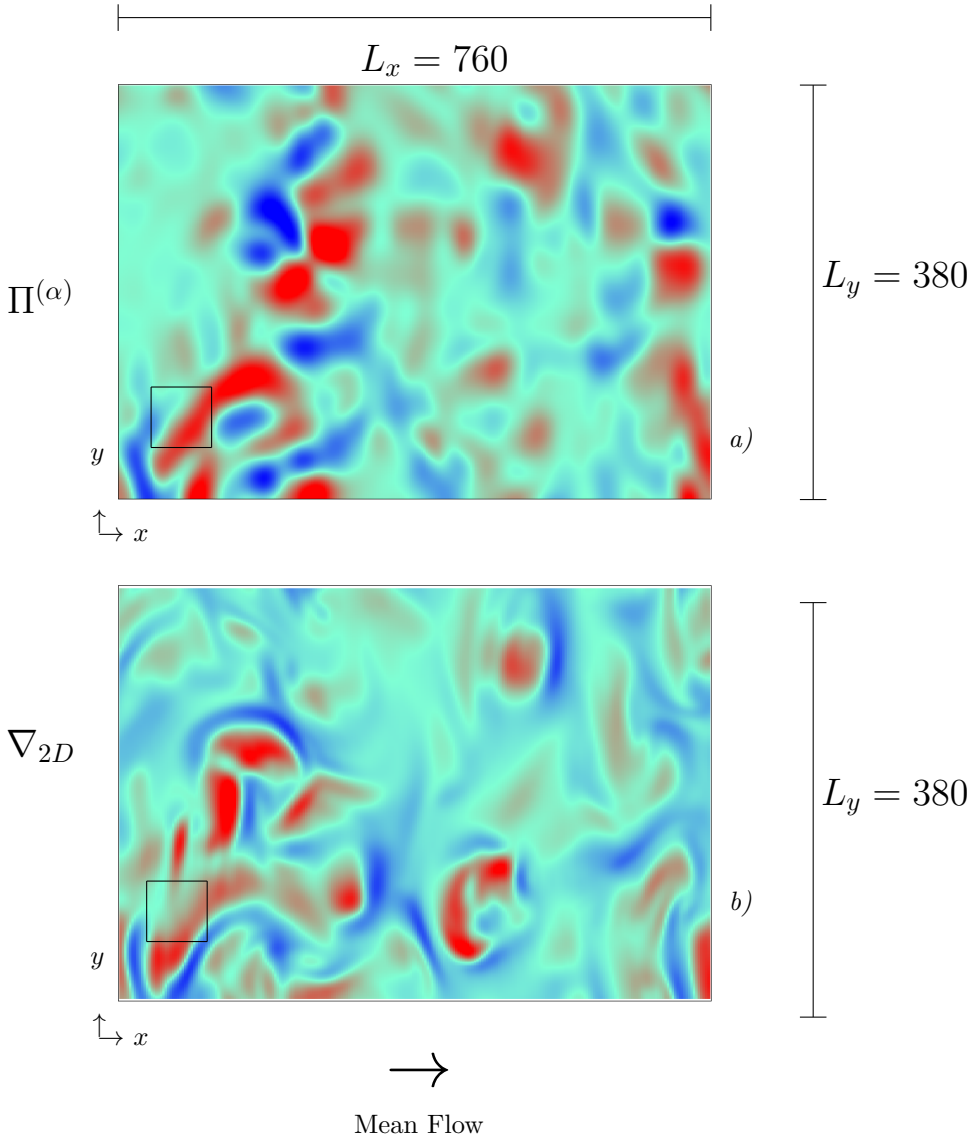

FIGURE 3.5 – Contour maps of the energy flux $\Pi^{(\Delta)}$ (panel a) and of the two-dimensional surface divergence ∇_{2D} (panel b) computed at the free surface for $Re_\tau = 171$.

on upwellings and downwellings [61, 48]. To show this striking correspondence, in Figs. 3.7b-c and in Figs. 3.8b-c we present a zoom of the small squares area depicted in Figs. 3.5-3.6. Contour maps of Figs. 3.7b-c show an almost perfect coincidence of direct/inverse energy cascade regions with

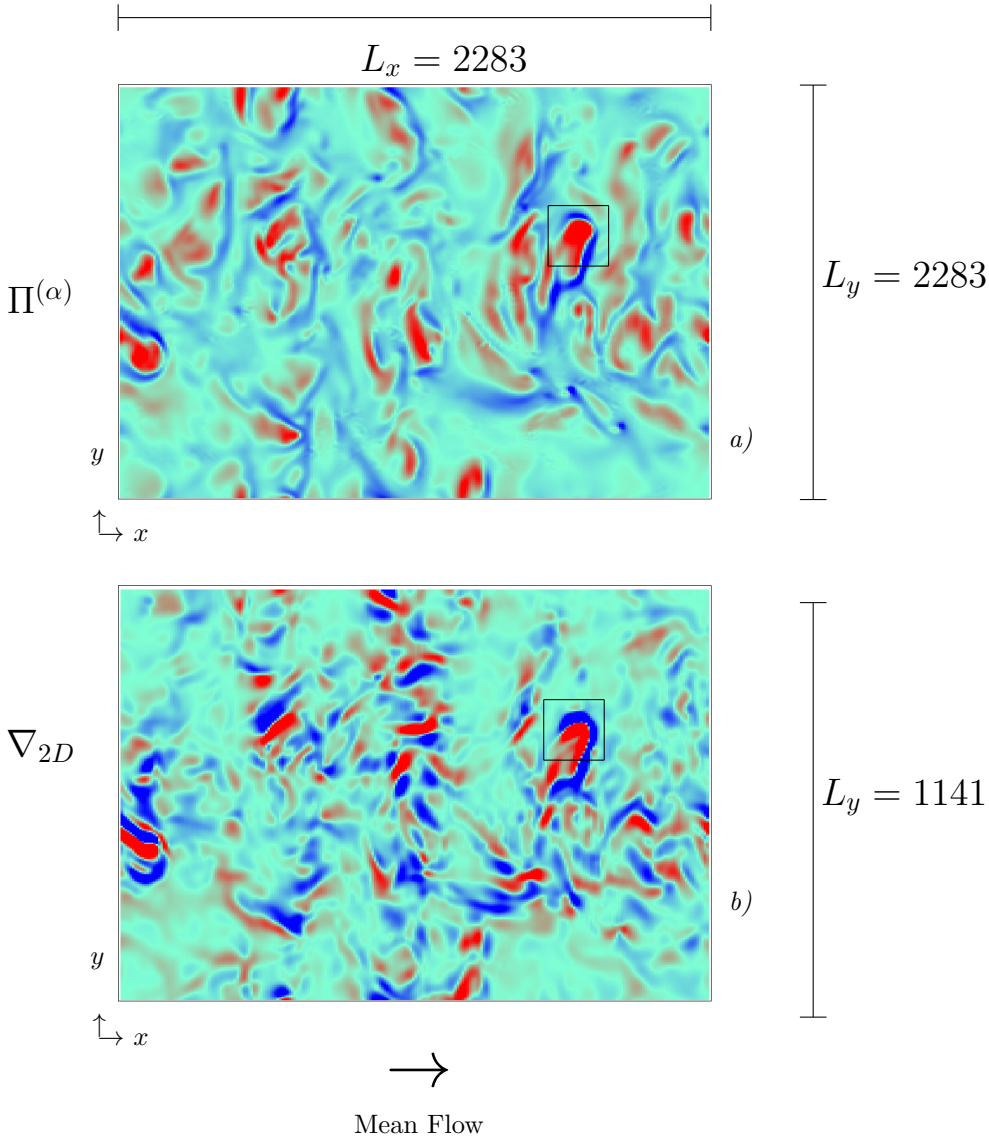

FIGURE 3.6 – Contour maps of the energy flux $\Pi^{(\Delta)}$ (panel a) and of the two-dimensional surface divergence ∇_{2D} (panel b) computed at the free surface for $Re_\tau = 509$.

the expansion/compression regions: the overlapping streamlines complete the self evidence of the flow topology with the surface regeneration mechanism. The same correlations are even better depicted in Figs. 3.8b-c. The occurence of downscale/upscale energy transfer can be directly linked

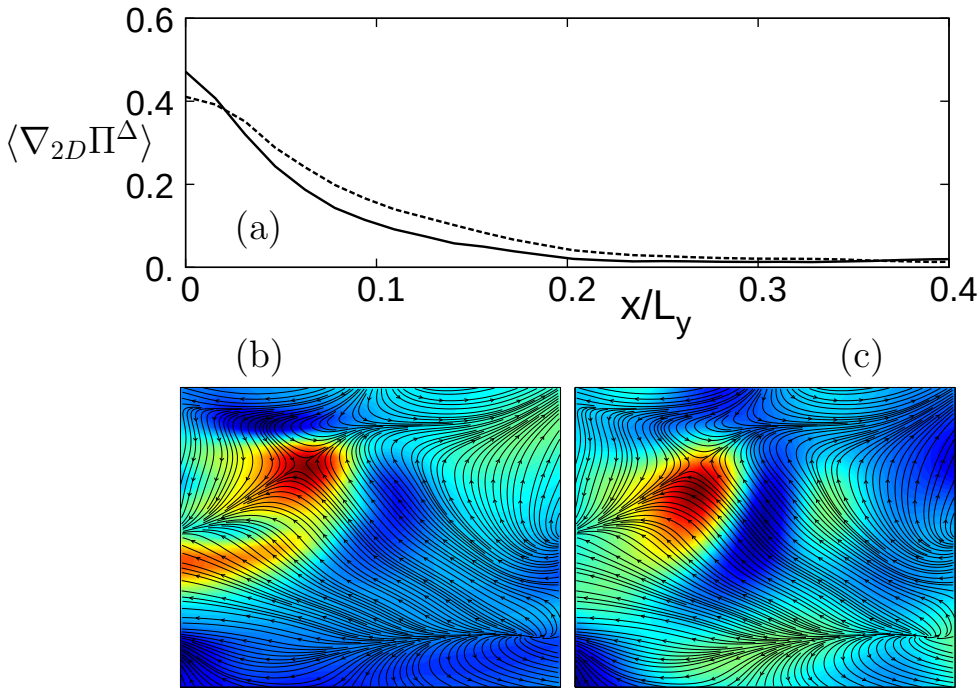

FIGURE 3.7 – Correlation coefficient $\langle \nabla^{+}_{2D} \Pi^{\Delta}_{+} \rangle$ (solid line, $-$) and $\langle \nabla^{-}_{2D} \Pi^{\Delta}_{-} \rangle$ (dashed line, $--$) between the positive (resp. negative) energy flux Π^{Δ}_{+} (resp. Π^{Δ}_{-}) and the positive (resp. negative) two dimensional surface divergence ∇^{+}_{2D} (resp. ∇^{-}_{2D}) computed along the streamwise direction x and averaged in time for $Re^{L}_{\tau} = 171$ (panel a). We also show the spatial distribution of $\Pi^{(\Delta)}$ (panel b) and ∇_{2D} (panel c) on the rectangular region indicated in Fig. 3.5. Flow streamlines have been superposed to each contour map to highlight regions of local flow expansion (flow sources) and regions of local flow compression (flow sinks).

to the behavior of the third order structure function, $S_3 = \langle (\delta_r u)^3 \rangle$, with $\delta_r u = [u(x+r) - u(x)]$ being the longitudinal velocity increments. In particular, the sign of S_3 indicates the direction of the energy flux: for negative S_3, energy goes from large to small scales (downscale energy transfer), whereas for positive S_3 energy goes from small to large scales (upscale energy transfer). Our results on the behavior of S_3 at the channel center and at the free surface are shown (as a function of r/L_y) in Fig. 3.9 for both Re^{L}_{τ} and Re^{H}_{τ}.

At the channel center (Fig. 3.9a), S_3 is always negative for both Re_{τ},

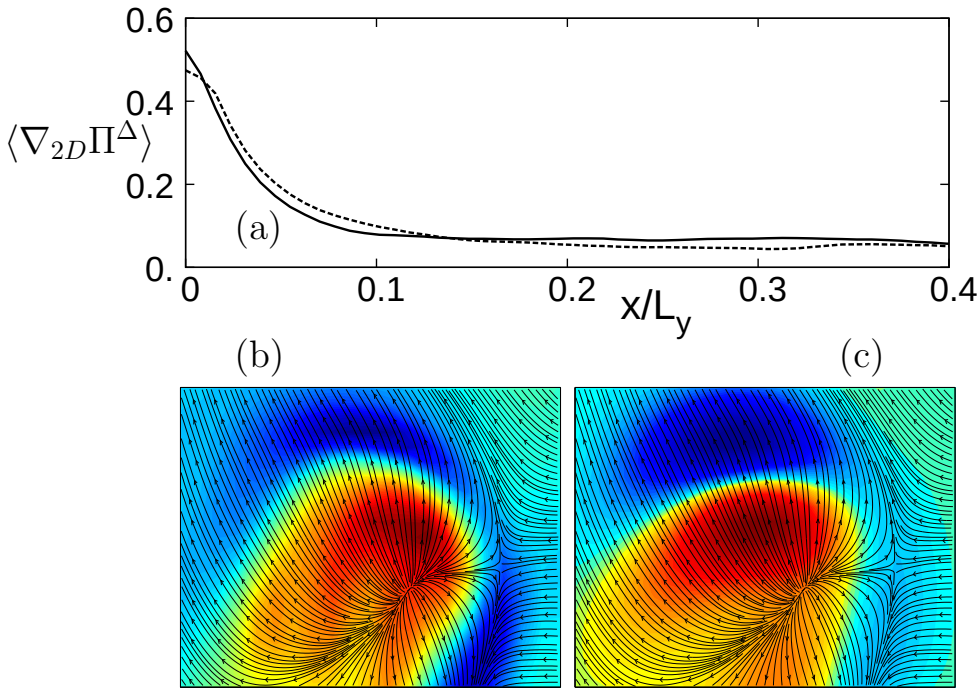

FIGURE 3.8 – Correlation coefficient $\langle \nabla^{+}_{2D} \Pi^{\Delta}_{+} \rangle$ (solid line, $-$) and $\langle \nabla^{-}_{2D} \Pi^{\Delta}_{-} \rangle$ (dashed line, $--$) between the positive (resp. negative) energy flux Π^{Δ}_{+} (resp. Π^{Δ}_{-}) and the positive (resp. negative) two dimensional surface divergence ∇^{+}_{2D} (resp. ∇^{-}_{2D}) computed along the streamwise direction x and averaged in time for $Re^{L}_{\tau} = 509$ (panel a). We also show the spatial distribution of Π (panel b) and ∇_{2D} (panel c) on the rectangular region indicated in Fig. 3.6. Flow streamlines have been superposed to each contour map to highlight regions of local flow expansion (flow sources) and regions of local flow compression (flow sinks).

indicating the predominance of the downscale energy transfer: in the bulk, energy flows from large to small scales only. A similar behavior is observed at the free surface for Re^{L}_{τ} (Fig. 3.9b, triangles), with only a narrow range of scales (around $r/L_y \simeq 0.1$) were S_3 is positive (i.e. a limited upscale energy transfer). The situation changes for Re^{H}_{τ} at the free surface (Fig. 3.9b, circles): S_3 is negative at small length scales but turns positive (displaying a plateau) for $r/L_y > 0.1$. This indicates the occurrence of a downscale energy transfer for $r/L_y < 0.1$, which is replaced by a persistent upscale energy transfer for $r/L_y > 0.1$. The length scale at which S_3 changes sign

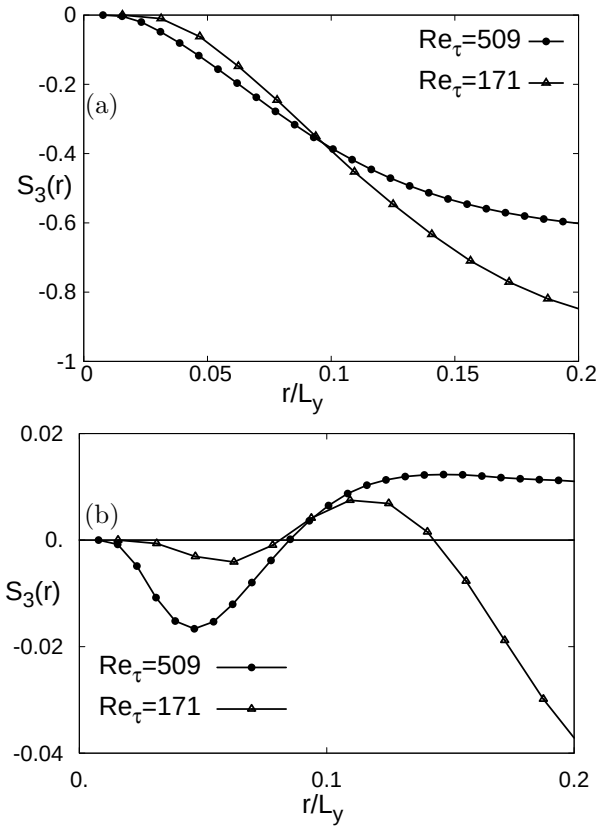

FIGURE 3.9 – Third order structure function $S_3(r)$ computed at the channel center (panel a) and at the free surface (panel b) for both $Re_\tau^L = 171$ and $Re_\tau^H = 509$. S_3 is shown as a function of r/L_y .

$(r/L_y \simeq 0.1)$ can be regarded as the average size of an upwelling. This may be understood from a simple physical interpretation of the third order structure function. By drawing an imaginary circle around a given flow field, the radial vector of the velocity difference between the center of the circle and its circumference indicates the energy direction: the energy flows out of the circle, if the circle encloses an upwelling, whereas the energy flows in, if the circle encloses a downwelling. The upscale energy transfer has

been recently associated ([7]) also to the behavior of the second-order $S_2 = \langle(\delta_r u)^2\rangle$ and forth-order $S_4 = \langle(\delta_r u)^4\rangle$ structure functions. In particular, structure functions were found to scale as $S_p \simeq r_p/3$ in the inertial range. Here, we try to quantify the behavior of $S_2(r)$ and $S_4(r)$ in free surface flows, where no clear indication of these behaviors is available [29].

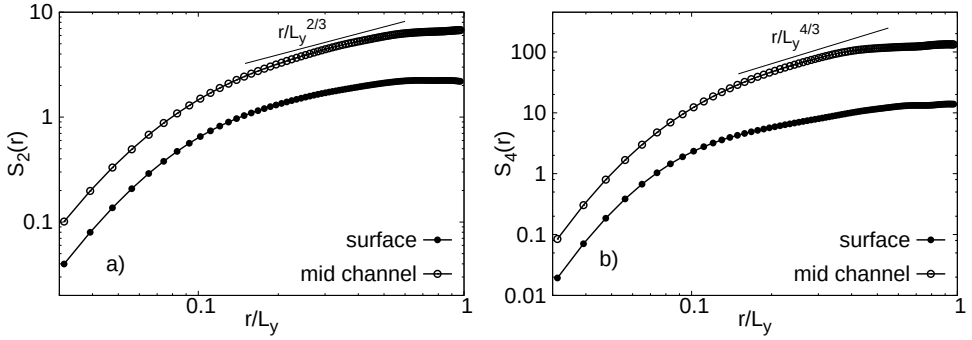

FIGURE 3.10 – Second ($S_2(r)$, panel a) and forth ($S_4(r)$, panel b) order structure functions for $Re_\tau^L = 171$ expressed as a function of r/L_y and computed at the surface and at the center of the channel. The solid lines indicate the observed scaling in the inertial range. At the channel center (mid channel, empty circles), $S_2 \simeq r^{2/3}$ and $S_4 \simeq r^{4/3}$

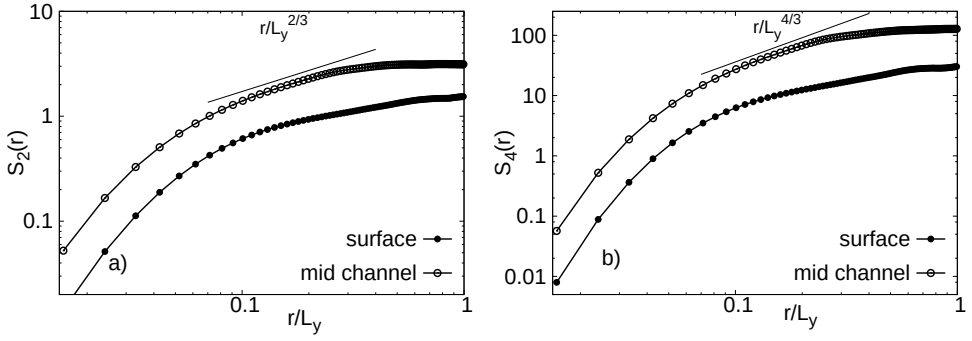

FIGURE 3.11 – Second ($S_2(r)$, panel a) and forth ($S_4(r)$, panel b) order structure functions for $Re_\tau^H = 509$ expressed as a function of r/L_y and computed at the surface and at the center of the channel. The solid lines indicate the observed scaling in the inertial range. At the channel center (mid channel, empty circles), $S_2 \simeq r^{2/3}$ and $S_4 \simeq r^{4/3}$

Our results are shown in Figs. 3.10-3.11 as a function of the dimensionless displacement r/L_y and for both Re_τ^L and Re_τ^H .

Specifically, we compare the behavior of the structure functions at the free surface (filled circles) and at the channel center (empty circles) .

The range of scales where we observe an algebraic scaling, although not extremely large, is however sufficient to propose a trend behavior. As expected, where turbulence is three dimensional (channel center) $S_p \simeq r_p/3$ for both Re_τ^L and Re_τ^H.

To quantify carefully the scaling behavior of the structure functions at the free surface, we use the Extended Self Similarity (ESS) representation [6].

The slope (ξ_p) of the p-th order structure function ($S_p \simeq r^{\xi_p}$) is obtained by plotting $\langle(\delta_r u)^p\rangle$ versus $\langle(\delta_r u)^3\rangle$ on a log-log plot, and by computing $\xi_p = \mathrm{d}logS_p/\mathrm{d}logS_3$. The value of ξ_p measured for $p \leq 6$ is shown in Fig. 3.12 and compared with the Kolmogorov p/3 scaling (dotted line). Deviations from the Kolmogorov scaling are seen for $p \geq 4$ for both Re_τ^L and Re_τ^H (with larger deviations for Re_τ^H), and are likely due to intermittency phenomena occurring at the free surface.

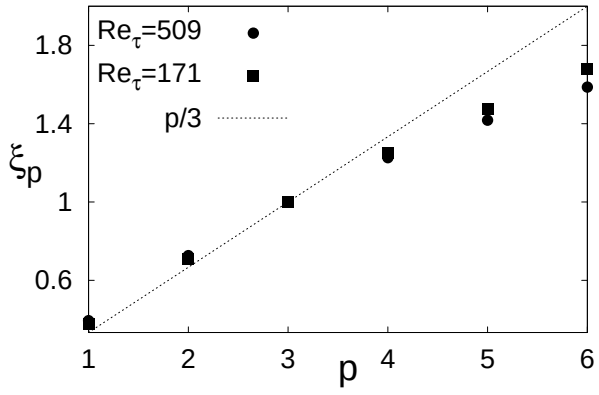

FIGURE 3.12 – Structure function scaling exponent ξ_p at the free surface for both Re_τ^L and Re_τ^H . The dotted line indicates the classical Kolmogorov scaling p/3.

3.2.5 Flow compressibility

These results lead to infer the following scenario for the dynamics of direct/inverse energy cascades in free surface turbulence. Direct energy cascade is associated with regions of local flow expansion ($\nabla_{2D} > 0$) caused

by upwellings reaching the free surface from below. Since upwellings are produced by the full three dimensional flow field, they follow the basic laws of three dimensional turbulence: this behavior is kept also in the initial stage of their joining the surface. This sort of fossil three dimensional turbulence explains the regions of direct energy cascade observed at the free surface. Once attached at the free surface, upwellings gradually loose their three dimensionality and move according to the basic laws of two dimensional turbulence (hence following the inverse energy cascade). The relative strength of the inverse energy cascade mechanism is small for low Re_τ but increases for increasing Re_τ. At higher Re_τ, the free surface dynamics is decoupled from the three dimensional dynamics of the bulk, hence becoming closer to the classical two-dimensional turbulence.

However, surface models based on two dimensional turbulence theories and simulations cannot but partially reproduce the much richer physics exhibited by surface turbulence [63]. As an example, the two dimensional divergence cannot be used as flow topology indicator in two dimensions since it is locally zero. In previous works [23, 63, 8] the flow compressibility rather than the two dimensional divergence, was used to characterize the behavior of three dimensional turbulence onto two dimensional planes. The degree of compressibility is quantified by the dimensionless compressibility factor

$$\begin{aligned} C &= \frac{\langle (\nabla \cdot \mathbf{v})^2 \rangle}{\langle |\nabla \mathbf{v}|^2 \rangle} = \\ &= \frac{\langle (\partial_x u_x + \partial_y u_y)^2 \rangle}{\langle (\partial_x u_x)^2 \rangle + \langle (\partial_x u_y)^2 \rangle + \langle (\partial_y u_x)^2 \rangle + \langle (\partial_y u_y)^2 \rangle}. \end{aligned} \tag{3.2.3}$$

The value of C as a function of the vertical direction z/h is shown in Fig. 3.13 for both Re_τ^L (Fig. 3.13a) and Re_τ^H (Fig. 3.13b). The range of abscissae in Fig. 3.13 is limited to the top half of the channel from the free surface down to the channel centerline ($z/h = 0.5$). For both Re_τ, compressibility peaks close to the surface and drops down almost asymptotically to $C = 0.16$ (dashed line in Fig. 3.13) at the channel half height, a value indicating the theoretical prediction of C for homogeneous isotropic turbulence [8].

In the present case, it is clear that the behavior of C far from the free surface approaches the limiting behavior of three dimensional homogeneous isotropic turbulence. The line $C = 0.5$ in Figure is the theoretical prediction based on the Kraichnan compressible flow as reported in [34, 8]. This

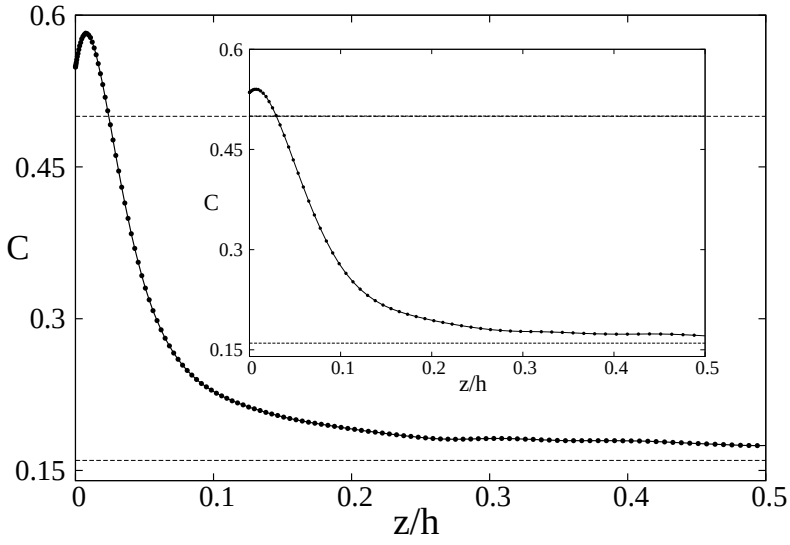

FIGURE 3.13 – Behavior of the compressibility factor C along the wall-normal direction z/h for Re_τ^H and for Re_τ^L (inset). Note that $z = 0$ represents the free surface. Values of the compressibility factor for a two dimensional cut of a three dimensional homogeneous isotropic turbulent flow ($C \simeq 1/6$) and for a compressible Kraichnan flow ($C = 0.5$) are also shown ([8]).

value represents the upper limit of the compressibility factor as computed from three dimensional simulations of homogeneous isotropic turbulence with suitable boundary conditions [63, 8]. Our data show for the first time the compressibility of a three dimensional free surface channel flow and report values for the compressibility factor C trespassing the theoretical threshold value $C = 0.5$. In accordance with previous works [28, 12] in which an increase of the compressibility factor C was associated with an inverse energy cascade prevailing over a direct energy cascade, we find that compressibility is larger for larger Re_τ (hence when a strong inverse energy cascade occurs). It is important to observe that a compressibility factor larger than the critical value $C = 0.5$ is of significant importance: it suggets the occurrence of extreme events (velocity source and sinks, associated to point-like structures) which which may have strong influence on the dispersion of chemical species and particles in free surface flows (as it will be discussed estensively in next Chap. 4).

3.3 Stratified turbulence at the surface

In this section the influence of thermal stratification on the free surface turbulent channel flow, will be investigated.

The reference geometry is the same of previous section with a stable stratification obtained by imposing a constant heat flux at the surface and an adiabatic condition at the wall (see Fig. 2.1).

The system of equations resolved are here recalled in dimensionless form: the conservation of mass, momentum and energy of the fluid is described by the following set of three-dimensional time-dependent equations:

$$\nabla \cdot \mathbf{u} = 0 \ , \tag{3.3.1}$$

$$\frac{\partial \mathbf{u}}{\partial t} + \mathbf{u} \cdot \nabla \mathbf{u} = \frac{1}{Re_\tau} \nabla^2 \mathbf{u} - \nabla p + \frac{Gr}{Re_\tau^2} \theta \boldsymbol{\delta}_g + \boldsymbol{\delta}_p, \tag{3.3.2}$$

$$\frac{\partial \theta}{\partial t} + \mathbf{u} \cdot \nabla \theta = \frac{1}{Re_\tau Pr} \nabla^2 \theta - \beta_T, \tag{3.3.3}$$

where $\mathbf{u} = (u_x, u_y, u_z)$ is the velocity vector, p is the fluctuating kinematic pressure, $\boldsymbol{\delta}_p = (1, 0, 0)$ is the mean pressure gradient that drives the flow in the streamwise direction, θ is the temperature field and $\boldsymbol{\delta}_g = (0, 0, 1)$ is necessary to compute the buoyancy term only in the wall-normal direction.

For the fluid velocity, no-slip (resp. no-stress) boundary conditions are enforced at the bottom (resp. top) boundary.

The dimensionless Reynolds, Grashof and Prandtl number are defined as

$$Re_\tau = \frac{u_\tau h}{\nu}, \qquad Gr = \frac{g \beta h^3}{\nu^2} \frac{\partial \theta}{\partial z} \Big|_s \ , \qquad Pr = \frac{\mu c_p}{\lambda} \ . \tag{3.3.4}$$

where μ and ν are the dynamic and the kinematic viscosity, β is the thermal expansion coefficient, c_p is the specific heat and λ is the thermal conductivity. In the definition of Re_τ and Gr, $u_\tau = (h \left|\boldsymbol{\delta}_p\right| / \rho)^{1/2}$ is the shear velocity (ρ being the fluid density) whereas $\partial\theta/\partial z|_s$ is the imposed free-surface heating.

An extensive campaign of Direct Numerical Simulations (DNS) is performed to investigate the role of the fluid stratification. All the simulations are run at reference Prandtl number $Pr = 5$ and Reynolds number

$Re_\tau = 171$. Three different values of the Grashof number are considered in this study: $Gr = 0$, $Gr = 3.02 \times 10^5$ and $Gr = 9.15 \times 10^5$. As a consequence, the numerical simulations are run at three different values of the shear Richardson number $Ri_\tau = Gr/Re_\tau^2$, which measures the importance of buoyancy compared to inertia: $Ri_\tau = 0$, $Ri_\tau = 165$ and $Ri_\tau = 500$. Note that Gr is changed by changing the temperature gradient at the free surface. The spatial resolution of each simulation ($128 \times 128 \times 257$) is chosen to fulfill the requirements imposed by DNS (Tiselj et al., 2001 [70]).

3.3.1 Flow field statistics

First how the stable stratification of the fluid influences the mean flow field in free-surface turbulence will be considered.

In Fig. 3.14a the mean streamwise velocity profile $\langle u_x \rangle$ (in wall units) is shown for the three regimes of stratification as a function of the wall-normal coordinate $z^+ = zu_\tau/\nu$. Brackets indicate time and space average. The averaging procedure is done using snapshots of velocity and temperature fields separated in time exceeding the correlation time and in space exceeding the integral scale.

Since the simulations are run keeping the driving pressure gradient constant, the slope of the velocity profile at the bottom wall is invariant among the different simulations. For increasing stratification, however, we observe a clear separation of the domain into two different regions: a turbulent region near the bottom wall ($z^+ < 80$), where the usual near wall-turbulence is maintained, and a buoyancy-affected region near the free surface ($z^+ > 80$), where the stratification becomes important and the flow velocity increases. The flow velocity and the corresponding mass flow rate increase near the free surface for increasing Ri_τ: this is due to a reduction of the wall-normal momentum transport, and in particular of the wall shear stress (the driving pressure gradient being constant in all the simulations). In Fig. 3.14b we show the behavior of the mean temperature profiles as a function of the wall-normal coordinate z^+.

Regardless of the value of Ri_τ, we observe a region of large temperature gradient (near the free surface) topping a region where the temperature gradient is small and almost uniform ($z^+ < 80$). This region of well-mixed temperature near the bottom wall is due to the existence of active turbulence which effectively stirs the flow. The region near the free surface, characterized by the large temperature gradient and low mixing is usually called

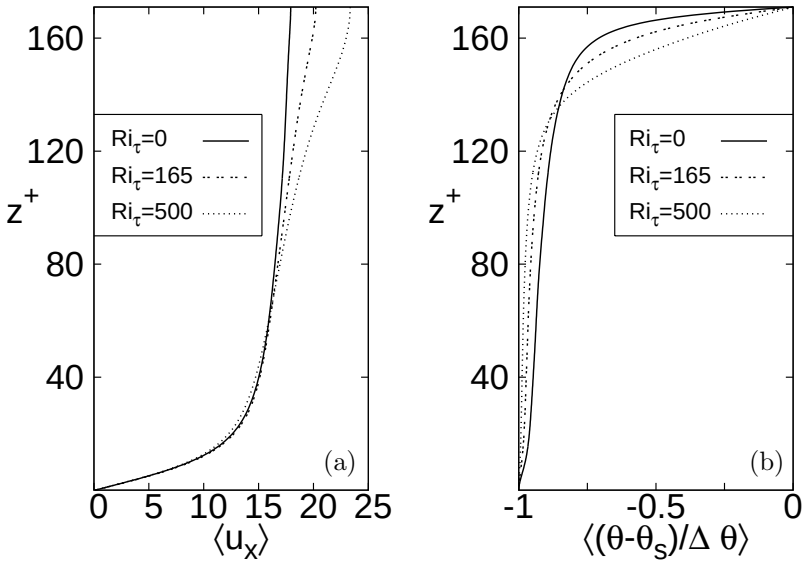

FIGURE 3.14 – Mean fluid streamwise velocity and temperature for stably-stratified free surface turbulence at $Ri_\tau = 0$ (solid line), $Ri_\tau = 165$ (dashed line) and $Ri_\tau = 500$ (dotted line). Panels: (a) mean fluid streamwise velocity, $\langle u_x \rangle$; (b) mean fluid temperature, $\langle (\theta - \theta_S)/\Delta\theta \rangle$.

thermocline: the thickness of the thermocline increases with Ri_τ, possibly indicating that mixing is increasingly reduced. Fluid parcels approaching the thermocline from the lower turbulent region do not have enough momentum to trespass the gravitational potential barrier created by the steep temperature gradient of the thermocline.

To observe the influence of the stable stratification on mixing and turbulence characteristics, the statistics of the fluid velocity and temperature fluctuations are examined. The root mean square (rms) of the fluid velocity fluctuations in each direction is shown in Fig. 3.15a-c.

For unstratified turbulence ($Ri_\tau = 0$), the velocity fluctuations near the bottom wall (where turbulence production is maximum) are similar to those observed in standard closed channel simulations, indicating that the near wall turbulence is not influenced by the presence of a free-slip top boundary (Lam and Banerjee [37]). The largest effect of the free surface on turbulence is the increase of $\langle u'_{x,rms} \rangle$ and $\langle u'_{y,rms} \rangle$ near the surface itself. Correspond-

ingly, $\langle u'_{z,rms} \rangle$ is largely reduced at the free surface and turbulence is nearly two-dimensional. For stratified turbulence ($Ri_\tau > 0$) we observe that the profiles of the velocity fluctuations are not altered in the near-wall region $z^+ < 40$, where the typical dynamics of the wall turbulence is maintained. A different situation occurs in the upper part of the domain ($z^+ > 90$), and in particular near the free surface. In this region, $\langle u'_{x,rms} \rangle$ and $\langle u'_{y,rms} \rangle$ decrease significantly as Ri_τ increases. This is due to the stabilizing effect induced by the fluid stratification, which reduces the turbulence fluctuations (turbulent kinetic energy is lost to potential energy). By contrast, $\langle u'_{z,rms} \rangle$ is less influenced by the fluid stratification near the free surface, owing to the strong constraint on u'_z imposed by the assumption of an undeformable free surface. This turbulence modulation has an impact on the distribution of temperature inside the free-surface channel. The rms of the temperature fluctuations, $\theta'_{rms}/\Delta\theta$, is shown in Fig. 3.15d. For neutrally buoyant and weakly-stratified flows ($Ri_\tau = 0$ and $Ri_\tau = 165$, respectively), the temperature fluctuations have a maximum at the free surface, or very close to it. This is due to the specific boundary condition prescribed for the energy equation (Eq. 3.3.3): owing to the constant heat flux condition, there is no constraint on the temperature value at the interface, thus producing a maximum on the temperature fluctuations. This situation changes when the fluid stratification becomes stronger. For $Ri_\tau = 500$, we observe a peak value for the temperature fluctuations occurring at $z^+ \simeq 150$ (and not at the free surface). Higher temperature fluctuations below the free surface are not due to the turbulence structures; rather, they are the consequence of the large scale IGW occurring in this region when Ri_τ increases (see also the following discussion on flow structures). We also observe that $\theta'_{rms}/\Delta\theta$ decreases with increasing Ri_τ.

Flow visualizations are now considered to identify specific flow structures in free-surface stratified turbulence. In particular, we use contour maps of the temperature field, since the temperature distribution is a clear marker of the underlying flow field structure. Results, obtained for simulations run at $Ri_\tau = 0$, $Ri_\tau = 165$ and $Ri_\tau = 500$, are shown in Fig. 3.16.

The mean flow is from left to right (positive x direction). For $Ri_\tau = 0$ (unstratified flow), temperature is passively advected by the velocity field. Bursts emanate from the bottom wall and produce upwelling motions of fluid traveling towards the free surface (blue regions in Fig 3.16a). To replace the fluid carried by upwellings, downward motions (downwellings) are

produced at the free surface and move towards the bulk region (red regions in Fig.3.16a). These mechanisms for the velocity/temperature distribution change when considering a stratified flow. Stratified flows can sustain a variety of wavy motions which have no counterpart in unstratified flows. The reason is the tendency for the vertical motions to be suppressed by buoyancy: a fluid particle which is displaced in the vertical direction by the velocity fluctuations tends to be restored to its original position; it may overshoot inertially and oscillate about this position (Zonta et al., 2012b [75]). This oscillation (IGW) is clearly visible near the free surface in Fig. 3.16c. In the remaining part of the domain, intermittent bursts associated with the near-wall turbulence are seen. Note that the region where the internal waves are observed coincides with the region where a thermocline exists (see Fig. 3.14b), proving that the internal waves may be produced in a thermocline (Ferziger et al., 2002 [25]).

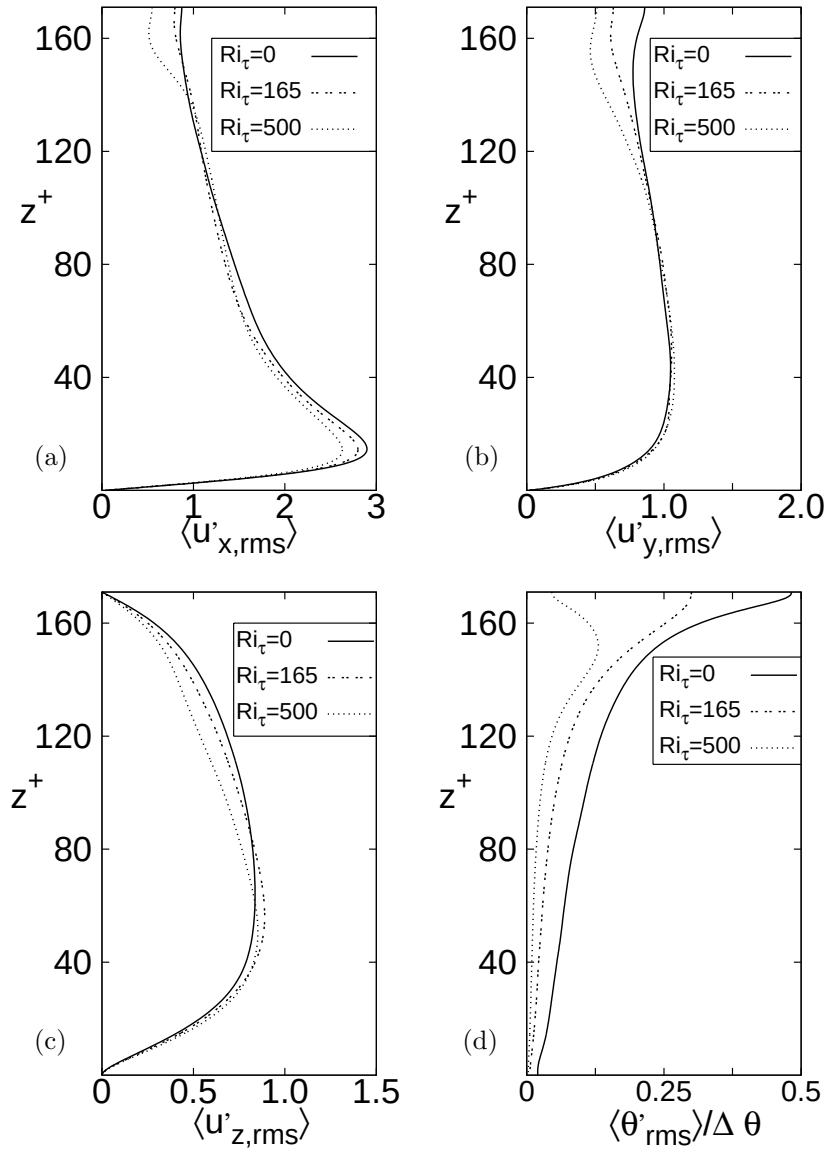

FIGURE 3.15 – Root mean square (r.m.s.) of fluid velocity and temperature fluctuations for stably stratified free surface turbulence at different Ri_τ. Panels: (a) streamwise velocity fluctuations, $\langle u'_{x,rms}\rangle$; (b) spanwise velocity fluctuations, $\langle u'_{y,rms}\rangle$; (c) wall-normal velocity fluctuations, $\langle u'_{z,rms}\rangle$; (d) temperature fluctuations, $\langle \theta'_{rms}\rangle/\Delta\theta$.

(a) Unstratified turbulence, $Ri_\tau = 0$

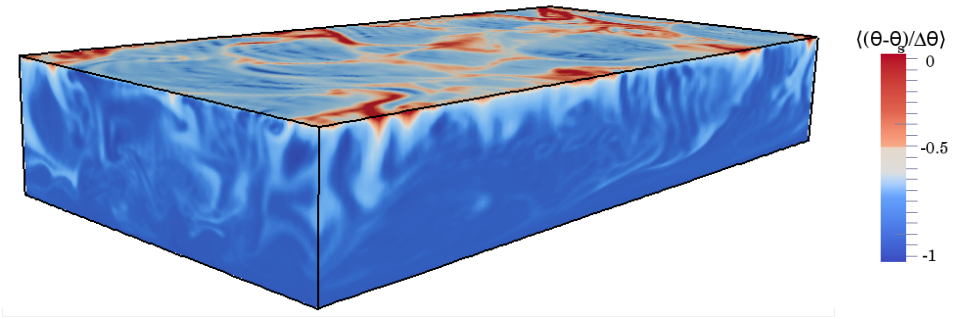

(b) Thermally-stratified turbulence, $Ri_\tau = 165$

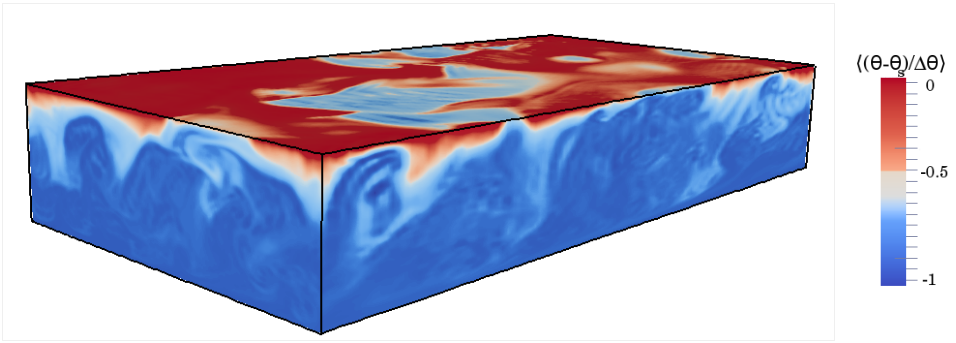

(c) Thermally-stratified turbulence, $Ri_\tau = 500$

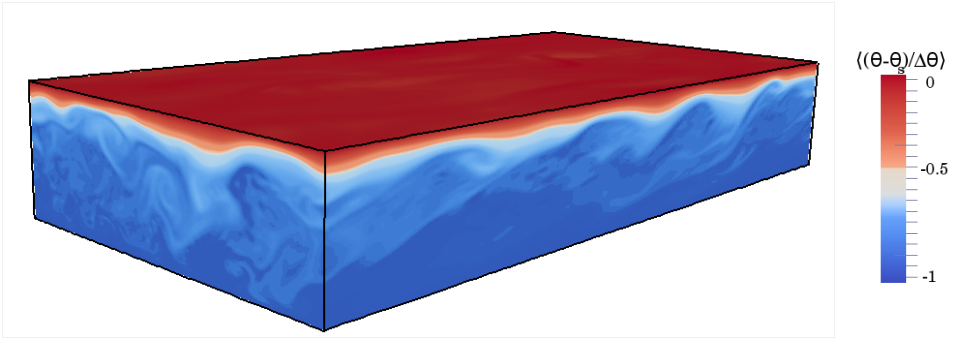

FIGURE 3.16 – Contour maps (three dimensional visualizations) of the temperature field. Panels: (a) simulation of unstratified turbulence ($Ri_\tau = 0$); (b) simulation of stratified turbulence ($Ri_\tau = 165$); (c) simulation of stratified turbulence ($Ri_\tau = 500$);

4

Passive particles in turbulent free-surface flow

In this chapter the dispersion of light particles floating on a flat shear-free surface of a turbulent open channel is examined. Direct numerical simulations of turbulence coupled with Lagrangian particle tracking are performed, considering different values of the shear Reynolds number ($Re_\tau = 171$ and 509), shear Richardson number, namely of stratification, ($Ri_\tau = 0$, 165 and 500) and of the Stokes number ($0.06 < St < 1$ in viscous units).

In the first section the problem is posed and the details of the simulations are provided; in the second section the cluster dynamics are discussed in detail via the time evolution of the cluster correlation dimension for the case of unstratified turbulent flow.

Results show that particle buoyancy induces clusters that evolve towards a long-term fractal distribution in a time much longer than the Lagrangian integral fluid time scale, indicating that such clusters over-live the surface turbulent structures which produced them.

In the third section it will examined in detail how the modification of turbulence due to the thermal stratification strongly influences the settling velocity of floaters in the bulk of the flow and the phenomena of clustering at the surface.

4.1 Introduction: problem definition

Buoyant particles transported by three-dimensional incompressible turbulence are known to distribute non-uniformly within the flow [23, 13, 38, 39]. In the particular case of light tracer particles (referred to as floaters here-

inafter) in free-surface turbulence, non-uniform distribution is observed on the surface, where floaters form clusters by accumulating along patchy and string-like structures [38]. Clustering occurs even if floaters have no inertia, and in the absence of floater-floater interaction, surface tension effects, or wave motions [38]. Differently from the case of inertial particles, in which clustering is driven by inertia and arises when particle trajectories deviate from flow streamlines, clusters are controlled by buoyancy, which forces floaters on the surface. The physical mechanism governing buoyancy-induced clustering is closely connected to the peculiar features of free-surface turbulence (discussed in Chap. 3), which is characterized by sources (resp. sinks) of fluid velocity where the fluid is moving upward (resp. downward) [23] . Once at the surface, floaters follow fluid motions passively and leave quickly the upwelling regions gathering in downwelling regions: here, fluid can escape from the surface and sink whereas floaters can not, precisely because of buoyancy [38].

In a series of recent papers [13, 38, 39] it was shown that floater clusters in free-surface turbulence form a compressible system that evolves towards a fractal distribution in several large-eddy turnover times (measured at the free-surface) and at an exponential rate. The macroscopic manifestation of this behaviour is strong depletion of floaters in large areas of the surface and very high particle concentration along narrow string-like regions, which are typical of scum coagulation on the surface of the sea [39]. From a statistical viewpoint, this is reflected by a peaked probability distribution function of particle concentration with power-law tails. A proper description of such power-law distribution requires a clear understanding of the mechanism by which floaters are segregated into filamentary clusters.

In the next section such mechanisms will be examined from a phenomenological point of view, and the cluster dynamics will be examined in connection with the characteristic timescale of the surface vortices. This analysis is of fundamental interest since it quantifies the temporal persistence of clusters with respect to the dominant surface flow scales, but reflects practically towards modeling of dispersion in many surface transport phenomena, such as the spreading of phytoplankton, pollutants and nutrients in oceanic flow [39].

Once these dynamics will be explained in the case of neutrally buoyant

turbulent open channel flow, the effect of a thermal stratification on such mechanisms will be examined.

4.2 Behaviour in the turbulent open channel

4.2.1 Simulation parameters

The physical problem considered in this study is floater dispersion at the free surface of a turbulent open channel flow. A sketch of the simulated flow configuration is shown in 3.1 in Sect. 3.2, together with the boundary conditions for the fluid (water). The flow field is calculated by integrating incompressible continuity and Navier-Stokes equations (3.2.1 in Sect. 3.2).

Floaters motion is described by a set of ordinary differential equations for velocity $\mathbf{v}_p$ and position $\mathbf{x}_p$ at each time step. In vector form:

$$\frac{d\mathbf{x}_p}{dt} = \mathbf{v}_p \ , \tag{4.2.1}$$

$$\frac{d\mathbf{v}_p}{dt} = \frac{(\rho_p - \rho_f)}{\rho_p}\mathbf{g} + \frac{(\mathbf{u}_{@p} - \mathbf{v}_p)}{\tau_p}(1 + 0.15\, Re_p^{0.687}) \ , \tag{4.2.2}$$

where $\mathbf{u}_{@p}$ is the fluid velocity at the floater position, interpolated with 6th-order Lagrange polynomials, ρ_p (resp. ρ_f) is the floater (resp. fluid) density, and $\tau_p = \frac{\rho_p\, d_p^2}{18\,\rho_f \nu}$ is the floater relaxation time based on the diameter d_p. The Stokes drag coefficient is computed using the Schiller-Naumann non-linear correction, required to ensure accurate evaluation of the drag force exerted on floaters with Reynolds number $Re_p = |\mathbf{u}_{@p} - \mathbf{v}_p|\, d_p/\nu > 0.2$. To calculate individual trajectories, periodic boundary conditions are imposed on floaters moving outside the computational domain in the homogeneous directions. In the wall-normal direction, particles reaching the free-slip surface still obey the buoyancy force balance, whereas elastic rebound is enforced at the no-slip bottom wall. It is remarked here that the buoyancy force balance does not automatically enforce particles to stay at the free surface. The details of numerical scheme are discussed in Chap. 2.

Samples of $\mathcal{N} = 2 \cdot 10^5$ floaters characterized by specific density $S = \rho_p/\rho_f = 0.5$ and diameter $d_p = 250\ \mu m$ (a value in the size range of large phytoplankton cells [55]) were considered. The corresponding values of the non-dimensional response time (Stokes number) $St = \tau_p/\tau_f$ with $\tau_f = \nu/u_\tau^2$ the viscous timescale of the flow, are $St^L = 0.064$ at Re_τ^L and $St^H = 0.562$ at

Re_τ^H. Floaters with density much less than that of the fluid were considered on purpose to confine their motion to the free surface and produce a behavior which resembles not at all that of neutrally buoyant, non-inertial particles.

4.2.2 Characterization of particle clustering through surface divergence

Most of the analyses for geophysical flows have been conducted considering two-dimensional incompressible homogeneous isotropic turbulence [69]. In such flows the divergence of the velocity field is zero by construction. However, the divergence in real surface flows introduced in Sect. 3.2.3, is defined as:

$$\nabla_{2D} = \frac{\partial u}{\partial x} + \frac{\partial v}{\partial y} = -\frac{\partial w}{\partial z} \ , \tag{4.2.3}$$

and does not vanish. Therefore floaters, forced to stay on surface by buoyancy, probe a compressible two-dimensional system [13], where velocity sources are regions of local flow expansion ($\nabla_{2D} > 0$) generated by subsurface upwellings and velocity sinks are regions of local compression ($\nabla_{2D} < 0$) due to downwellings [23]. In Fig. 4.1 a qualitative characterization of floater clustering on the free surface is proved by correlating the instantaneous particle patterns with the colormap of ∇_{2D}.

Due to buoyancy, floaters reaching the free surface can not retreat from it following flow motions: they can only leave velocity sources (red areas in Fig. 4.1) and collect into velocity sinks (blue areas in Fig. 4.1). Once trapped in these regions, floaters organize themselves in clusters that are stretched by the fluid forming filamentary structures. Eventually sharp patches of floater density distribution are produced, which correlate very well with the rapidly-changing patches of ∇_{2D}, as clearly shown by Fig. 4.1. Similar behavior (formation of clusters with fractal mass distribution) has been observed in previous studies [38, 13] for the case of Lagrangian tracers in surface flow turbulence without mean shear.

4.2.3 Time scaling of floaters clustering

Due to the close phenomenological connection between clustering and surface turbulence, the cluster length and time scales are expected to depend on local turbulence properties. In particular, one can quantify the temporal coherence of surface flow structures through their Lagrangian integral

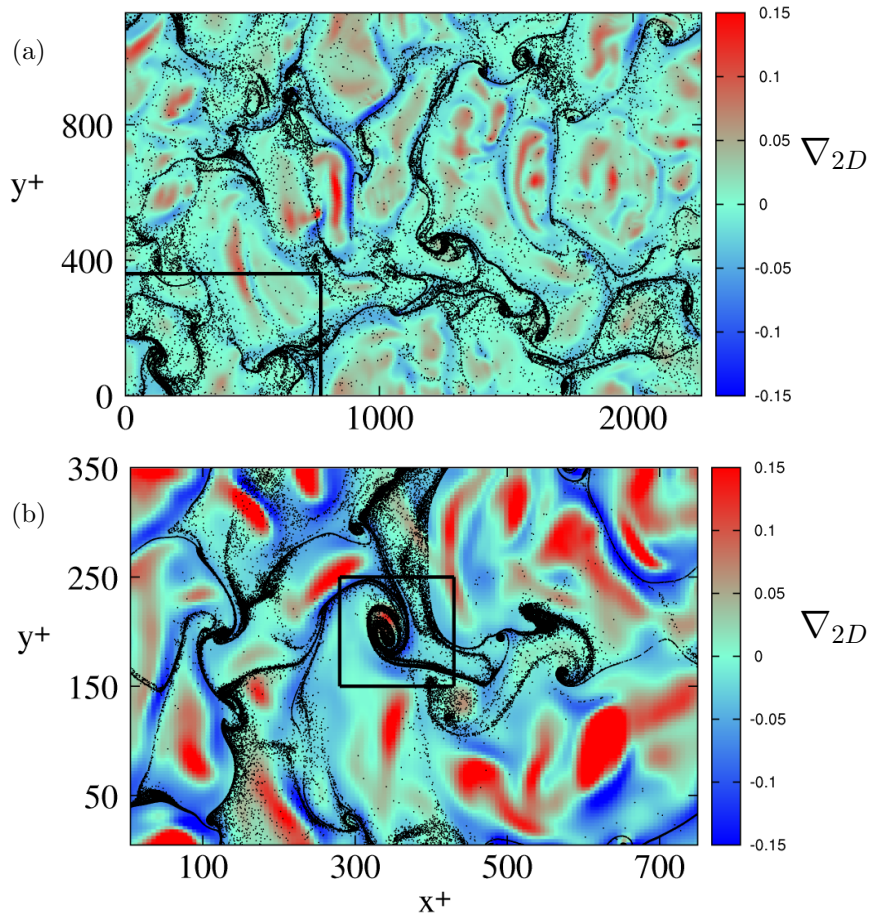

FIGURE 4.1 – Correlation between floater clusters and surface divergence ∇_{2D}: floaters segregate in $\nabla_{2D} < 0$ regions (in blue, footprint of sub-surface downwellings) avoiding $\nabla_{2D} > 0$ regions (in red, footprint of sub-surface upwellings). Panels: (a) Re_τ^H, $t^+ = 180$ upon floater injection; (b) Re_τ^L, $t^+ = 121$. The rectangle in panel (a) renders the relative domain size in the Re_τ^L simulation; the rectangle in panel (b) highlights the floater cluster shown in Fig. 4.3.

timescale (or, equivalently, their eddy turnover time [23]):

$$T_{\mathcal{L},ij} = \int_0^\infty R_{f,ij}(t, \mathbf{x}_f(t))dt \ , \tag{4.2.4}$$

where:

$$R_{f,ij}(t, \mathbf{x}_f(t)) = \frac{\langle \mathbf{u'}_{f,i}(t, \mathbf{x}_f(t)) \cdot \mathbf{u'}_{f,j}(t_0, \mathbf{x}_f(t_0)) \rangle}{\langle \mathbf{u'}_{f,i}(t_0, \mathbf{x}_f(t_0)) \cdot \mathbf{u'}_{f,j}(t_0, \mathbf{x}_f(t_0)) \rangle} \tag{4.2.5}$$

is the correlation coefficient of velocity fluctuations. Correlation coefficients were obtained upon ensemble-averaging (denoted by angle brackets) over all $\mathcal{N}$ fluid tracers released within the flow domain. Subscript f denotes the dependence of $R_{f,ij}$ on the instantaneous tracer position $\mathbf{x}_f(t)$. Velocity fluctuations were computed as $\mathbf{u'}_{f,i}(t, \mathbf{x}_{f,i}(t)) = \mathbf{u}_{f,i}(t, \mathbf{x}_{f,i}(t)) - \bar{\mathbf{u}}_{f,i}(t, \mathbf{x}_{f,i}(t))$, with $\bar{\mathbf{u}}_{f,i}(t, \mathbf{x}_{f,i}(t))$ the space-averaged Eulerian fluid velocity. Estimation of $T_{\mathcal{L},ij}$ is crucial to parameterize particle spreading rates and model large-scale diffusivity in bounded shear dispersion [68]. To compute $T_{\mathcal{L},ij}$ the channel height is divided into 50 uniformly-spaced bins filled with tracers. For each tracer the instantaneous value of the diagonal elements of $R_{f,ij}$ is computed with their integral over time to get $T_{\mathcal{L},11}$, $T_{\mathcal{L},22}$ and $T_{\mathcal{L},33}$. Finally, these were ensemble-averaged within each bin using only tracers initially located within the bin.

In Figure 4.2 are shown, for both Re_τ^H and Re_τ^L, the wall-normal behavior of the Lagrangian integral timescale of the fluid (symbols), obtained as $T_\mathcal{L} = [\langle T_{\mathcal{L},11}\rangle + \langle T_{\mathcal{L},22}\rangle + \langle T_{f,33}\rangle]/3$. Note that $\langle T_{\mathcal{L},33}\rangle \simeq 0$ at the surface. For comparison purposes, the Kolmogorov timescale, $\langle \tau_K \rangle$, is also shown (dot-dashed line). The value of $T_\mathcal{L}$ changes significantly with the distance from the wall: in the Re_τ^H simulation, $T_\mathcal{L} \simeq 120$ at the surface, a value 10 times larger than that near the wall (where $T_\mathcal{L} \simeq 14$) indicating that the characteristic lifetime of surface structures is significantly longer than that of near-wall structures. It is also evident that $T_\mathcal{L}$ is everywhere larger than $\langle \tau_K \rangle$, confirming clear scale separation between large-scale surface motions and small-scale dissipative structures.

To correlate the typical lifetime of surface motions with that of floater clusters, it is examined the time-evolution of the local correlation dimension of clusters, $D_2(t)$ [39]. The same observable was studied experimentally also by Larkin et al. [39, 38] as a measure of the fractal dimension of floater distribution. Their main finding is that $\langle D_2(t)\rangle$ decays at an exponential rate from $\langle D_2(t=0)\rangle \simeq 2$ to $\langle D_2(t\to\infty)\rangle \simeq 1$, the decay time being approximately one surface eddy turnover time (defined as the typical time for the "largest" eddies to significantly distort in a turbulent flow). In this work, $D_2(t)$ for several surface clusters is computed, one of which is followed in time in Fig. 4.3. This particular cluster was generated by past upwelling motions, which it survived (Fig. 4.3(a)), and is now found sampling a region of the free-surface reached by another upwelling motion (Fig. 4.3(b), red area). Floaters are swept from the velocity source and redistribute at its

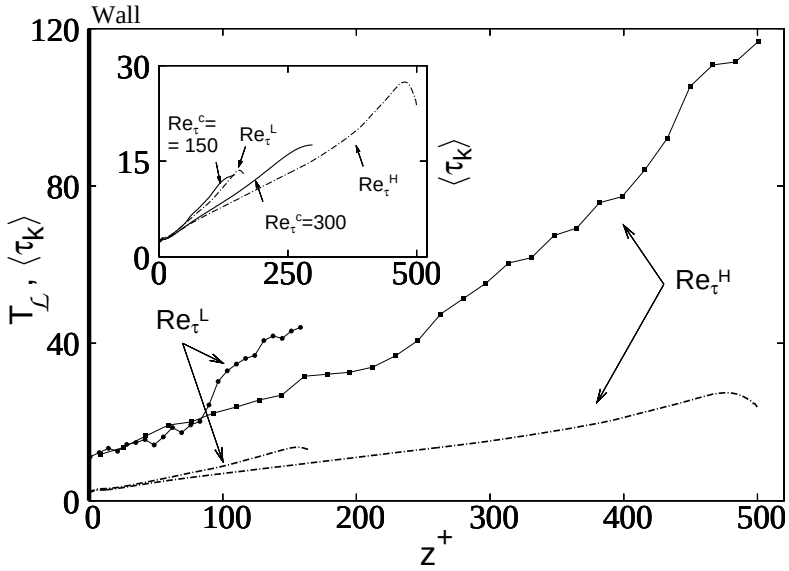

FIGURE 4.2 – Lagrangian integral fluid timescale ($T_{\mathcal{L}}$, symbols) and Kolmogorov timescale ($\langle \tau_K \rangle$, lines) in open channel flow at Re_τ^H (squares) and at Re_τ^L (circles), as function of the wall-normal coordinate z^+. The inset compares the behavior of $\langle \tau_K \rangle$ in open channel flow with that in closed channel flow (at $Re_\tau^c = 150$ and 300, solid lines).

edges maintaining the cluster spatial connection, as shown in Fig. 4.3(c). As time progresses (Fig. 4.3(d)), the cluster reshapes generating sharp density fronts.

Upon isolating the floaters sub-sample Φ_j for each cluster forming on the surface, the conditioned correlation dimension is computed at each time step $D_2(\Phi_j, t)$. The instantaneous value of $D_2(\Phi_j, t)$ for the specific cluster examined in Fig. 4.3 is given in each figure panel and shows a decrease in time associated to the formation of filamentary clusters: $D_2(\Phi_j, t) \simeq 1.67$ at relatively short times ($t \simeq 0.7T_{\mathcal{L}}$, Fig. 4.3(a)); and $D_2(\Phi_j, t) \simeq 1.14$ at much larger times ($t \simeq 3.9T_{\mathcal{L}}$, Fig. 4.3(d)). These values are also included as circles in panel (b) of Fig. 4.4, where it is shown the time behavior of the ensemble-averaged correlation dimension: $\langle D_2(t) \rangle = \sum_{j=1}^{\mathcal{N}_c} D_2(\Phi_j, t)$ (red line), with $\mathcal{N}_c$ the number of clusters over which averaging was made ($\mathcal{N}_c = 10$ for the profiles shown in Fig. 4.4). To render the intermittency of the clustering phenomenon, and to quantify the uncertainty associated with our measurement, is also plotted the standard deviation from $\langle D_2(t) \rangle$ (error bars). The black line in each panel represents the estimate of $\langle D_2(t) \rangle$

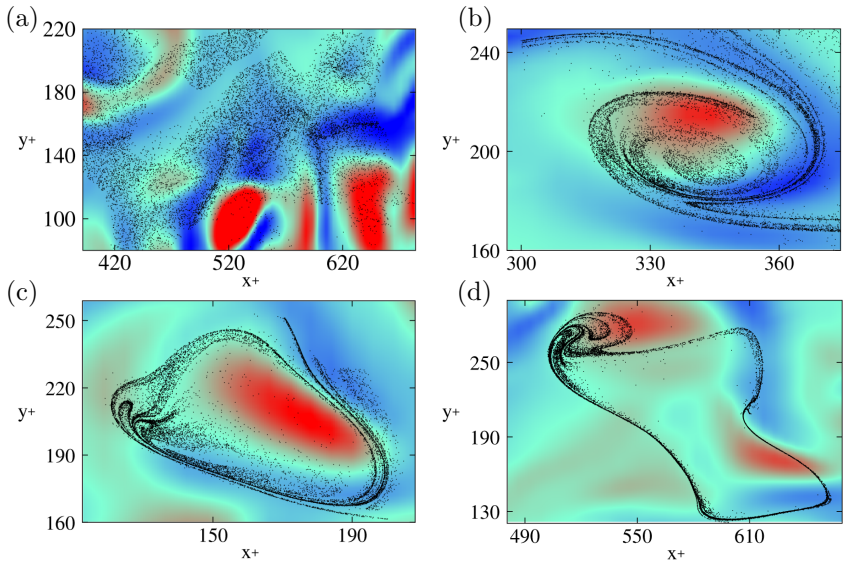

FIGURE 4.3 – Time evolution of the floater cluster highlighted in Fig. 4.1(b). The cluster is examined following its Lagrangian path, with Eulerian coordinates in each snapshot changing accordingly. Upon reaching the surface within an upwelling, floaters start to collect into a neighboring downwelling (blue region) at time $t^+ \simeq 36 \simeq 0.7T_{\mathcal{L}}$. Then, they are hit by a subsequent upwelling (red region) at time $t^+ \simeq 121 \simeq 2.4T_{\mathcal{L}}$ (a), and scattered around at time $t^+ \simeq 145 \simeq 2.9T_{\mathcal{L}}$ (b). Eventually, they form a highly-concentrated filamentary pattern at time $t^+ \simeq 193 \simeq 3.9T_{\mathcal{L}}$ (c). This pattern exhibits strong time persistency and over-lives several surface-renewal events.

obtained assuming an exponential decay rate [39, 38]. In the present flow configuration, the decay time is given as proportional to the value of $T_{\mathcal{L}}$ at the free-surface. The best fit to the data is given by a relation of the type $\langle D_2(t) - D_2(\infty)\rangle \propto exp(-t/\alpha T_{\mathcal{L}})$ with $\alpha \simeq 5$ for both Re_τ^H and Re_τ^L. This result proves the long-time persistency of surface clusters, that evolve in a time significantly larger than $T_{\mathcal{L}}$ to a steady state where the measured $\langle D_2(t)\rangle$ approaches a value approximately equal to 1, in agreement with the formation of filament-like structures observed in Fig. 4.3. Present findings confirm qualitatively those of Larkin et al. [39, 38] but show a slower decay time (larger than $T_{\mathcal{L}}$ and, in turn, larger than one eddy turnover time). This may be due to the different 3D flow instance considered below the 2D free surface. $\langle D_2(t)\rangle$ has an asymptotic behavior because of the non-interacting point-particle assumptions adopted. More realistic physical modelling for

particles interacting with surface forces could lead to different long-time behavior.

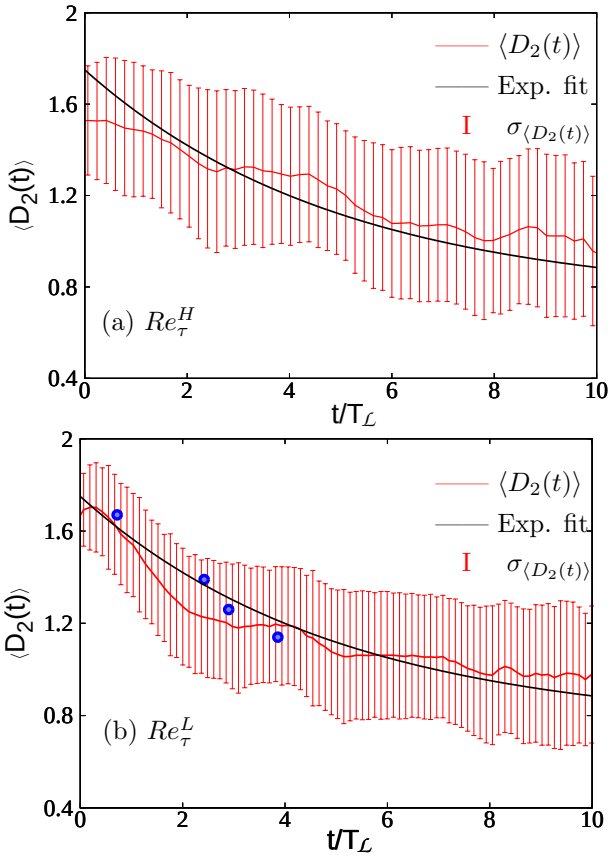

FIGURE 4.4 – Time evolution of the cluster correlation dimension $\langle D_2(t)\rangle$ at the free surface. Circles in panel (b) represent the instantaneous values of D_2 for the floater cluster shown in Fig. 4.3. Panels: (a) Re_τ^H; (b) Re_τ^L. The red line in each panel shows the mean correlation dimension, $\langle D_2(t)\rangle$, the black line represents the estimate of $\langle D_2(t)\rangle$ yield by an exponentially-decaying fit: $\langle D_2(t) - D_2(\infty)\rangle \propto exp(-t/\alpha T_\mathcal{L})$ with $\alpha \simeq 5$ for both Re_τ^H and Re_τ^L. The red area represents the standard deviation from $\langle D_2(t)\rangle$. Time is given as proportional to the Lagrangian integral timescale of the flow at the free-surface.

4.3 Influence of thermal stratification on the surfacing and clustering of floaters

In this section the influence of thermal stratification on the particles dynamics studied in the previous section, will be examined.

4.3.1 Simulation parameters

The reference geometry is the same of previous section with a stable stratification obtained by imposing a constant heat flux at the surface and an adiabatic condition at the wall (see Fig. 2.1).

The system of equations resolved, recalled in Sect. 3.3 dimensionless form, are the conservation of mass 3.3.1, momentum 3.3.2 and energy 3.3.3 of the fluid.

For the fluid velocity, no-slip (resp. no-stress) boundary conditions are enforced at the bottom (resp. top) boundary and the dimensionless Reynolds, Grashof and Prandtl number are defined in Sect. 3.3.

Direct Numerical Simulations (DNS) coupled with Lagrangian Particle Tracking were performed to investigate the role of the fluid stratification on the dispersion of the floaters with different inertia (see Table 4.1). As ins Sect. 3.3, all the simulations are run at reference Prandtl number $Pr = 5$, Reynolds number $Re_\tau = 171$ and three different values of the Richardson number are considered in this study $Ri_\tau = Gr/Re_\tau^2$, which measures the importance of buoyancy compared to inertia: $Ri_\tau = 0$, $Ri_\tau = 165$ and $Ri_\tau = 500$.

To analyse the problem of the dispersion of the floaters, samples of $N_P = 10^5$ floaters characterised by $d_p = 250\mu m$ (a value in the size range of large phytoplankton cells, Ruiz et al., 2004) and by four different specific densities $S = \rho_p/\rho_f$: $S = 0.5$, $S = 0.7$, $S = 0.8$ and $S = 0.9$ are considered. The corresponding values of the non-dimensional response time of the floaters (Stokes number $St = \tau_p/\tau_f$, with $\tau_f = \nu/u_\tau^2$ the viscous timescale of the flow) ranges within $St = 0.06 \div 0.11$. A summary of the simulations parameters is provided in Table 4.1.

4.3.2 Floater surfacing

Floaters are initially positioned at the bottom wall and, being lighter than the fluid, rise towards the free surface. To quantify the surfacing process, the

Simulation	Re_τ	Ri_τ	$S = \rho_p/\rho_f$	$St = \tau_p/\tau_f$
S1	171	0	0.5	0.063
			0.7	0.089
			0.8	0.102
			0.9	0.114
S2	171	165	0.5	0.063
			0.7	0.089
			0.8	0.102
			0.9	0.114
S3	171	500	0.5	0.063
			0.7	0.089
			0.8	0.102
			0.9	0.114

TABLE 4.1 – Floater surfacing and clustering in stratified free-surface turbulence: summary of the simulation parameters.

number of floaters n (normalized by the total number of floaters N_P) that have reached the free surface is counted as a function of time t expressed in wall units ($t^+ = tu_\tau^2/\nu$). The quantity n/N_P for each value of the specific density S is computed. The first case considered is the case of floaters moving in neutrally buoyant turbulence ($Ri_\tau = 0$, Fig. 4.5a). Obviously, according to their specific density, those floaters with the lowest density are the first to reach the free surface. The surfacing process can be considered complete at $t^+ \simeq 400$ for $S = 0.5$, at $t^+ \simeq 600$ for $S = 0.7$, at $t^+ \simeq 1000$ for $S = 0.8$ and at $t^+ > 1400$ for $S = 0.9$.

The effect of the thermal stratification on the surfacing of the floaters is shown in Fig. 4.5b just for the two cases in which the floaters have maximum and minimum rise velocity: $S = 0.5$ and $S = 0.9$. Since the effect of the fluid stratification on the surfacing of the floaters is more evident for the floaters with $S = 0.9$, the discussion is limited to this case.

In the first part of the surfacing process, the fluid stratification prevents a larger number of floaters from reaching the free surface: at $t^+ \simeq 400$, $n/N_P \simeq 0.3$ for $Ri_\tau = 0$ and $n/N_P \simeq 0.15$ for $Ri_\tau = 500$ (a value half the size). In the second part of the surfacing process the situation reverses with the fluid stratification enhancing the number of the floaters that reach the free surface: at $t^+ > 1000$, $n/N_P \simeq 0.8$ for $Ri_\tau = 0$ and $n/N_P \simeq 0.9$ for $Ri_\tau = 500$. From a physical point of view, these results suggest that (i) the rise velocity of the faster floaters (those reaching the free surface before $t^+ = 400$) is reduced by the fluid stratification and that (ii) the rise velocity

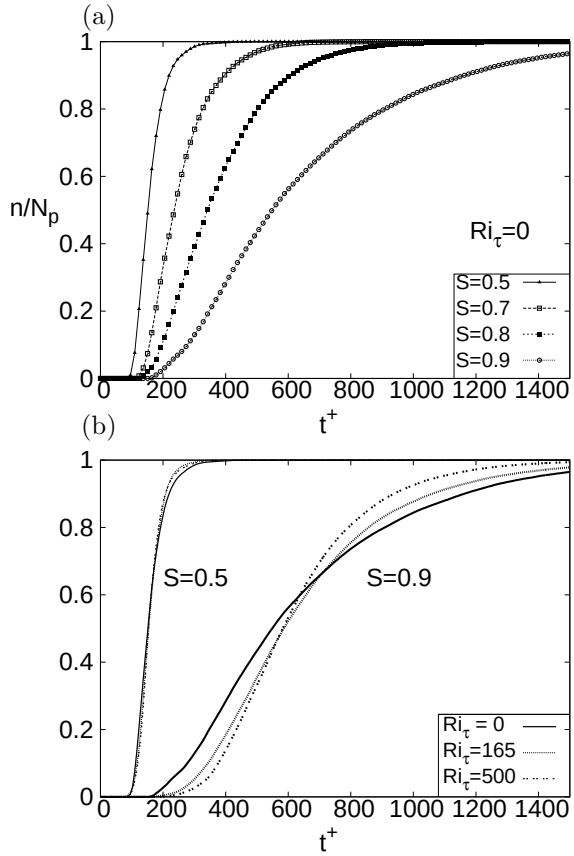

FIGURE 4.5 – Time behavior of the normalized number of floaters (n/N_P) settling at the free surface. Panels: (a) the effect of the floaters specific density (S) on n/N_P in unstratified turbulence ($Ri_\tau = 0$); (b) the effect of thermal stratification (Ri_τ) on n/N_P for $S = 0.5$ and $S = 0.9$.

of the slower floaters is enhanced by the fluid stratification (those reaching the free surface after $t^+ = 1000$). This observation is necessarily related to the changes in the structure of turbulence, which is known to influence the rise velocity of light particles (Maxey, 1987 [42]; Ruiz et. al [55], 2005; Marchioli et al., 2007 [41]).

To characterize further the surfacing process, the time taken by each floater to reach the free surface t_e is quantified explicitly. The probability distribution function (pdf) of t_e (expressed in wall units, t_e^+) is shown in Fig. 4.6. The abscissa of the maximum of the $pdf(t_e^+)$ is the expected value.

For $Ri_\tau = 0$ (Fig. 4.6a), the expected value decreases for decreasing S (i.e. for increasing the buoyancy of the floater): the lower the density of the floater, the larger its buoyancy drift and the shorter the time taken to reach the surface (see also Fig. 4.5a). In particular, $t_e^+ \simeq 320,\ 220,\ 200$ and 150 for $S = 0.9,\ 0.8,\ 0.7$ and 0.5, respectively.

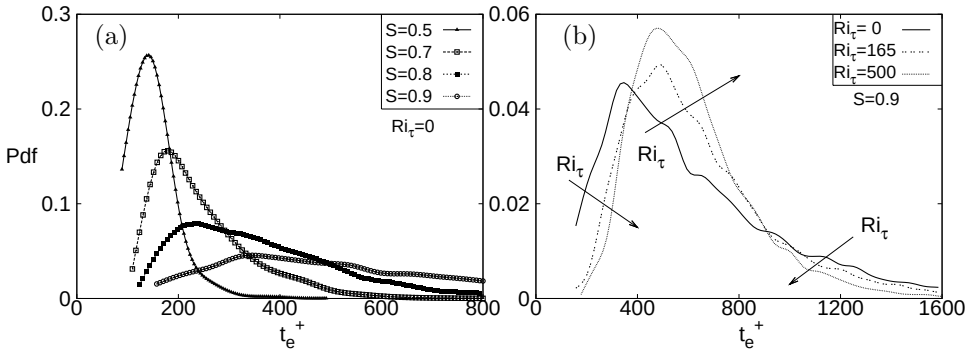

FIGURE 4.6 – Probability density function (pdf) of floaters exit time (t_e^+). Panels: (a) the effect of floaters specific density (S) on $pdf(t_e^+)$ in unstratified turbulence ($Ri_\tau = 0$); (b) the effect of thermal stratification (Ri_τ) on $pdf(t_e^+)$ for $S = 0.9$.

It could be noted that, as the floater density becomes closer to that of the fluid ($S \to 1$), the $pdf(t_e^+)$ becomes broader, with decreasing $\max\{pdf(t_e^+)\}$ and higher tails: $\max\{pdf(t_e^+)\} \simeq 0.25,\ 0.15,\ 0.08$ and 0.05 for $S = 0.5,\ 0.7,\ 0.8$ and 0.9, respectively. The dynamics of the floaters with a stronger buoyancy is less influenced by the turbulence fluctuations and the dispersion of the exit time (the tails of the $pdf(t_e^+)$) is reduced. Fig. 4.6b shows the distribution of the exit time of the floaters for $S = 0.9$ and different Richardson number Ri_τ (different fluid stratification): arrows point in the direction of increasing stratification (increasing Ri_τ). The expected value of t_e^+ increases for increasing stratification: from $t_e^+ = 350$ for $Ri_\tau = 0$ to $t_e^+ = 500$ for $Ri_\tau = 500$. Also, the value of $\max\{pdf(t_e^+)\}$ increases for increasing the fluid stratification, ranging from $\max\{pdf(t_e^+)\} \simeq 0.45$ for $Ri_\tau = 0$ to $\max\{pdf(t_e^+)\} \simeq 0.55$ for $Ri_\tau = 500$. These results indicate that the velocity of the faster floaters (those reaching the free surface at short times) in unstratified turbulence is larger compared to the corresponding value in stratified turbulence (but the number of floaters associated to this value of

t_e^+ increases for increasing Ri_τ). Finally, a crossover between the $pdf(t_e^+)$ curves occurring at $t_e^+ \simeq 900$ is observed: for unstratified turbulence, there is a significant number of floaters reaching the free surface at large time ($t_e^+ > 900$).

4.3.3 Floater clustering

Once at the free surface, floaters cannot escape from it (due to their buoyancy) and their dynamics is closely related to the local structure of the velocity field. Turbulence at the free surface is nearly two dimensional, and can be characterized by the divergence of the velocity field (Schumacher, 2003 [63]; Eckhard and Schumacher, 2001 [23]):

$$\nabla_{2D} = \frac{\partial u'}{\partial x} + \frac{\partial v'}{\partial y} = -\frac{\partial w'}{\partial z}. \tag{4.3.1}$$

In the present flow configuration $\nabla_{2D} \neq 0$ at the free surface. Therefore, floaters moving on the free surface probe a compressible system (Cressman et al., 2004 [13]), where velocity sources are regions of local flow expansion ($\nabla_{2D} > 0$) generated by upwellings, and velocity sinks are regions of local flow compression ($\nabla_{2D} < 0$). In Fig. 4.7 a qualitative characterization of the clustering of the floaters on the free surface is provided by correlating the instantaneous position of the floaters with the contour maps of ∇_{2D}.

In particular, the behaviour of floaters with $S = 0.5$ (left panels) and $S = 0.9$ (right panels) for $Ri_\tau = 0$ (Fig. 4.7a-b) is considered, $Ri_\tau = 165$ (Fig. 4.7c-d) and $Ri_\tau = 500$ (Fig. 4.7e-f).

To compare the results obtained with the same number of floaters settled at the free surface, the distribution of the floaters in Fig. 4.7 are computed at different t^+, depending on the specific density of the floaters: $t^+ \simeq 200$ for $S = 0.5$ and $t^+ \simeq 1000$ for $S = 0.9$ (this corresponds to $n/N_P \simeq 0.8$, see Fig. 4.5b). For $Ri_\tau = 0$ (Fig. 4.7a-b) it is observed that the floaters escape velocity sources (red areas in Fig. 4.7a-b) and collect into velocity sinks (blue areas in Fig. 4.7a-b). Once trapped in these regions, the floaters organize in clusters that are stretched by the fluid forming filamentary structures: these filaments of floaters correlate very well with the behavior of $\nabla_{2D} < 0$. The situation changes when considering a stratified fluid. Upwellings/downwellings at the free surface are less intense and the filamentary structures less evident, floaters being homogeneously distributed (Figs. 4.7c-f). To quantify these observations, the probability of

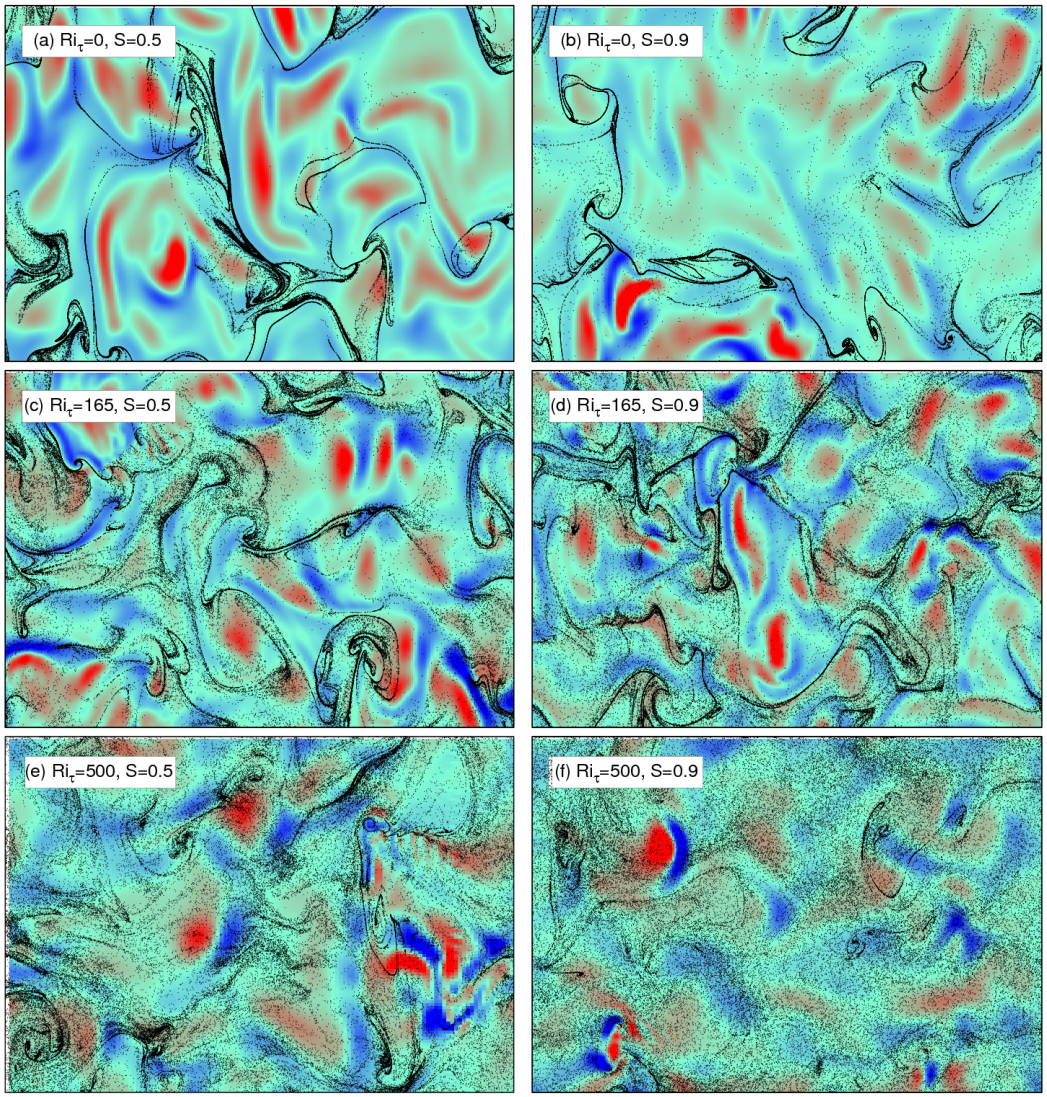

FIGURE 4.7 – Correlation between floater clusters and surface divergence ∇_{2D} for $Ri_\tau = 0,\ 165$ and 500 and for floater specific density $S = 0.5$ and $S = 0.9$. Panels: (a) $Ri_\tau = 0$ and $S = 0.5$; (b) $Ri_\tau = 0$ and $S = 0.9$; (c) $Ri_\tau = 165$ and $S = 0.5$; (d) $Ri_\tau = 165$ and $S = 0.9$; (e) $Ri_\tau = 500$ and $S = 0.5$; (f) $Ri_\tau = 500$ and $S = 0.9$.

finding a floater in a flow region characterised by a specific value of ∇_{2D}, $pdf(\nabla_{2D})$ is computed. For $Ri_\tau = 0$ (Fig. 4.8a), floaters accumulate in regions of $\nabla_{2D} < 0$ (downwellings). This result does not depend on *the* floater buoyancy since, for all values of S, $\max\{pdf(\nabla_{2D})\} \simeq 0.25$ occurs for $\nabla_{2D} \simeq -0.02$. The effect of the fluid stratification on the clustering of the floaters at the surface is shown in Fig. 4.8b-c, where the behavior of $pdf(\nabla_{2D})$ at varying Ri_τ and for the specific densities $S = 0.5$ (in Fig. 4.8b) and $S = 0.9$ (in Fig. 4.8c) is presented. As Ri_τ increases, a clear displacement of the maximum of the pdf towards larger values of ∇_{2D} (Fig. 4.8b-c) is observed. This corresponds to a physical situation in which the accumulation of the floaters into downwellings (∇_{2D}) does not occur, and the floaters are distributed more homogeneously over the free surface.

To quantify further the segregation of the floaters observed in Fig. 4.7, the Voronoi diagram (Monchaux et al., 2010 [44]) is used. The Voronoi diagram is a decomposition of the 2D surface into independent cells built around each floater. The area of each cell is therefore a measure of the local particle concentration: small areas indicate high concentration of the floaters, whereas large areas indicate low concentration of the floaters (see Fig. 4.9). In Fig. 4.10, it is shown the probability distribution function (pdf) of the Voronoi areas obtained by applying a Voronoi tessellation to the distribution of floaters shown in Fig.4.7.

In particular, Fig. 4.10a refers to the situation observed in Fig. 4.7a,c,e ($S = 0.5$), whereas Fig. 4.10b refers to the situation observed in Fig. 4.7b,d,f ($S = 0.9$). Regardless of the value of S, it is obtained similar trends for the probability distribution function of the Voronoi areas. For $Ri_\tau = 0$, the maximum of the pdf curves occurs for very small areas. This reflects a situation in which floaters cluster in regions characterized by a very high concentration. For increasing stratification, the situation changes and the values of the Voronoi areas increase, thus meaning that the clustering of the floaters is damped (i.e. the area surrounding each floater is larger). This confirms the qualitative observation (Fig. 4.7) that the thermal stratification imposed throughout the channel reduces the clustering of the floaters at the surface.

Finally, the topology of the clusters at the free surface is characterised by computing the time evolution of the correlation dimension of clusters, $D_2(t)$ (Fig. 4.11). The correlation dimension is a measure of the topological features of the distribution of the floaters. For simple geometrical

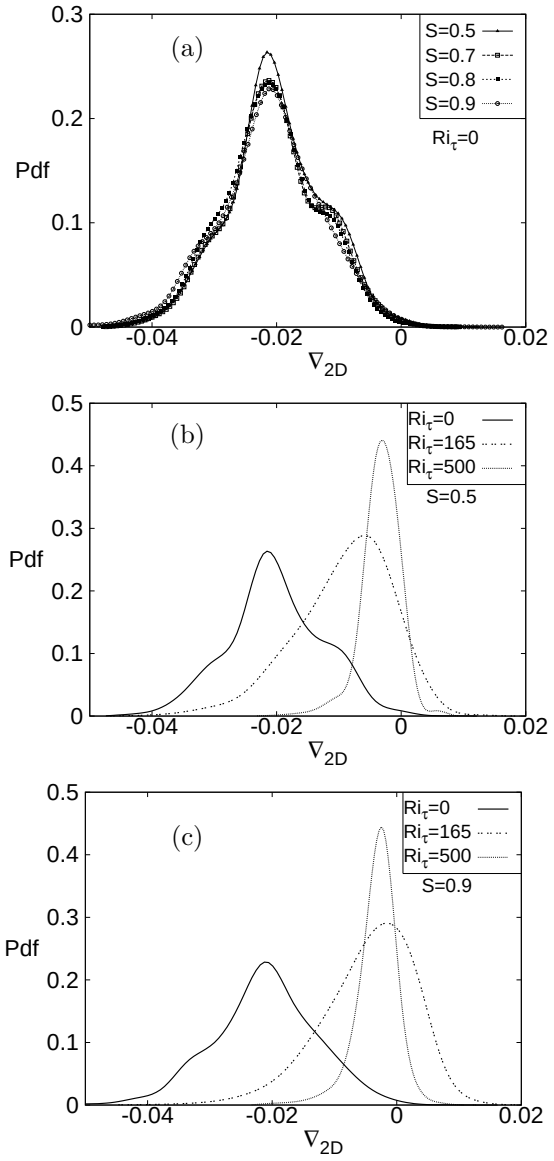

FIGURE 4.8 – Probability density function (pdf) of surface divergence ∇_{2D} computed at floaters position. Panels: (a) the effect of floaters specific density (S) on $pdf(\nabla_{2D})$ in unstratified turbulence; (b) the effect of thermal stratification (Ri_τ) on $pdf(\nabla_{2D})$ for $S = 0.5$; (c) the effect of thermal stratification (Ri_τ) on $pdf(\nabla_{2D})$ for $S = 0.9$.

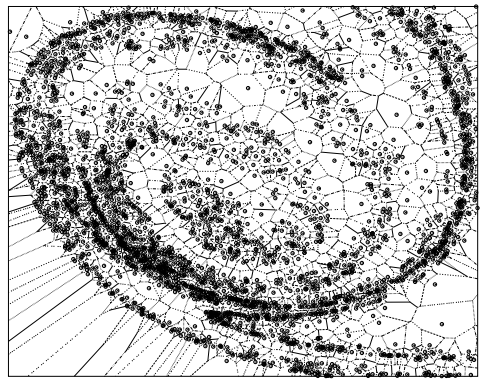

FIGURE 4.9 – Application of the Voronoi tessellation to the analysis of the clusters formed by the floaters. Voronoi diagram corresponding to the small box indicated in Fig. 4.1b.

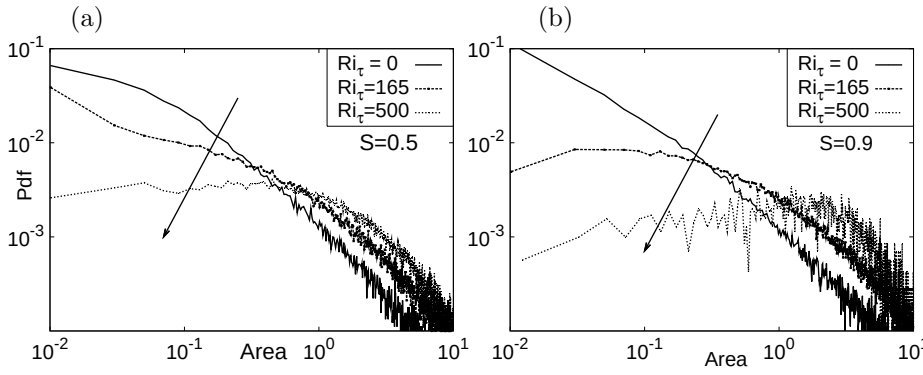

FIGURE 4.10 – Probability distribution function (pdf) of the Voronoi areas computed at the free surface for different Ri_τ. Panels: (a) *pdf* for floaters with specific density $S = 0.5$; (b) *pdf* for floaters with specific density $S = 0.9$.

structures like points, lines and surfaces, $D_2(t) = 0, 1, 2$ respectively. The behavior of $D_2(t)$ for the floaters with $S = 0.5$ and $S = 0.9$ and for all the values of Ri_τ is computed, starting the calculation when the floaters reach the free surface ($t^+ > 50$ for $S = 0.5$ and $t^+ > 150$ for $S = 0.9$, see Fig. 4.5b). Thr discussion will be focused considering $S = 0.5$ (Fig. 4.11a). For $Ri_\tau = 0$, $D_2(t)(@t = 0) \simeq 1.4$ and decays in time almost exponentially

towards $D_2(t) \simeq 1$. The initial value of $D_2(t)(@t = 0)$ is lower than in neutrally buoyant case showed in previous section, because here floaters are released from a plane close to the bottom wall and arrive at the free surface already segregated. Therefore, a segregation due to inertia is observed during the surfacing process. Once at the free surface, floaters segregate due to buoyancy. In a long-term limit $D_2(t) \simeq 1$, meaning that the floaters accumulate into filaments, i.e line-like structures (see also Fig. 4.7a-b for a clear visualization of this result). For $Ri_\tau > 0$, $D_2(t)(@t = 0) \simeq 1.5$ and does not decay in time. This reflects the physical observation that the filaments of the floaters in thermally-stratified flows are hardly seen (see also Fig. 4.7c-f) and the distribution of the floaters remains roughly two dimensional ($D_2(t) \simeq 1.5$).

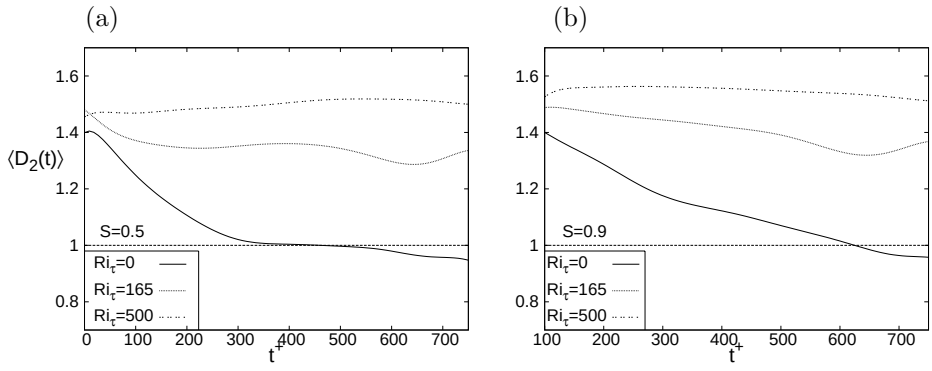

FIGURE 4.11 – Time evolution of the cluster correlation dimension $\langle D_2(t)\rangle$ at the free surface for different Ri_τ. Panels: (a) $\langle D_2(t)\rangle$ for floaters with specific density $S = 0.5$; (b) $\langle D_2(t)\rangle$ for floaters with specific density $S = 0.9$.

The segregation of the floaters into filaments for unstratified turbulence is due to the combined dynamics of upwelling/downwelling events. For stratified turbulence, upwellings and downwellings lose momentum to trespass the potential barrier created near the free surface by the temperature gradient. Therefore, it is clear that the homogeneous distribution of the floaters for stratified turbulence stems from the weakening of upwellings and downwellings.

5

Active particles in turbulent free-surface flow

In this chapter Direct Numerical Simulation of turbulent open channel flow is used in order to describe and analyse active particle systems and the complex dynamics which arises.

Preliminary results will be discussed for the case of shear Reynolds number $Re_\tau = 171$ and different values of shear Richardson number ($Ri_\tau = 0$, 165 and 500).

In the first section the model for the active particles and the details of the simulations are provided. In the second section the cluster dynamics are discussed for the case of turbulent open channel flow.

In the third section the effect of thermal stratification will be examined. It will be shown how the dynamics of micro-swimmer in marine stratified turbulence could be affected by the thermocline layer.

5.1 Introduction: problem definition

In recent years, a whole class of biological and physical systems which may be referred to as active matter or active particles, has been studied theoretically and experimentally [56, 67]. Examples of such systems are the self-propelled particles as phytoplankton cells, whose interaction with the leading fluid is non trivial.

A wide variety of external factors including nutrient concentration, gravity, and the rate of strain of the fluid affect the orientation of the swimming velocity of the cells [22, 21]. The resulting distribution is far from uniform. Gradients in concentration of plankton span a wide range of length scales,

ranging from regions of persistent upwelling at the equator with length scales of thousands of kilometres to microscale patchiness that occurs at the scale of centimetres.

To deal with aquatic flows, motile micro-organisms have developed many ways of adaptation [22]. One of those tends to orient the cell's swimming direction upward against gravity. The resulting balance between gravitational torque due to the asymmetric distribution of density and the hydrodynamic torque is known as gyrotaxis and will be examined in this chapter.
Gyrotaxis was discovered in 1985 by John Kessler [50, 49] by showing that phytoplankton cells tend to collect along the centerline of a laminar Poiseuille flow. Recent experimental observation shows that gyrotactic algae cells could be trapped in horizontal layers in laminar vertical shear. The phenomenon called 'gyrotactic trapping' [22, 21] occurs when vertically migrating cells accumulate where vertical gradients in horizontal velocity exceeds a critical shear threshold, causing cells to tumble end over end.
Only recently it was demonstrated that phytoplankton clustering could occur also in turbulence [20, 14, 15, 74, 16]. Numerical simulations have shown that gyrotactic algae generate small-scale clusters with fractal distibution [20, 74].
Shear, in the form of vertical gradients in horizontal fluid velocity, can be generated by tidal currents [60], wind stress, and internal waves and is often enhanced within thin layers. Moreover it is interesting to investigate how modulation of turbulent fluctuations controlled by thermal stratification, could affect the dynamics of phytoplankton cells. Next sections are devoted to understand these dynamics.

5.1.1 Governing equations for particles and parameters of simulation

The dynamics of a population of $N = 10^5$ swimming micro-organisms is simulated. Each micro-swimmmer is modelled as a spheroidal particle whose position $\mathbf{x}$ evolves according to

$$\frac{d\mathbf{x}}{dt} = \mathbf{u}(\mathbf{X}) + v_s\mathbf{p}, \tag{5.1.1}$$

where v_s is the mean cell's swimming speed, $\mathbf{u}$ the velocity of fluid in the position of swimmer and $\mathbf{p}$ the particle orientation. The orientation $\mathbf{p}$ of each

swimmer evolves in response to the biasing torques acting upon it. Under the assumptions that the microswimmers cells have a spheroidal geometry, the reorientation rate of the organisms is defined by the following balance of forces (Fig. 5.1):

$$\frac{d\mathbf{p}}{dt} = \frac{1}{2B}\left[\mathbf{k} - (\mathbf{k}\cdot\mathbf{p})\mathbf{p}\right] + \frac{1}{2}\omega \wedge \mathbf{p} \tag{5.1.2}$$

where $\mathbf{k} = [0, 0, 1]$ is a unit vector in the vertical upwards direction, $\omega = \nabla \wedge \mathbf{u}$ is the fluid vorticity and $B = \mu\alpha_{\perp}/(2h\rho g)$ is the gyrotactic reorientation time (h denotes the centre-of-mass offset relative to the centre-of-buoyancy, $\alpha_{\perp}$ is the dimensionless resistance coefficient for rotation about an axis perpendicular to $\mathbf{p}$, ρ and μ are the fluid density and viscosity, respectively). B is a key parameter for the dynamic of the cells since it represents the characteristic time a perturbed cell takes to return to vertical if $\omega = 0$. The first term on the right hand side of equation 5.1.2 describes the tendency of a cell to remain aligned along the vertical direction due to bottom-heaviness while the second term captures the tendency of vorticity to overturn a cell by imposing a viscous torque on it.

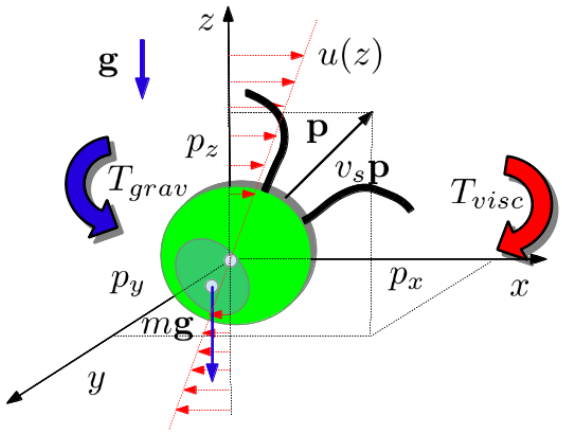

FIGURE 5.1 – Gyrotactic microorganisms swim with velocity V_s in a direction given by the orientation vector $\mathbf{p}$ set by a balance of torques. The torque due cell asymmetry (bottom heaviness: $\mathbf{T_{grav}}$) tends to align the cell to its preferential orientation along the vertical direction $\mathbf{k}$ whereas the torque due to flow ($\mathbf{T_{visc}}$) tends to rotate the cell.

Cell positions and swimming direction were integrated using the non-

dimensional form of equations 5.1.1 and 5.1.2

$$\frac{d\mathbf{x}^*}{dt^*} = \mathbf{u}^*(\mathbf{X}^*) + \Phi\mathbf{p}, \tag{5.1.3}$$

$$\frac{d\mathbf{p}}{dt^*} = \Psi\left[\mathbf{k} - (\mathbf{k}\cdot\mathbf{p})\mathbf{p}\right] + \frac{1}{2}\omega^* \wedge \mathbf{p} \tag{5.1.4}$$

where time, lengths and velocity were non-dimensionalised by using the friction velocity u_τ and fluid viscosity ν. Dimensionless parameters are $\Phi = v_s/u_\tau$ and $\Psi = \frac{1}{2B}\frac{\nu}{u_\tau^2}$. At each time step of the simulation, the local fluid velocity and vorticity at the particle positions, were calculated using Lagrangian interpolation (Chap. 2).

The reorientation timescale while known only for handful species, generally spans the range $B \simeq 0.1 - 10s$ and phytoplankton's swimming velocities are often in the range $V_s \simeq 10 - 1000\mu m/s$. In next simulations a fixed value of the swimming velocity equals to $100\mu m/s$ is used (the corresponding dimensionless value is $\Phi = 0.048$) which is a parameter based on Chlamydomonas augustae [14, 20]. While this specie has a value of the gyrotactic time scale equals to $3.4s$, simulations were performed by investigating the range $B \simeq 0.1 - 10s$ in particular $B = 0.1, 1, 10s$ which correspond to $\Psi_H = 1.13$, $\Psi_I = 0.113$, $\Psi_L = 0.0113$.

5.2 Turbulent open channel flow

Since the main mechanism which significantly affects the transport of swimming gyrotactic microorganisms in suspension is the interaction with the local variation of vertical gradient of streamwise fluid velocity ($\partial u/\partial z$), in figure 5.2 the trend of mean strain rate in turbulent open channel flow is shown. The value of mean strain rate ($\partial u/\partial z$) is higher at wall region and within $\simeq 40$ wall units, it drops to zero toward the surface ($z^+ = 0$).

Particles were initially released at the center of the channel with random initial orientations.

In figure 5.3 the trends of normalized concentrations along wall normal distance for the three values of Ψ are shown.

The domain was divided into wall-parallel slabs, of volume $V_{slab} = L_x \cdot L_y \cdot \delta z_{slab_i}$, where z_{slab_i} is the thickness of the slab, equally spaced. Particles contained in each slab were counted and the normalized concentration C/C_0 was computed as: $\frac{C}{C_0} = \frac{np_{slab_i}}{V_{slab_i}}\frac{V_{tot}}{np_{tot}}$ where np_{slab_i} is the number of particles

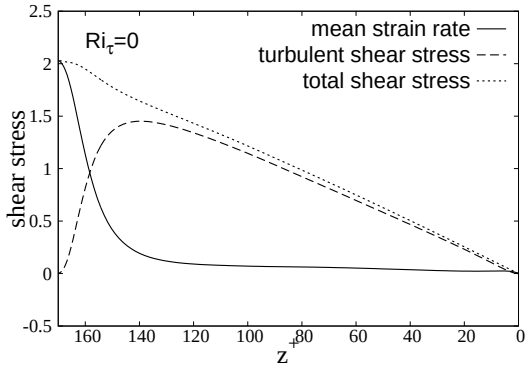

FIGURE 5.2 – Mean strain rate : $\partial_z u$ (solid curve), turbulent shear stress : $u'w'$ (dashed lines) and the total shear stress given by the sum of the previous contributions (dots), for the neutrally buoyant case ($Ri_\tau = 0$) and $Re_\tau = 171$

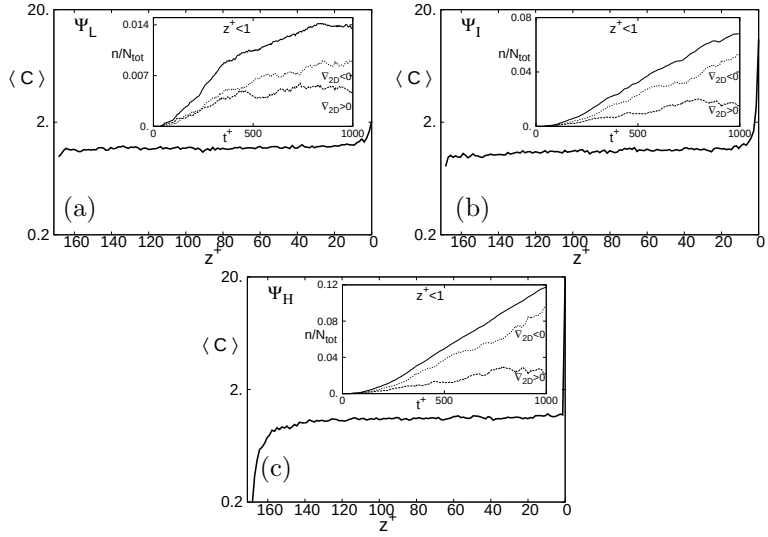

FIGURE 5.3 – Concentration in log-linear scale for Ψ_L (a), Ψ_I (b), Ψ_H (c) in the wall normal direction. The inset shows the number of particles which reach the surface ($z^+ = 0$) in time (solid curve). The relative contributions due to the number which arrive in downwellings ($\nabla_{2D} < 0$) and upwellings ($\nabla_{2D} > 0$) are also shown.

contained in the i-th volume V_{slab_i}, np_{tot} is the number of total particles and $V_{tot} = L_x \cdot L_y \cdot L_z$ is the total volume of the domain.

Figure 5.3(a) shows the case for Ψ_L, 5.3(b) shows the case for Ψ_I and

5.3(c) the case for Ψ_H.

The trends show a depletion of wall region and an increasing of concentration at the surface. Particles will tend to align with the vertical direction and reach the surface due to gyrotaxis. This trends will be more important at higher value of Ψ (or equivalently at lower values of B): plankton cells will react more rapidly to the perturbation due to local fluctuations and the result is a more stable vertical migration.

In the inset of figures 5.3 the number of particles which reach the upper layer ($z^+ < 1$) in time (solid curve) is shown with the number of particles which reach the surface in regions of upwelling (positive values of surface divergence)(see Chap. 4) and regions of downwelling (negative values of surface divergence). The trend is to sample mostly the regions of downwelling.

This result was already obtained in laminar downwelling flows [50] and generalised in homogeneous isotropic turbulence (HIT) [20]. In HIT, Durham and coworkers have motivated the clustering of gyrotactic particles in downwelling regions due to compressibility of the cell velocity. They argued that, since the velocity of cells is the superposition of the flow velocity $\mathbf{u}$ and of the swimming velocity $\Phi\mathbf{p}$, it could be obtained that

$$\nabla \cdot \mathbf{v} = \Phi \nabla \cdot \mathbf{p} = -\Psi\Phi\nabla^2 u_z$$

(where u_z is the vertical component of the velocity of fluid in the position of particles). The last expression was obtained in the limit of a large stabilizing torque ($B \ll 1$) and assuming that in this limit, the cell orientation reaches an equilibrium with local vorticity.

The slope of the curve n/N_{tot} increases as Ψ increases showing that the number of particles which reach the surface is proportional to their tendency to be aligned upward. In the case of Ψ_H the number of plankton cells monotonically increases in time: particles in this case reach the surface and will not escape from it. Since the simulations are performed in the hypothesis of dilute system (one way coupling), the simulations are shown until $t^+ \approx 1000$ when almost the 10% of total number of particles have reached the surface. Again the number of particles which reach the upper layer in upwelling is stationary after a certain temporal window, while it is not true for the particles which arrive already segregated into downwellings or which are moving from upwellings. In figure 5.4 the instantaneous configuration of particles at the surface for $t^+ \approx 1000$ and the different Ψ are shown.

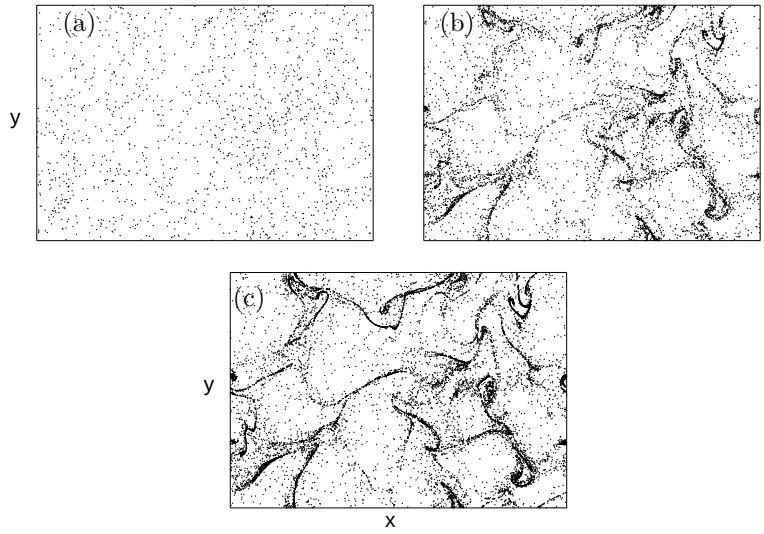

FIGURE 5.4 – Surface clustering of gyrotactic particles at the same instant for Ψ_L (a), Ψ_I (b) and Ψ_H (c)

The clustering is more evident for Ψ_I and Ψ_H, with filamentary structures which resemble that of passive particles (Chap. 4). In figure 5.5 the trend of $< p_z >$ in function of wall distance is shown, for the three values of Ψ. As done for the concentration, also in this case the particles were selected accordingly to their positions and the mean values were computed in each horizontal slab. For the Ψ_H it could be noted that within 20 wall units from the wall (away from the maximum shear) the mean value of p_z tends to the maximum value which means that particles have a persistent tendency to swim upward as expected.

As we decrease Ψ, this tendency decrease which is intuitive since lower values of Ψ cause higher tendency of this particles to be driven away from vertical upward.

In figure 5.5(b) the mean value of the vertical total velocity of particles along wall normal distance is shown. It is related to the value of p_z: the higher the value of Ψ, the higher the mean value of u_z. Interestingly, for the case of Ψ_L and Ψ_I within the wall region, the mean value of u_z of particles is negative or close to zero. Even if the statistics in this layer are affected

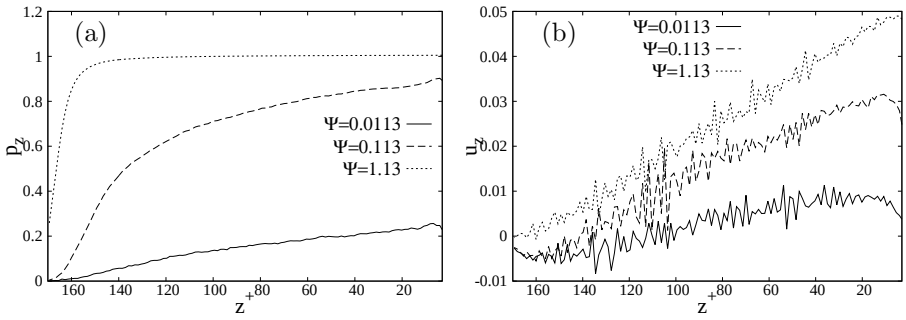

FIGURE 5.5 – Mean vertical orientation (a) and mean vertical velocity (b) of cells in wall normal direction. Solid curve refers to Ψ_L, dashed lines to Ψ_I and dots to Ψ_H

by the small number of particles (see figure 5.3), it could be related to the phenomenon of tumbling: the vertical motion is destroyed by the presence of high value of shear which causes particles to tumble end over end [21].

5.3 Stratified open channel flow

Thermal stratification induces at the surface an increase of the mean streamwise velocity (Chap. 3). This causes a different trend in the mean strain rate which is shown in figure 5.6 in function of the Richardson shear number.

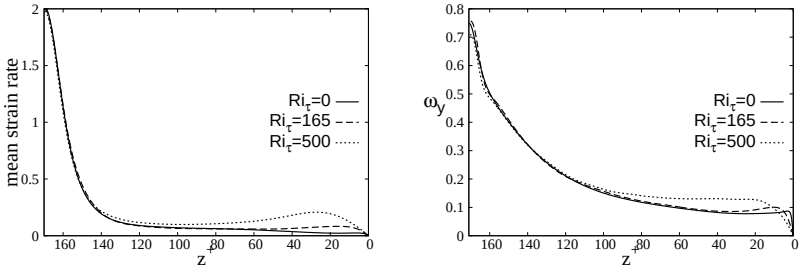

FIGURE 5.6 – Mean laminar strain rate (left) : $\partial_z u$ for $Ri_\tau = 0$ (solid curve), $Ri_\tau = 165$ (dashed lines), and $Ri_\tau = 500$ (dots). Mean spanwise vorticity (right): $\omega_y = \partial_z u + \partial_x w$. All cases refers to $Re_\tau = 171$

As we increase the stratification (namely the value of Richardson number), the mean strain rate is not still constant but shows a maximum which

appears for $z^+ \approx 20$ at $Ri_\tau = 500$. This region is the region of thermocline, rapid variation of temperature profile in which internal gravity waves could form. In figure 5.6 the mean profile of spanwise vorticity is shown. By definition an increase of mean strain rate cause an increase of the spanwise vorticity $\omega_y = \partial_z u + \partial_x w$ which drops to zero at surface for the imposed condition of free-slip.

Results are shown in figure 5.7 in which the mean profiles of concentration is presented in wall distance for the different stratifications (the case of neutrally buoyant flow is reported here as reference).

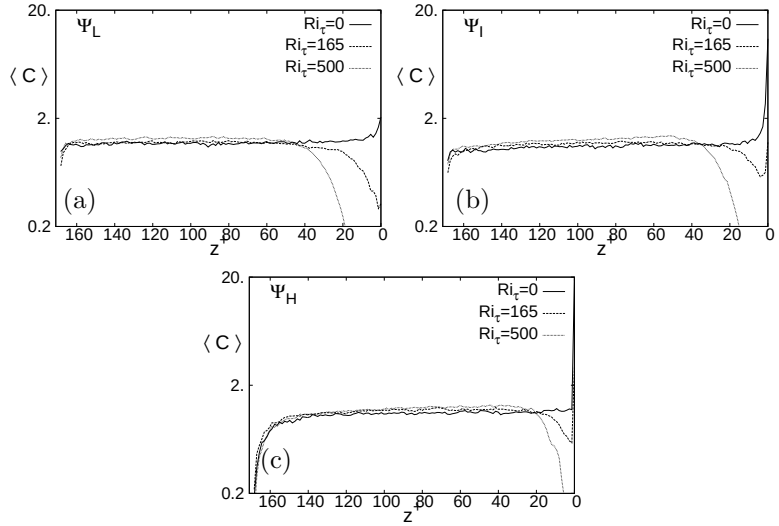

FIGURE 5.7 – Concentration in log-linear scale for Ψ_L (a),Ψ_I (b),Ψ_H (c) in the wall normal direction. $Ri_\tau = 0$ is shown in solid curve, $Ri_\tau = 165$ is shown in dashed lines, and $Ri_\tau = 500$ in dots

The trend is similar for the three values of Ψ: as we increase stratification, the regions closed to the surface are depleted. Particles will be driven away from vertical upward and this will be more evident at lower values of Ψ. In fact the width of the "depletion layer" increases as we decrease the value of Ψ since the mean strain rate induced by the presence of stratification will have more influence. In particular for Ψ_H the value at which the concentration drops to zero is nearly equal to $z^+ \approx 20$ which corresponds to the maximum value of strain rate.

To investigate what happen in the thermocline layer, in figure 5.8 the

profile of probability density function of the orientations at different Richardson number for the reference case of Ψ_I are shown for particles in a layer of $20 < z^+ < 40$.

It can be noted that the dashed curves which represent the pdf of spanwise orientations are unaffected by stratification since they show a symmetric profile with a peak around zero: No preferential orientations in spanwise direction. The story is different for the solid curves which represent the pdf of the streamwise orientations: in this case the curve shift toward right as we increase the stratification. The stratification induce an increase of preferential orientation of particles along the streamwise direction. The dotted curves represent the pdf of vertical orientations: the value of the peak decrease as the Richardson increase: the stratification makes the vertical migration more unstable.

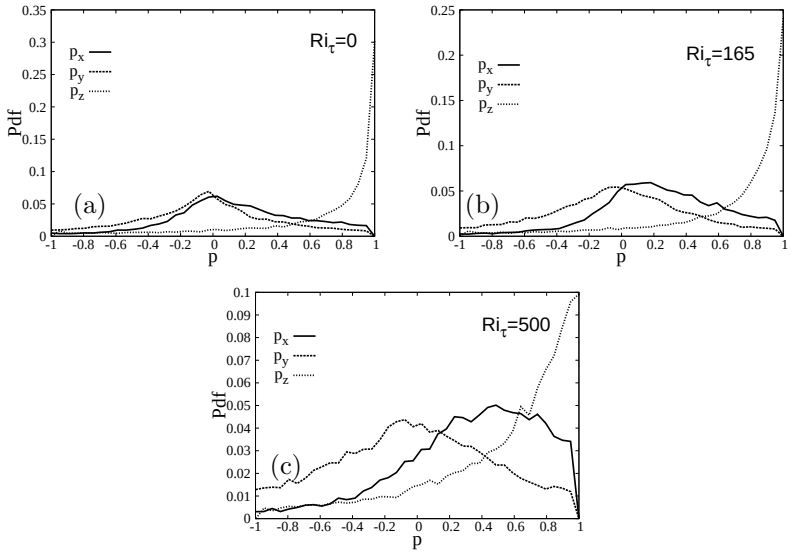

FIGURE 5.8 – Pdf of orientations for Ψ_I at different Richardson number. Particles inside the thermocline ($20 < z^+ < 40$) are considered.

To make these analysis more quantitative, in figure 5.9 the trends of $< p_z >$ and $< p_x >$ for the three Ψ considered and for the different values of shear Richardson number are shown. While for Ψ_H the trend of p_z seems to reach the vertical direction, in the case of Ψ_L and Ψ_I there is a significant

difference with respect to the neutrally buoyant case. In fact for Ψ_L and $Ri_\tau = 500$ swimmers were blocked just under the maximum value of strain rate. Interestingly, for Ψ_L and $Ri_\tau = 165$, the trend of $< p_z >$ reaches the asymptotic value under the maximum strain rate while the small amount of particles which are able to overpass this maximum value, tend to orient with the vertical direction. The same considerations could be done for Ψ_I. As discussed before, the reduction in the mean vertical direction corresponds to an increase of the mean streamwise direction. No preferential orientation in the spanwise direction (not shown) is observed.

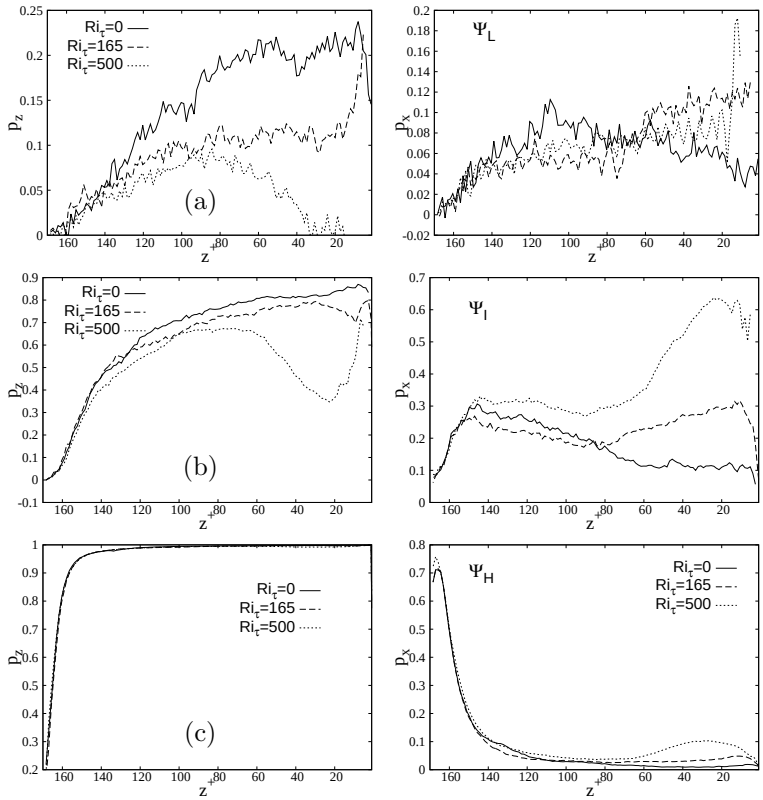

FIGURE 5.9 – Mean vertical and streamwise orientations for Ψ_L (a), Ψ_I (b), Ψ_H (c) in the wall normal direction. $Ri_\tau = 0$ is shown in solid curve, $Ri_\tau = 165$ is shown in dashed lines, and $Ri_\tau = 500$ in dots

Conclusions and future developments

Direct Numerical Simulation of free surface open channel flow is used to analyse the behaviour of the energy flux and of the local flow compressibility at the free surface and the effect on the dynamics of passive and active floaters. For sufficiently high Reynolds numbers ($Re_\tau = 509$ in the present study), an inverse energy cascade at the free surface, characterised by a transfer of energy from smaller to larger flow scales is observed. This inverse energy cascade can coexists with the classical direct energy cascade, with energy flowing from larger to smaller flow scales. It is found that direct/inverse energy cascades correlate with the behaviour of the two-dimensional surface divergence ∇_{2D}: Direct energy cascade is linked to regions of local flow expansion ($\nabla_{2D} > 0$), while inverse energy cascade is linked to regions of local flow compression ($\nabla_{2D} < 0$). It has been also proposed a phenomenological explanation of these results based on the dynamics of upwellings impinging on the free surface. Yet, the magnitude of the inverse energy cascade increases for increasing Re_τ. Despite its two-dimensional geometry, free surface turbulence has specific features which cannot be observed in two dimensional computations. The compressibility factor has been computed and it is showed that regions of local flow compression/expansion are seen at the free surface of a three dimensional domain. These findings are particularly important because they open new intriguing perspectives to model/parametrize the dynamics of chemical species and floaters dispersed at the free surface. It is remarked that present results can be important also for Large Eddy Simulation (LES). In LES, the most common subgrid-scale stress models are absolutely dissipative, i.e they can only account for the direct energy cascade. Based on current results, it is suggested that an inverse energy flux (inverse energy cascade) must be taken into account to ensure accurate predictions using LES [57, 58].

For what concerns passive dynamics, this study highlights the intermittent character of particle spatial distribution in free-surface turbulence

[19, 38]. Intermittency is due to buoyancy-driven clustering effects connected to the formation of sources and sinks of fluid velocity generated by sub-surface upwelling and downwelling motions. At small time scales, cluster formation is driven by the divergence of the flow field at the surface: clusters evolve in time producing fractal-like patterns that can be characterized by their correlation dimension. Results indicate that these patterns slowly relax towards a long-term distribution with exponential decay rate, requiring several Lagrangian integral fluid timescales. According to [33, 32], the surface-renewal timescale, which is usually employed to quantify interface scalar fluxes, is much smaller than the Lagrangian timescale and is thus inappropriate to quantify floater distribution dynamics.

Surface compressibility plays an important role in determining the motion of passive tracers like pollutants and nutrients but also the spreading rate of active ocean surfactants, such as phytoplankton [13, 39]. These findings provide useful indications to parametrize the relevant timescales characterizing dispersion of such species and therefore, can assist in developing models to predict cluster formation and evolution over several surface renewal cycles [68]. Future developments could incorporate strict physical connection between simulated cluster dynamics and real systems at much longer times. In particular, effects due to particle finite size (non overlapping) and surface tension (that attracts particles at the surface) [65] should be considered.

In case of stable stratification, simulation were run at Prandtl number $Pr = 5$, shear Richardson number $Ri_\tau = 0,\ 165$ and 500 considering floaters with specific density ratio $S = 0.5,\ 0.7,\ 0.8$ and 0.9. Flow statistics reveal that stable stratification suppresses the vertical transport of momentum and heat compared to the unstratified case, where temperature is a passive scalar. Using flow field visualization it is found that internal gravity waves may be generated (for sufficiently high Ri_τ) near the free surface, whereas active turbulent bursting phenomena still occur near the bottom wall. Flow field modifications induced by thermal stratification influence both surfacing and clustering of floaters at the surface. In particular, regardless of S, stratification focuses the range of values that can be attained by the rise velocity of floaters. This indicates that the vertical spread of the floater swarms induced by turbulence is decreased. Once at the surface, stratification prevents the formation of filamentary structures (observed in unstratified turbulence) and produces a nearly (two-dimensional)

homogeneous distribution. This behavior is associated to a weakening of upwelling/downwelling events produced by near-wall bursting phenomena. Future developments of this work will be the analysis of floater dynamics in stratified turbulence at higher Reynolds and Richardson numbers to reproduce physical situations occurring in deeper channels and for larger stratification. The effect of stratification on the compressibility and the energy flux will be also included.

The dynamic of self-propelled particles in turbulent open channel flow was introduced. Preliminary results linked to the dynamics of active particles and their interaction with the stratification demonstrated that the presence of stratification is able to forbid and block, the surfacing of phytoplankton. Further analysis will be done to understand deeply the formation of gyrotactic trapping in correspondence of thermal stratification.

Finally, it could be very interesting to study how surface waves (which effect in this study was neglected) could modify the distribution of active gyrotactic and passive particles. Recent experimental and numerical works [59, 24] have shown that non trivial behaviour arises when small sphere are floating on a water-air interface in which stationary waves are present. Collective dynamics could induce clustering in the node (point that undergo no vertical displacements) or in the antinode (points in which fluid purely moves in vertical direction) of the waves.

Acknowledgments

I would like to thank Prof. Alfredo Soldati who provided me the opportunity for this thesis. My thanks go also to Cristian Marchioli and Francesco Zonta with which I had the pleasure to work.
I wish to thank Prof. Eric Climent who allowed me to stay in Toulouse and to study the behaviour of gyrotactic particles within his group at IMFT.
Thanks also to the other guys of the lab for the discussions and advices: Mattia, Marco, Luca and Federico.

Bibliography

[1] Rutherford Aris. *Vectors, tensors and the basic equations of fluid mechanics*. Courier Dover Publications, 1990. 1.1.2

[2] V Artale, A Vulpiani, G Boffetta, M Cencini, and A Celani. Dispersion of passive tracers in closed basins. Technical report, 1997. 1.1

[3] E Aurell, G Boffetta, A Crisanti, G Paladin, and A Vulpiani. Predictability in the large: an extension of the concept of lyapunov exponent. *Journal of Physics A: Mathematical and General*, 30(1):1, 1997. 1.1

[4] George K Batchelor. Computation of the energy spectrum in homogeneous two-dimensional turbulence. *Physics of Fluids*, 12(12):II–233, 1969. 3.2.2

[5] Jeremie Bec. Fractal clustering of inertial particles in random flows. *Physics of Fluids*, 15(11):L81–L84, 2003. 1.1.2

[6] R. Benzi, S. Ciliberto, R. Tripiccione, C. Baudet, F. Massaioli, and S. Succi. *Phys. Rev. E*, 48:R29–R32, Jul 1993. 3.2.4

[7] Luca Biferale, Stefano Musacchio, and Federico Toschi. Inverse energy cascade in three-dimensional isotropic turbulence. *Physical review letters*, 108(16):164501, 2012. 1.1.1, 3.2.4

[8] Guido Boffetta, Jahanshah Davoudi, Bruno Eckhardt, and Jörg Schumacher. Lagrangian tracers on a surface flow: the role of time correlations. *Physical review letters*, 93(13):134501, 2004. 1.1.2, 3.2.5, 3.2.5, 3.2.5, 3.13

[9] D Byrne, H Xia, and M Shats. Robust inverse energy cascade and turbulence structure in three-dimensional layers of fluid. *Physics of Fluids*, 23(9):095109, 2011. 1.1.1

[10] Antonio Celani, Stefano Musacchio, and Dario Vincenzi. Turbulence in more than two and less than three dimensions. *Physical review letters*, 104(18):184506, 2010. 1.1.1

[11] Massimo Cencini, Fabio Cecconi, and Angelo Vulpiani. *Chaos*. World Scientific, 2009. 1.1.2

[12] M Chertkov, I Kolokolov, and M Vergassola. Inverse versus direct cascades in turbulent advection. *Physical review letters*, 80(3):512, 1998. 3.2.5

[13] John R Cressman, Jahanshah Davoudi, Walter I Goldburg, and Jörg Schumacher. Eulerian and lagrangian studies in surface flow turbulence. *New Journal of Physics*, 6(1):53, 2004. 4.1, 4.2.2, 4.3.3, 5.3

[14] Ottavio A Croze, Gaetano Sardina, Mansoor Ahmed, Martin A Bees, and Luca Brandt. Dispersion of swimming algae in laminar and turbulent channel flows: consequences for photobioreactors. *Journal of The Royal Society Interface*, 10(81):20121041, 2013. 5.1, 5.1.1

[15] F De Lillo, M Cencini, G Boffetta, and F Santamaria. Geotropic tracers in turbulent flows: a proxy for fluid acceleration. *Journal of Turbulence*, 14(7):24–33, 2013. 5.1

[16] Filippo De Lillo, Massimo Cencini, William M Durham, Michael Barry, Roman Stocker, Eric Climent, and Guido Boffetta. Turbulent fluid acceleration generates clusters of gyrotactic microorganisms. *Physical review letters*, 112(4):044502, 2014. 5.1

[17] Francesco d'Ovidio, Vicente Fernández, Emilio Hernández-García, and Cristóbal López. Mixing structures in the mediterranean sea from finite-size lyapunov exponents. *Geophysical Research Letters*, 31(17), 2004. 1.1

[18] Francesco d'Ovidio, Jordi Isern-Fontanet, Cristóbal López, Emilio Hernández-García, and Emilio García-Ladona. Comparison between eulerian diagnostics and finite-size lyapunov exponents computed from altimetry in the algerian basin. *Deep Sea Research Part I: Oceanographic Research Papers*, 56(1):15–31, 2009. 1

[19] Lauris Ducasse and Alain Pumir. Intermittent particle distribution in synthetic free-surface turbulent flows. *Physical Review E*, 77(6):066304, 2008. 5.3

[20] William M Durham, Eric Climent, Michael Barry, Filippo De Lillo, Guido Boffetta, Massimo Cencini, and Roman Stocker. Turbulence

drives microscale patches of motile phytoplankton. *Nature communications*, 4, 2013. 5.1, 5.1.1, 5.2

[21] William M Durham, John O Kessler, and Roman Stocker. Disruption of vertical motility by shear triggers formation of thin phytoplankton layers. *Science*, 323(5917):1067–1070, 2009. 5.1, 5.2

[22] William M Durham and Roman Stocker. Thin phytoplankton layers: characteristics, mechanisms, and consequences. *Annual review of marine science*, 4:177–207, 2012. 5.1

[23] Bruno Eckhardt and Jörg Schumacher. Turbulence and passive scalar transport in a free-slip surface. *Phys. Rev. E*, 64:016314, Jun 2001. 3.2.2, 3.2.5, 4.1, 4.2.2, 4.2.3, 4.3.3

[24] G Falkovich, A Weinberg, P Denissenko, and S Lukaschuk. Surface tension: floater clustering in a standing wave. *Nature*, 435(7045):1045–1046, 2005. 5.3

[25] Joel H Ferziger, Jeffrey R Koseff, and Stephen G Monismith. Numerical simulation of geophysical turbulence. *Computers & fluids*, 31(4):557–568, 2002. 3.3.1

[26] Leslie Fox and Ian Bax Parker. Chebyshev polynomials in numerical analysis. 1968. 2.4

[27] Uriel Frisch. *Turbulence: the legacy of AN Kolmogorov*. Cambridge university press, 1995. 1.1.1

[28] Krzysztof Gawedzki and Massimo Vergassola. Phase transition in the passive scalar advection. *Physica D: Nonlinear Phenomena*, 138(1):63–90, 2000. 3.2.5

[29] W. I. Goldburg, J. R. Cressman, Z. Vörös, B. Eckhardt, and J. Schumacher. *Phys. Rev. E*, 63:065303, May 2001. 3.2.4

[30] Ismael Hernández-Carrasco, Cristóbal López, Emilio Hernández-García, and Antonio Turiel. How reliable are finite-size lyapunov exponents for the assessment of ocean dynamics? *Ocean Modelling*, 36(3):208–218, 2011. 1.1

[31] RHA IJzermans, MW Reeks, E Meneguz, M Picciotto, and A Soldati. Measuring segregation of inertial particles in turbulence by a full lagrangian approach. *Physical Review E*, 80(1):015302, 2009. 1.1.2

[32] Alireza Kermani, Hamid R Khakpour, Lian Shen, and Takeru Igusa. Statistics of surface renewal of passive scalars in free-surface turbulence. *Journal of Fluid Mechanics*, 678:379–416, 2011. 3.2.2, 5.3

[33] Satoru Komori, Yasuhiro Murakami, and Hiromasa Ueda. The relationship between surface-renewal and bursting motions in an open-channel flow. *Journal of Fluid Mechanics*, 203:103–123, 6 1989. 3.2.2, 5.3

[34] Robert H Kraichnan. Inertial ranges in two-dimensional turbulence. Technical report, DTIC Document, 1967. 1.1.1, 3.2.2, 3.2.5

[35] S Kumar, R Gupta, and S Banerjee. An experimental investigation of the characteristics of free-surface turbulence in channel flow. *Physics of Fluids*, 10(2):437–456, 1998. 3.2.2

[36] Guglielmo Lacorata, Erik Aurell, and Angelo Vulpiani. Drifter dispersion in the adriatic sea: Lagrangian data and chaotic model. In *Annales Geophysicae*, volume 19, pages 121–129. Copernicus GmbH, 1999. 1, 1.1

[37] K Lam and S Banerjee. On the condition of streak formation in a bounded turbulent flow. *Physics of Fluids*, 4(2):306–320, 1992. 3.3.1

[38] Jason Larkin, M. M. Bandi, Alain Pumir, and Walter I. Goldburg. Power-law distributions of particle concentration in free-surface flows. *Phys. Rev. E*, 80:066301, Dec 2009. 4.1, 4.2.2, 4.2.3, 4.2.3, 5.3

[39] Jason Larkin, Walter Goldburg, and M.M. Bandi. Time evolution of a fractal distribution: Particle concentrations in free-surface turbulence. *Physica D: Nonlinear Phenomena*, 239(14):1264 – 1268, 2010. 4.1, 4.2.3, 4.2.3, 5.3

[40] Jacques Magnaudet. High-reynolds-number turbulence in a shear-free boundary layer: revisiting the hunt–graham theory. *Journal of Fluid Mechanics*, 484:167–196, 2003. 1.1.1

[41] Cristian Marchioli, Marco Fantoni, and Alfredo Soldati. Influence of added mass on anomalous high rise velocity of light particles in cellular flow field: A note on the paper by maxey (1987). *Physics of Fluids*, 19(9):098101, 2007. 4.3.2

[42] MR Maxey. The gravitational settling of aerosol particles in homogeneous turbulence and random flow fields. *Journal of Fluid Mechanics*, 174:441–465, 1987. 4.3.2

[43] Pablo D Mininni, Alexandros Alexakis, and Annick Pouquet. Scale interactions and scaling laws in rotating flows at moderate rossby numbers and large reynolds numbers. *Physics of Fluids*, 21(1):015108, 2009. 1.1.1

[44] Romain Monchaux, Mickaël Bourgoin, and Alain Cartellier. Preferential concentration of heavy particles: a voronoï analysis. *Physics of Fluids*, 22(10):103304, 2010. 4.3.3

[45] Ryuichi Nagaosa. Direct numerical simulation of vortex structures and turbulent scalar transfer across a free surface in a fully developed turbulence. *Physics of Fluids*, 11(6):1581–1595, 1999. 1.1.1

[46] Ryuichi Nagaosa and Robert A. Handler. Statistical analysis of coherent vortices near a free surface in a fully developed turbulence. *Physics of Fluids*, 15(2), 2003. 3.2.1, 3.2.2

[47] Ryuichi Nagaosa and Robert A. Handler. Characteristic time scales for predicting the scalar flux at a free surface in turbulent open-channel flows. *AIChE Journal*, 58(12):3867–3877, 2012. 3.2.2

[48] Y. Pan and S. Banerjee. A numerical study of free surface turbulence in channel flow. *Physics of Fluids*, 7(7), 1995. 1.1.1, 1.1.1, 3.2.2, 3.2.3, 3.2.3, 3.2.4

[49] TJ Pedley and JO Kessler. A new continuum model for suspensions of gyrotactic micro-organisms. *Journal of Fluid Mechanics*, 212:155–182, 1990. 5.1

[50] TJ Pedley and JO Kessler. Hydrodynamic phenomena in suspensions of swimming microorganisms. *Annual Review of Fluid Mechanics*, 24(1):313–358, 1992. 5.1, 5.2

[51] Blair Perot and Parviz Moin. Shear-free turbulent boundary layers. part 1. physical insights into near-wall turbulence. *Journal of Fluid Mechanics*, 295:199–227, 1995. 1.1.1

[52] Blair Perot and Parviz Moin. Shear-free turbulent boundary layers. part 2. new concepts for reynolds stress transport equation modelling of inhomogeneous flows. *Journal of Fluid Mechanics*, 295:229–245, 1995. 1.1.1

[53] Maurizio Picciotto, Cristian Marchioli, Michael W Reeks, and Alfredo Soldati. Statistics of velocity and preferential accumulation of microparticles in boundary layer turbulence. *Nuclear engineering and design*, 235(10):1239–1249, 2005. 1.1.2

[54] M. Rashidi and S. Banerjee. Turbulence structure in free surface channel flows. *Physics of Fluids*, 31(9), 1988. 1.1.1, 3.2.2

[55] Javier Ruiz, Diego MacÃas, and Francesc Peters. Turbulence increases the average settling velocity of phytoplankton cells. *Proceedings of the National Academy of Sciences of the United States of America*, 101(51):17720–17724, 2004. 4.2.1, 4.3.2

[56] David Saintillan and Michael J Shelley. Instabilities, pattern formation, and mixing in active suspensions. *Physics of Fluids*, 20(12):123304, 2008. 5.1

[57] MV Salvetti and S Banerjee. Apriori tests of a new dynamic subgrid-scale model for finite-difference large-eddy simulations. *Physics of Fluids*, 7(11):2831–2847, 1995. 5.3

[58] MV Salvetti, Y Zang, RL Street, and S Banerjee. Large-eddy simulation of free-surface decaying turbulence with dynamic subgrid-scale models. *Physics of Fluids*, 9(8):2405–2419, 1997. 5.3

[59] Ceyda Sanlı, Detlef Lohse, and Devaraj van der Meer. From antinode clusters to node clusters: The concentration-dependent transition of floaters on a standing faraday wave. *Physical Review E*, 89(5):053011, 2014. 5.3

[60] Francesco Santamaria, Filippo De Lillo, Massimo Cencini, and Guido Boffetta. Gyrotactic trapping in laminar and turbulent kolmogorov flow. *Physics of Fluids*, 26(11):111901, 2014. 5.1

[61] Turgut Sarpkaya. Vorticity, free surface, and surfactants. *Annual Review of Fluid Mechanics*, 28(1):83–128, 1996. 1.1.1, 3.2.2, 3.2.3, 3.2.4, 3.2.4

[62] Komori Satoru, Ueda Hiromasa, Ogino Fumimaru, and Mizushina Tokuro. Turbulence structure and transport mechanism at the free surface in an open channel flow. *International Journal of Heat and Mass Transfer*, 25(4):513 – 521, 1982. 3.2.2

[63] Jörg Schumacher. Probing surface flows with lagrangian tracers. *Progress of Theoretical Physics Supplement*, 150:255–266, 2003. 3.2.5, 3.2.5, 4.3.3

[64] Enrico Ser-Giacomi, Vincent Rossi, Cristobal Lopez, and Emilio Hernandez-Garcia. Flow networks: A characterization of geophysical fluid transport. *preprint arXiv:1409.4171*, 2014. 1.1

[65] Pushpendra Singh, Daniel D Joseph, and Nadine Aubry. Dispersion and attraction of particles floating on fluid–liquid surfaces. *Soft Matter*, 6(18):4310–4325, 2010. 5.3

[66] Leslie M Smith, Jeffrey R Chasnov, and Fabian Waleffe. Crossover from two-to three-dimensional turbulence. *Physical review letters*, 77(12):2467, 1996. 1.1.1

[67] Andrey Sokolov, Raymond E Goldstein, Felix I Feldchtein, and Igor S Aranson. Enhanced mixing and spatial instability in concentrated bacterial suspensions. *Physical Review E*, 80(3):031903, 2009. 5.1

[68] Matthew S Spydell and Falk Feddersen. The effect of a non-zero lagrangian time scale on bounded shear dispersion. *Journal of Fluid Mechanics*, 691:69–94, 2012. 4.2.3, 5.3

[69] Patrick Tabeling. Two-dimensional turbulence: a physicist approach. *Physics Reports*, 362(1):1–62, 2002. 4.2.2

[70] Iztok Tiselj, Robert Bergant, Borut Mavko, Ivan BajsicÌ, and Gad Hetsroni. Dns of turbulent heat transfer in channel flow with heat conduction in the solid wall. *Journal of heat transfer*, 123(5):849–857, 2001. 3.3

[71] DT Walker, RI Leighton, and Luis O Garza-Rios. Shear-free turbulence near a flat free surface. *Journal of fluid Mechanics*, 320:19–51, 1996. 1.1.1

[72] H Xia, D Byrne, G Falkovich, and M Shats. Upscale energy transfer in thick turbulent fluid layers. *Nature Physics*, 7(4):321–324, 2011. 1.1.1

[73] Z Xiao, M Wan, S Chen, and GL Eyink. Physical mechanism of the inverse energy cascade of two-dimensional turbulence: a numerical investigation. *Journal of Fluid Mechanics*, 619:1–44, 2009. 3.2.3, 3.2.4

[74] Caijuan Zhan, Gaetano Sardina, Enkeleida Lushi, and Luca Brandt. Accumulation of motile elongated micro-organisms in turbulence. *Journal of Fluid Mechanics*, 739:22–36, 2014. 5.1

[75] Francesco Zonta, Miguel Onorato, and Alfredo Soldati. Turbulence and internal waves in stably-stratified channel flow with temperature-dependent fluid properties. *Journal of Fluid Mechanics*, 697:175–203, 2012. 3.3.1